James Eric (Orcid ID: 0000-0002-6507-4997)

Offshore Wind Speed Estimates from a High-Resolution Rapidly-Updating Numerical Weather Prediction Model Forecast Dataset

(manuscript for submission to *Wind Energy*)

Eric P. James[1] (corresponding author; eric.james@noaa.gov), Stanley G. Benjamin[2] (stan.benjamin@noaa.gov), and Melinda Marquis[2] (melinda.marquis@noaa.gov)

[1]*University of Colorado, Cooperative Institute for Research in Environmental Sciences at the NOAA Earth System Research Laboratory / Global Systems Division*

325 Broadway, Boulder, Colorado 80305-3337,

United States of America

[2]*NOAA Earth System Research Laboratory / Global Systems Division*

325 Broadway, Boulder, Colorado 80305-3337,

United States of America

Manuscript submitted 13 Feb 2017

Revisions submitted 2 Aug 2017

Abstract

In association with the Department of Energy-funded *Position of Offshore Wind Energy Resources* (POWER) project, we present results from compositing a three-year dataset of 80-m (above ground level) wind forecasts from the 3-km High-Resolution Rapid Refresh (HRRR) model over offshore regions for the contiguous United States (US). The HRRR numerical weather prediction system runs once an hour and features hourly data assimilation, providing a key advantage over previous model-based offshore wind datasets. Based on one-hour forecasts from the HRRR model, we highlight the different climatological regimes of the near-shore environment, characterizing the mean 80-m wind speed as well as the frequency of exceeding 4, 12, and 25 m s^{-1} for east and west coast, Gulf of Mexico, and Great Lake locations. Preliminary verification against buoy measurements demonstrates good agreement with observations. This dataset can inform the placement of targeted measurement systems in support of improving resource assessments and wind forecasts to advance offshore wind energy goals both in New England and other coastal regions of the US.

Keywords

Wind forecasting, offshore wind, resource assessment, weather prediction model

1. Introduction

Offshore wind energy currently provides approximately 10 GW of electricity in Europe, constituting a 29% increase in a six-month period [1]. In contrast, within the United States (US), only a single 30 MW wind farm (near Block Island, RI) has started operating as of the end of 2016. The United States (US) Department of Energy (DOE) has investigated the nature of the offshore wind energy resource along the US coastline [2, 3, 4]. In order to accelerate the development of technologies used for offshore wind, the DOE has developed a strategy for offshore wind development in the US [5]. This strategy fits within the ambitious "Wind Vision" report published in March 2015 [6]. Moving towards these offshore wind energy goals will necessitate identifying regions of large resource, and this prospecting process requires the deployment of high-quality measurement instrumentation within the turbine rotor layer [7]. These measurements must serve

the dual purpose of directly estimating the resource and understanding the flows contributing to this resource, as well as evaluating the abilities of current numerical weather prediction (NWP) models to simulate such flows. If models could be shown to produce accurate four-dimensional wind fields, the need to deploy costly instrumentation would be reduced.

Aiming to address these goals, an extensive measurement and modeling campaign, referred to as *Improving the Mapping and Prediction of Offshore Wind Resources* (IMPOWR), was conducted offshore of southern New England during 2013-14 [8]. Tower measurements were taken at the Cape Wind tower (located in Nantucket Sound, south of Hyannis Port, MA), building on an observational record during 2003-11. In addition, two land-based lidars provided coastal wind measurements up to 150 m above ground level (AGL), and aircraft research flights were conducted to sample a variety of coastal flow regimes. Ongoing research using the IMPOWR dataset seeks to determine whether the Weather Research and Forecasting – Advanced Research WRF (WRF-ARW) model is capable of representing the behavior of the marine boundary layer, and elucidate the causes of model errors.

Identifying regions of large offshore wind energy potential was one of the main goals of the complementary *Position of Offshore Wind Energy Resources* (POWER)

project, which also took place in 2013-14 [9]. Shipborne National Oceanic and Atmospheric Administration (NOAA) High-Resolution Doppler Lidar (HRDL; [10, 11]) measurements were taken from the NOAA Research Vessel (R/V) *Ronald H. Brown* during 9 Jul – 12 Aug 2004; these observations were used during POWER to assess rotor-layer wind characteristics throughout the Gulf of Maine during this month-long period [12].

The focus of this study (one particular component of the multi-faceted POWER project) is on a multi-year archive of NWP forecasts from the NOAA High-Resolution Rapid Refresh (HRRR) model. Our goal is to describe the unique advantages of this offshore wind dataset in the context of previous studies, investigating spatial and temporal variability within the nearshore environment and undertaking some preliminary verification against wind measurements. If it can be established that the HRRR does reasonably well (i.e., with error statistics that are comparable or better than previous datasets) with forecasting offshore winds, this dataset, which continues to grow in length, could complement and even guide the deployment of additional high-quality measurement systems for the purpose of examining offshore wind resources and improving offshore wind forecasts within the US.

Several previous studies have attempted to create offshore wind datasets for use in the renewable energy community. Manwell et al. [13] describe existing wind observations offshore of New England, and apply the commonly-used "measure-correlate-predict" (MCP; [14]) method to correlate a brief period of elevated wind observations with longer-term measurements from a nearby site. The MCP method is useful for individual sites, but generalized resource maps require some way of capturing spatial variability in wind fields. Woods et al. [15] use a novel resampling technique to interpolate from a limited number of high-resolution WRF-ARW simulations initialized with North American Regional Reanalysis (NARR) data to a 30-year wind time series for a small region on the outer continental shelf south of New Jersey. Their model configuration differs significantly from that used in the HRRR model, particularly in the absence of any data assimilation.

Monaldo et al. [16] have proposed the development of an oceanic wind dataset based on a 10-year archive of spaceborne synthetic aperture radar imagery. While this remote sensing technology is increasing in maturity, it is not clear to what extent the results will be influenced by assumptions made in the retrieval technique. In the future, a well-calibrated remote sensing dataset such as this could play an important role in offshore wind dataset development.

The most extensive existing offshore wind resource assessment studies within the US have been undertaken by the National Renewable Energy Laboratory [2, 3, 4]. Earlier studies [2, 3] used a limited number of numerical model simulations initialized with reanalysis data; one year of simulation days was selected from a 15-year period through a stratified random sampling scheme wherein the year was picked at random but the day of the year was retained in order to represent the seasonal cycle. The simulations, using proprietary modeling software, were run in a nested configuration, down to 1 km resolution, with downscaling to 200 m resolution, to derive a wind dataset at 90 m AGL. A more recent effort [4] combined this dataset with the Wind Integration National Dataset (WIND) Toolkit [17] to derive a wind climatology at 100 m AGL out to 200 nautical miles offshore.

While using a similar approach to these previous studies (i.e., atmospheric modeling), the HRRR-based approach described in this study has several major advantages. First, the HRRR uses hourly data assimilation; particularly important are the assimilation of 15-minute radar reflectivity observations [18], and of high-frequency and high-coverage commercial aircraft observations [19]. Second, the physics parameterizations within the HRRR configuration of WRF-ARW are developed and evaluated with a specific goal of improving short lead time forecasts. In the following section, we describe in more detail the HRRR model and its

advanced data assimilation configuration designed to provide the best initial condition for forecasts of a wide variety of weather phenomena, followed by a summary of the development of the 2013-present HRRR archive, and some preliminary verification against offshore wind measurements. This section is followed by a presentation of results, beginning with East Coast composite offshore wind maps, followed by time series analysis of several different nearshore meteorological environments, and then a brief overview of the dataset for other potential offshore wind regions within the US. Finally, in the concluding section, some remarks are given regarding the use of the dataset and future expansion of this study.

2. Methods

In this section, we describe the HRRR NWP system and its real-time applications, followed by a description of our experimental design in constructing the compositing dataset.

a. High-Resolution Rapid Refresh System

The HRRR model [18] was developed at the NOAA Earth System Research Laboratory (ESRL) / Global Systems Division (GSD) in 2008 as a real-time convection-allowing (i.e., resolving some internal structure for large individual

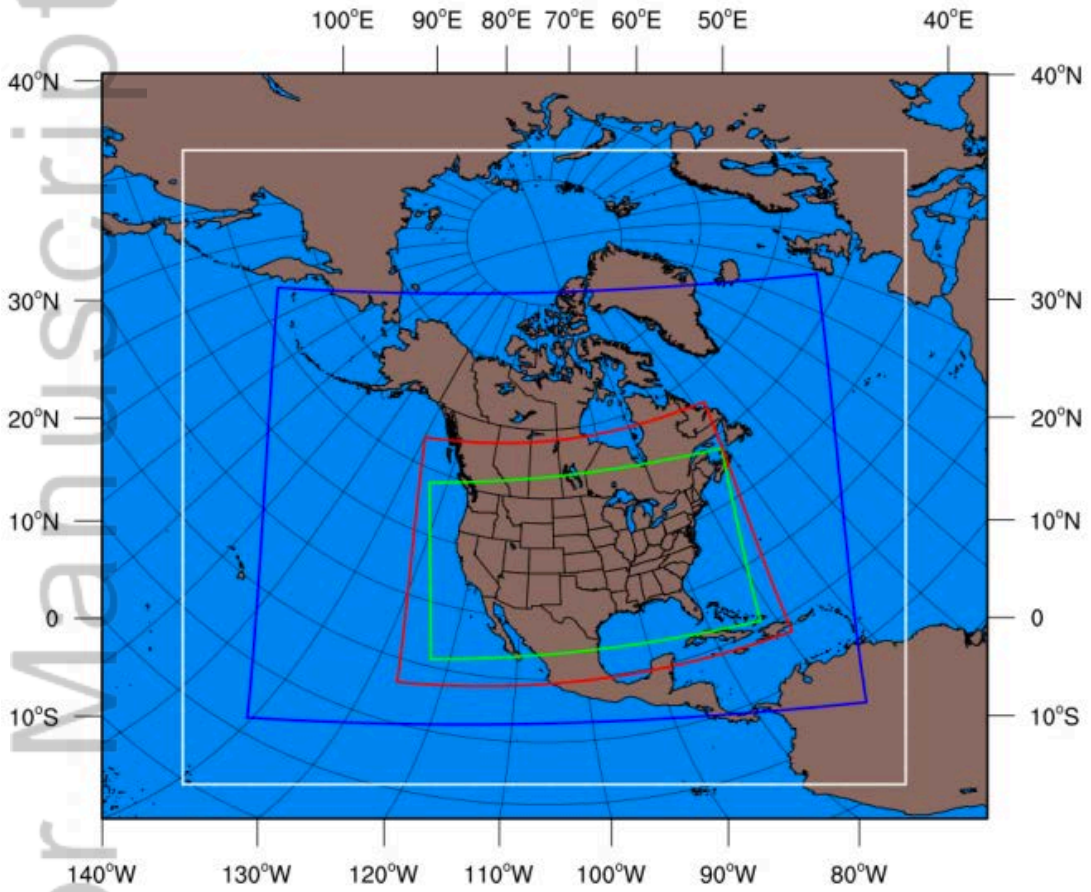

Fig. 1. Map of North America showing the computational domains of the earlier RUC (red), an earlier version of the RAP (blue), the current (2017) version of the RAP (white) and the HRRR (green) models. See [20] for more details.

thunderstorms) forecast system, initially for the northeastern US. In 2010 the domain was extended to cover the contiguous US (CONUS). The HRRR uses initial and lateral boundary conditions from the 13-km Rapid Refresh (RAP) model [20], which is itself the replacement for the Rapid Update Cycle (RUC; the original rapidly-updated NWP system [21]). The RAP and HRRR domains are shown in Fig. 1. Note that, although the eastern boundary of the HRRR domain is relatively close to the far eastern coast of Maine, it is not anticipated that errors from the lateral boundaries are significant enough to affect the results due to the relatively smooth lateral boundary conditions provided by the RAP.

The RAP and the HRRR use the community-supported WRF-ARW model [22], as well as the Gridpoint Statistical Interpolation (GSI [20,23,24]) for data assimilation to initialize the forecast model. The HRRR has 3-km horizontal grid spacing, which provides several significant advantages over the coarser resolution RAP. First, deep moist convection can be represented on the model grid without being parameterized. Alexander et al. [18] have shown that the HRRR is capable of representing many different modes of convective storm (largely, thunderstorm) evolution. A second advantage, particularly for the complex coastline of the northeastern US and other coastal US areas, is the improved representation of the land-water interface; this could be an especially important factor for representing

the low-level wind field in the nearshore environment. The RAP and HRRR both use a sigma vertical coordinate, with 50 model levels; the first three model levels are near 8 m, 38 m, and 90 m AGL at sea level.

Since the RAP and the HRRR are updated every hour, improved initial conditions can be obtained from the latest observations through hourly data assimilation. The ability of these models to assimilate recent observations is critical for their forecast skill, particularly because of the availability of frequent vertical profiles from commercial aircraft observations [20]; these aircraft observations have the strongest overall impact within the observation suite assimilated by the RAP [19]. Both models use the GSI system to carry out three-dimensional hybrid ensemble/variational data assimilation, combining latest observations with a high-resolution 1-h forecast to create an initial condition for the next model forecast. Ensemble forecasts from the Global Forecast System are used to calculate flow-dependent covariance fields, significantly improving forecasts over those achieved with a static three-dimensional variational analysis [25]. After the assimilation of recent observations, a cloud (or, more generally, hydrometeor) analysis [20] is carried out based primarily on satellite and surface-based ceilometer data.

Radar reflectivity observations in the RAP are assimilated through a diabatic digital filter initialization (DDFI) procedure [26]. The HRRR assimilates reflectivity observations in a more complex manner than the RAP; first a 1-hour "pre-forecast" WRF integration is carried out (starting from an initial condition downscaled from the RAP), with application of latent heating specified from radar reflectivity observations every 15 minutes. This "pre-forecast" integration results in a much more realistic hydrometeor structure within the HRRR at the start of the full forecast. After this 1-hour "pre-forecast", GSI brings in all current observations and carries out full hybrid ensemble-variational data assimilation before the WRF forecast is started. This initialization procedure for the HRRR, using the latest conventional and radar reflectivity observations, allows some adjustment of the downscaled RAP initial conditions to the 3-km topography and coastline configuration.

In this study, we consider 1-hour HRRR forecasts (from the full forecast, after the 1-h pre-forecast) as our best estimate of the state of the atmosphere. One-hour forecasts are considered to be close enough to the initial time (and the GSI data assimilation described above) that the model forecast error is still small and the forecast is still strongly constrained by recent observations. At the same time, 1-h forecasts are also far enough from the initial time that the model has had time to

spin up realistic 3-km structures in the atmosphere consistent with the atmospheric physical processes represented in the HRRR model that we wish to capture. Sufficient adjustment to attain physical consistency with the atmospheric relationships represented in the model, after the arrival of observations in the data assimilation procedure, requires this 1-h forecast duration. James et al. [27] present additional details and verification of HRRR 1-h forecasts applicable for potential wind and solar energy generation for the contiguous US.

A suite of physical parameterizations [20] is used in the RAP and HRRR models within the WRF framework; changes within the HRRR configuration during the 2013-15 period of record are outlined in Table 1, along with comparisons with the WRF configuration used by Draxl et al. [17] in generating the WIND Toolkit. Among the most important parameterizations for forecasting low-level winds is the planetary boundary layer (PBL) scheme, which is a modified version of the Mellor-Yamada-Nakanishi-Niino (MYNN) scheme (described by Nakanishi [28] and Nakanishi and Niino [29, 30]; see appendix B of Benjamin et al. [20]). The MYNN is a 1.5-order closure scheme. Mean turbulent quantities are related to vertical gradients in temperature, water vapor mixing ratio, and the horizontal wind components by coefficients that depend on the local turbulent kinetic energy (TKE), the mixing length, and the dimensionless stability functions. MYNN, in an

improvement over the earlier Mellor-Yamada-Janjic (MYJ [31]) scheme, includes the effects of buoyancy in the pressure covariance terms, and uses closure constants that are derived from large eddy simulation (LES) results rather than from observations. MYNN mixing length formulations are also more flexible across the stability spectrum than those of many of the other schemes [28]. The MYNN scheme has been shown to be nearly unbiased and to have small mean errors in its representation of PBL temperature and water vapor mixing ratio [32], and earlier versions of the scheme have been evaluated in the context of a number of other PBL scheme intercomparison studies [33, 34, 35]. For offshore winds, the influence of sea surface wave activity is handled by a wind speed dependent drag coefficient as described by [36].

The RAP and the HRRR use the RUC land surface model [37], which was developed over many years in association with improvements to the RUC and WRF models. Cloud microphysics are parameterized according to Thompson scheme [38, 39, 40] within WRF. The shortwave and longwave solar radiation components are currently parameterized using the Rapid Radiative Transfer Model – Global (RRTMG [41]). Earlier versions of the HRRR used the Dudhia shortwave scheme [42] and the Rapid Radiative Transfer Model (RRTM [43]) longwave scheme (prior to the end of

March 2013), and the Goddard [44] shortwave scheme in combination with RRTM longwave (prior to March 2014).

b. Hourly 80-m Wind Dataset

This study takes advantage of an approximately four-year archive of experimental HRRR (i.e., not the operational HRRR) forecasts. Archival of HRRR forecasts began in late January 2012; however, in order to include only full years in the dataset, we exclude 2012 from our results. Our archive currently contains a large variety of 2-dimensional fields, both kinematic and moisture-related. For this study, only results related to the 80-m (above ground level) wind field are presented. While it is likely that wind fields at levels other than 80 m are of interest to the renewable energy community, at this time the HRRR forecast archive contains only the wind field at 10- and 80-m heights. Other variables of potential interest, such as turbulent kinetic energy, have only recently begun to be output from the HRRR. Forecasts of 80-m winds only became available in RAP output beginning in 2016, so RAP forecasts are not included in our analysis. RAP performance for 10-m winds is presented by Benjamin et al. [20].

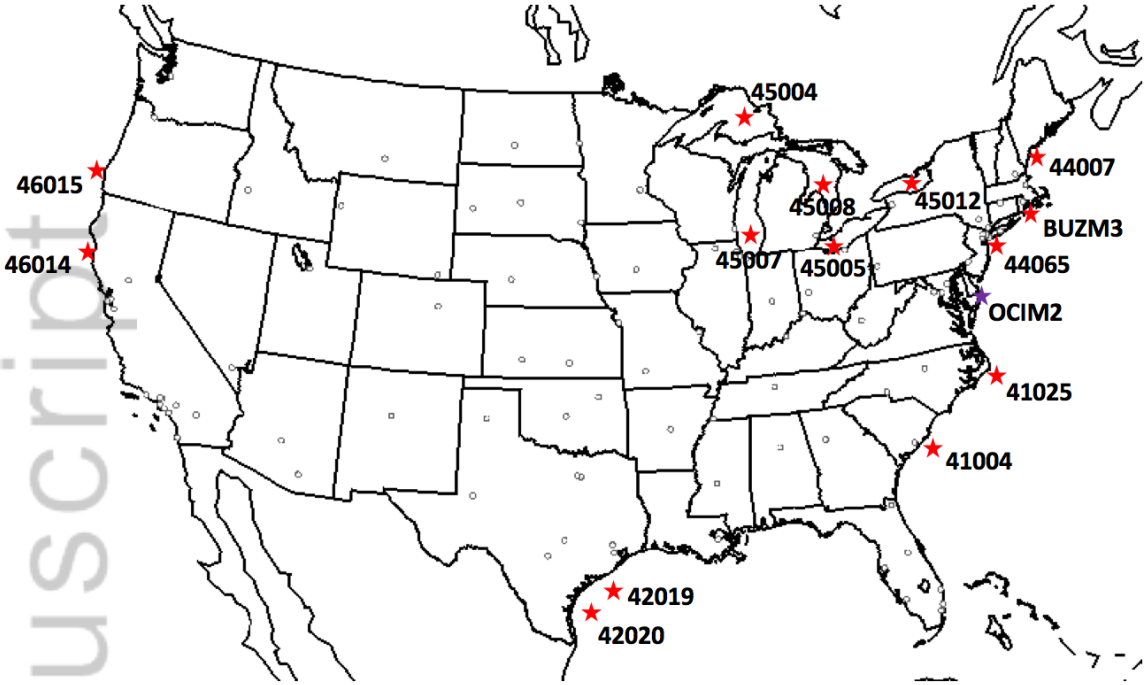

Fig. 2. Map of the contiguous United States with the locations of buoys used for verification in red stars. The purple star indicates coastal buoy OCIM2 (see text).

c. 10-m Wind Speed Verification against Offshore Buoy Measurements

Wind observations at heights that are comparable to modern wind turbines are extremely scarce in the offshore region, rendering any direct verification of HRRR 80-m winds in this region very challenging. Therefore, we undertake preliminary verification of HRRR 10-m winds against buoy-based anemometers around the coastal US. For the period of this study, 10-m wind forecasts from the HRRR are actually the wind at the lowest model level (which is near 8 m at sea level, and near

~7.8 m at the 100-200 m elevation of the upper Great Lakes). For this study, we have selected 14 buoys from the National Data Buoy Center (see Table 2), and we compare HRRR 1-h forecasts of wind speed at the closest model gridpoint to the observed wind speed. The buoys are located in a variety of offshore environments, with two near the west coast (Oregon, California), two off the coast of Texas, two off the Carolina coast, three near the northeastern seaboard, and five over the Great Lakes (one per lake; see Fig. 2).

For the purpose of verifying against observations at heights other than 8 m, we employ a simple log law [45] to interpolate HRRR lowest model level winds to the anemometer heights of the buoys:

$$v_z = v_{ref} \frac{\ln(z/z_0)}{\ln(z_{ref}/z_0)}$$

where v_z is the wind speed interpolated to anemometer height, v_{ref} is the wind speed at the lowest model level (8 m AGL at sea level, 7.8 m AGL for the Great Lakes), z is the anemometer height, z_{ref} is the lowest model level height AGL, and z_0 is the roughness length for open water (0.0002 according to [46]). While this interpolation is admittedly crude, it allows preliminary verification against non-standard buoy anemometer heights.

Table 2 presents verification results at all 14 buoys in terms of mean bias (forecast minus observation) and root mean squared error (RMSE). It is seen that, excluding the Great Lakes buoys, the HRRR winds are generally slightly too weak (after interpolating as described above), with RMSEs near 2.0 m s^{-1}. These RMSE values are lower than those found for METAR stations over the HRRR domain [27]. Performance is generally best for sites along the east coast and offshore of Texas.

Figure 3 shows time series of buoy observations (blue) compared against the interpolated HRRR 1-h forecasts (red), with a running monthly mean applied to the data, for four representative buoys. As is seen in Fig. 3a, biases at the Gulf of Mexico buoy 42020 are generally within 1 m s^{-1} of zero. Some regime dependence of the bias is evident in the time series, although seasonal signals are more difficult to discern; note that the time series cover a 2.5-year period in each case. A shift from a slight negative bias to a slight positive bias in April 2015 is more evident in the time series for buoys 44065 (New York Harbor entrance; Fig. 3b) and 46015 (offshore of Port Orford, Oregon; Fig. 3c); this shift corresponds to the implementation of the Coupled Atmosphere-Ocean Response Experiment (COARE) algorithm 3.0 [47] within the MYNN scheme for the parameterization of a wind-wave drag coefficient; prior to this change, the drag coefficient was constant with varying wind speeds.

Examining the diurnal cycle of bias and RMSE at each buoy, we find relatively minor changes in the character of the errors during a 24-h period. Figure 4 presents the bias and RMSE for Buoy 44065 (New York Harbor Entrance); it is seen that the bias over the three-year period reaches a minimum (negative bias) during the midday period (~18 UTC, which is 14 local time; Fig. 4a). RMSE varies relatively little during the day (Fig. 4b). Many of the other coastal buoys show similar diurnal cycles (not shown).

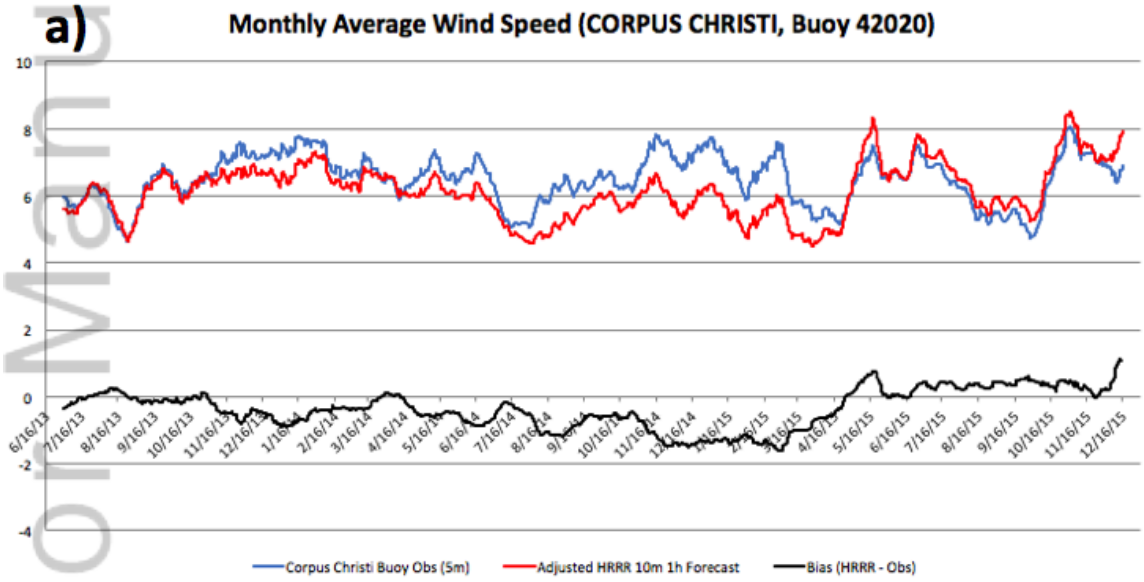

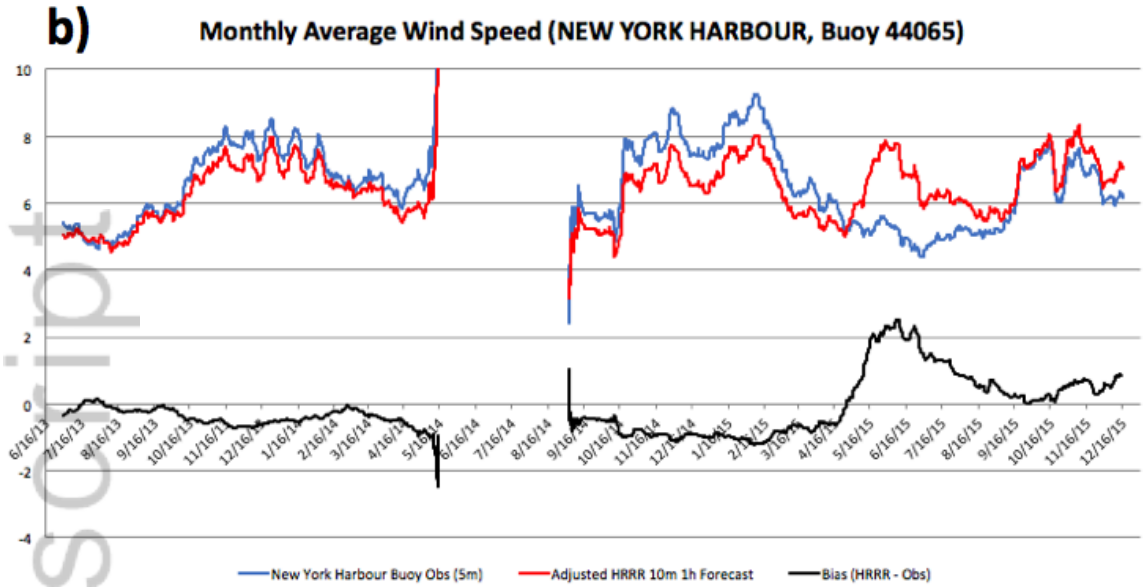

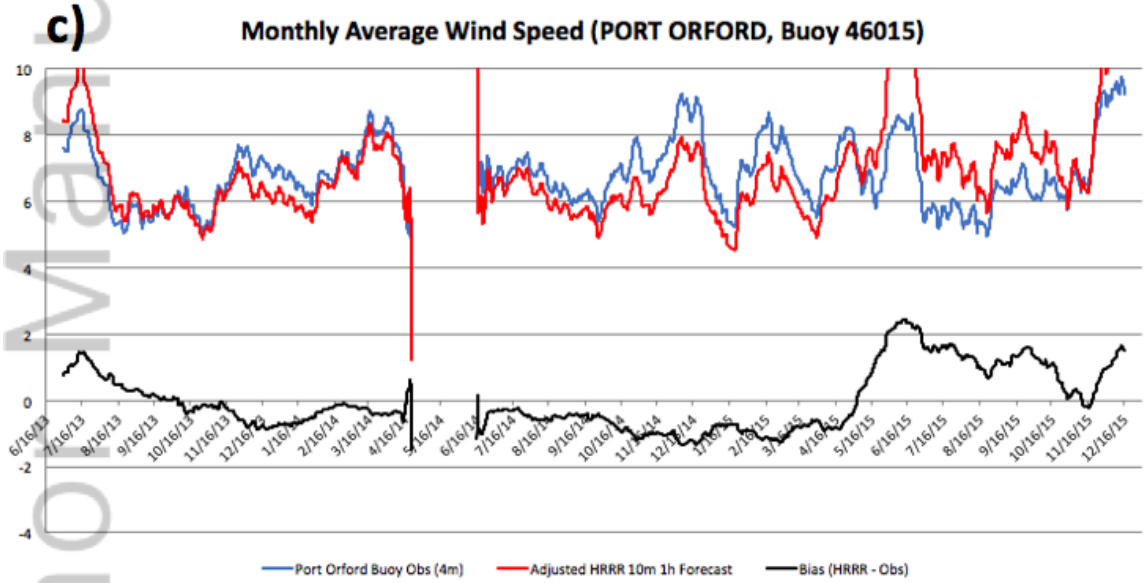

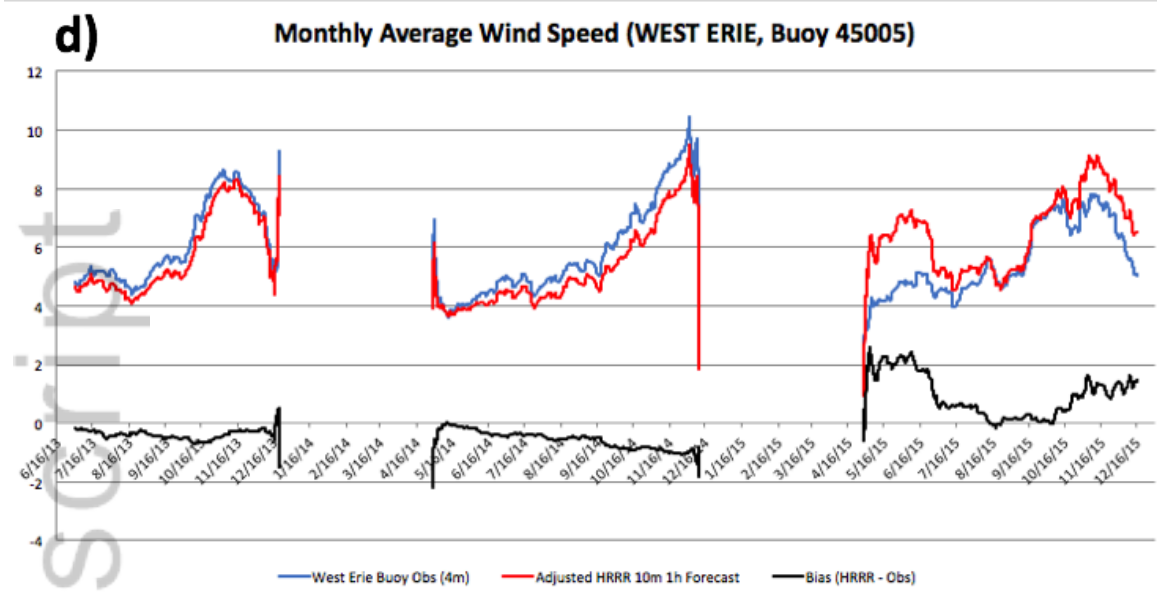

Fig. 3. Time series of HRRR 1-h forecasts of 10-m wind speed interpolated to buoy anemometer height using the log law (red curve; m s^{-1}), raw buoy wind speed observations (blue curve; m s^{-1}), and the bias (black curve; HRRR minus observations; m s^{-1}), for (a) Buoy 42020 (near Corpus Christi), (b) Buoy 44065 (New York Harbor Entrance), (c) Buoy 46015 (offshore of Port Orford, Oregon), and (d) Buoy 45005 (in western Lake Erie). A 30-day running mean is applied to reduce the amount of short time-scale noise.

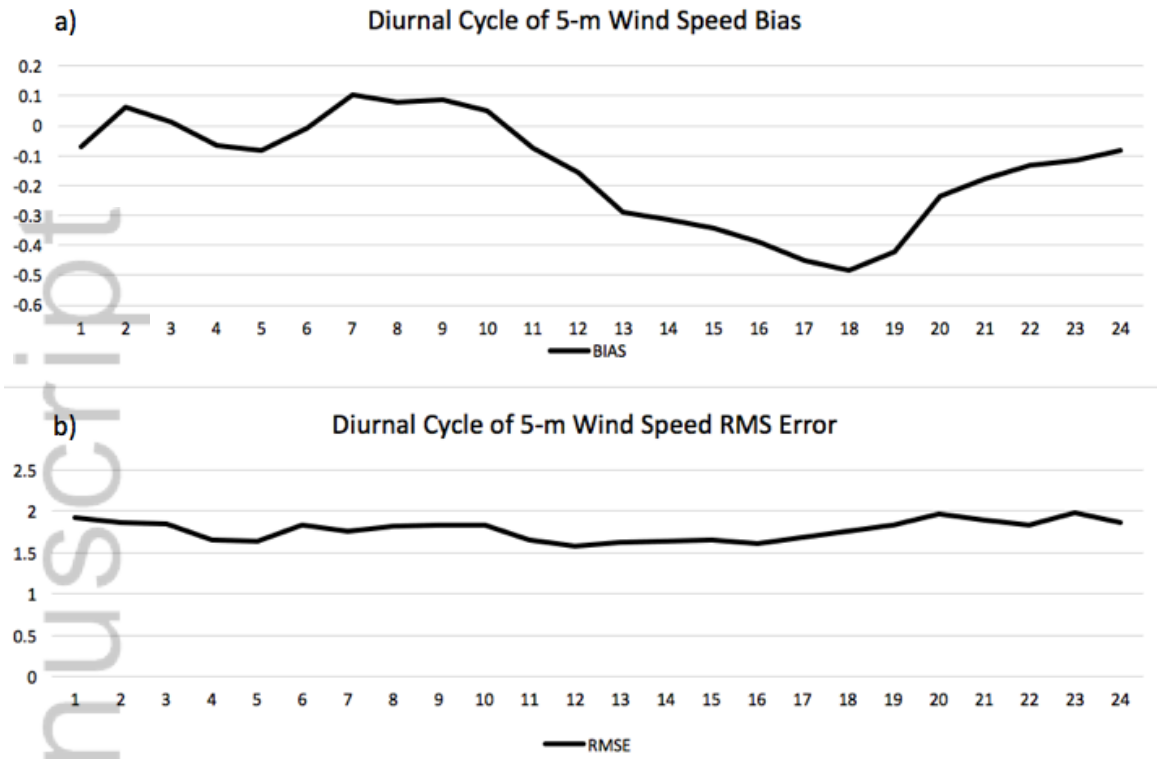

Fig. 4. Diurnal cycle of adjusted HRRR 1-h forecast (a) 5-m wind speed bias (m s^{-1}) and (b) 5-m wind speed RMS error (m s^{-1}) at Buoy 44065 (New York Harbor). The horizontal axes are in hours (UTC).

3. Results for the northeastern United States Atlantic offshore region

In this section, we present our analysis of the HRRR model 80-m wind forecasts composite for this specific region. Note that the HRRR dataset covers the entire coast of the contiguous US; more detailed analysis is undertaken for the

northeastern US because offshore wind projects have made the most progress in this region. To aid the reader in following the discussion, Fig. 5 shows the local terrain and coastal geography, in addition to offshore bathymetry.

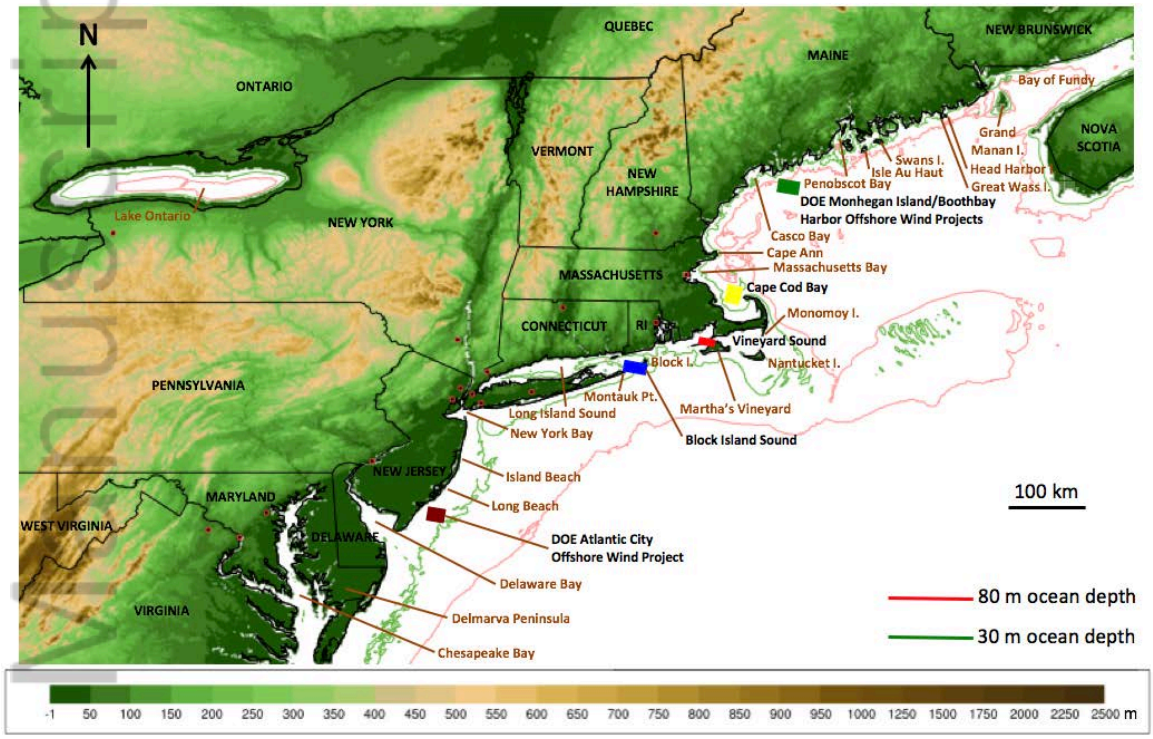

Fig. 5. Map of the northeastern CONUS showing terrain height above sea level (color fill; m), as well as the 30-m (green) and 80-m (red) bathymetry contours. The five offshore wind regions used for seasonal-variation calculations (see text) are shown as colored blocks: the DOE Monhegan Island/Boothbay Harbor Offshore Wind Projects (green), Cape Cod Bay (yellow), Vineyard Sound (red), Block Island Sound (blue), and the DOE Atlantic City Offshore Wind Project (brown).

a. East Coast Offshore Wind Maps

Figure 6 shows the average 80-m wind speed in the New England region over the three years 2013-15. Over 22 000 1-h HRRR forecasts, each covering the HRRR area (Fig. 1) at 3-km resolution, went into this calculation. Over land, the most obvious feature is the presence of higher average winds over regions of high terrain in the northern Appalachians (see map in Fig. 5). Off the coast, there is less spatial variability, but the wind speed does increase with distance from the shore. Coastal 80-m wind speeds vary from as low as about 6.5 m s^{-1} in sheltered bays including the Chesapeake, Delaware, and Long Island Sound (see map in Fig. 5), up to about

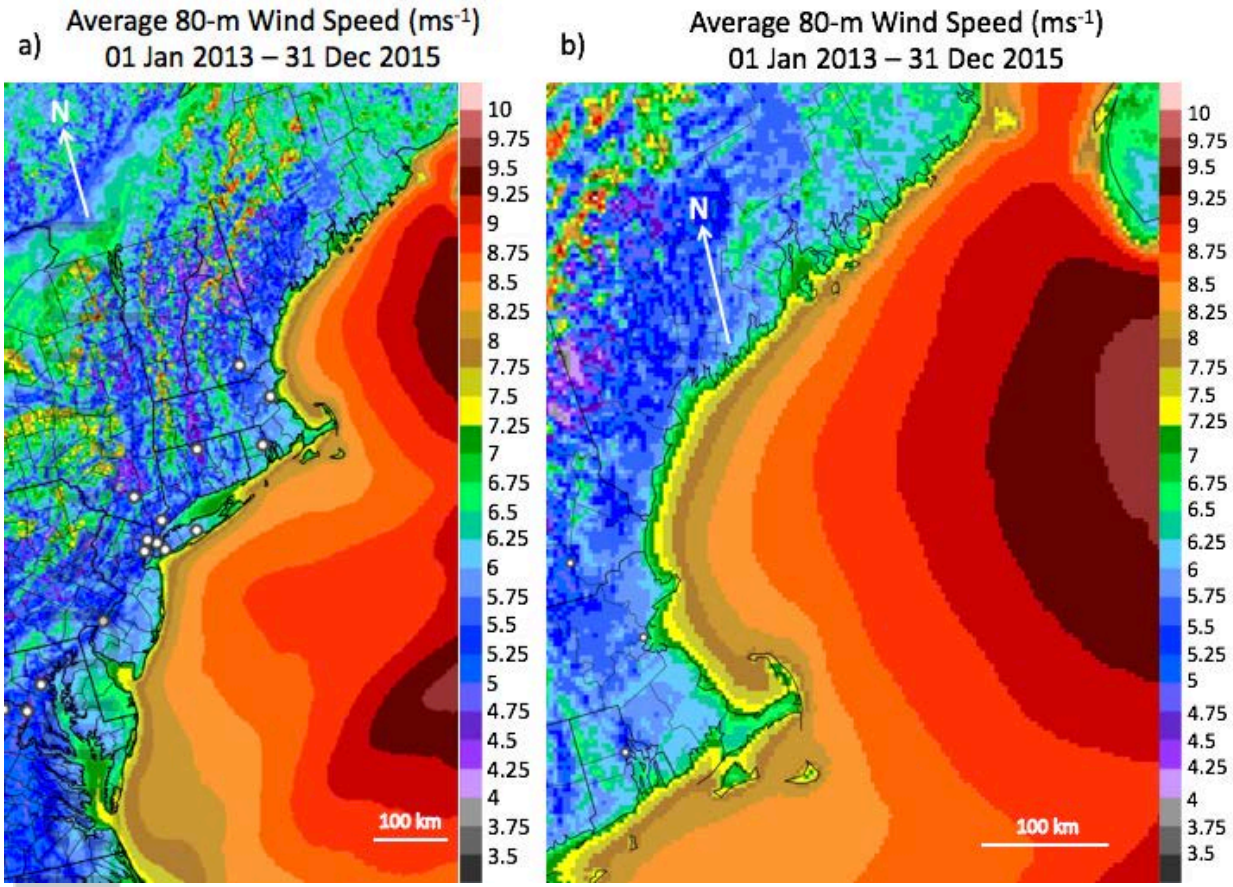

Fig. 6. Average 80-m wind speed from 1-h HRRR forecasts over the 2013-15 period, showing (a) the northeastern coast of the United States and (b) the Gulf of Maine.

8.25 m s^{-1} in more exposed portions of Cape Cod and eastern parts of the coast of Maine.

The magnitude of the offshore wind gradient varies along the coast of New England. A weaker wind speed gradient is seen immediately north and south of Cape Cod

(around 1.2-1.4 m s^{-1} per 100 km), with a stronger gradient to the east of Cape Cod, southeast of Long Island, and especially near the entrance to the Bay of Fundy (where the gradient approaches 2 m s^{-1} per 100 km). Focusing on the Gulf of Maine region (Fig. 6b), we see that this is also true in the very near-shore region, with significant variability in the proximity of the 8 m s^{-1} contour to the coastline.

To examine, in more detail, the nature of the 80-m wind speed probability density function at each 3-km grid point, we next present some maps of the exceedance frequency of several different wind speed thresholds derived by Clack et al. [48]: 4 m s^{-1}, which we consider to be near the bottom of a typical power curve; 12 m s^{-1} (near the top of a typical power curve), and 25 m s^{-1} (near the cut-out speed of a typical wind turbine). These frequencies are calculated over the three-year period of study (2013-15). Note that the specific values of the cut-in and cut-out speeds vary significantly among turbine models; our goal is merely to provide illustrative sample thresholds to demonstrate the utility of the dataset.

The 4 m s^{-1} frequency is shown in Fig. 7a. As was seen for the 3-year average wind speed, higher frequency of 4 m s^{-1} wind speeds encroaches closer to the coast to the south of Long Island and Rhode Island, and south of the far southeastern corner of Maine, with reduced frequencies southeast of Cape Cod and south of New Jersey.

Along the coast, 80-m winds generally exceed 4 m s^{-1} 76-84% of the time outside of bays and protected areas. The higher frequencies are relegated to outlying islands such as Block Island (RI) and the area around Great Waas and Head Harbor Islands in southeastern Maine.

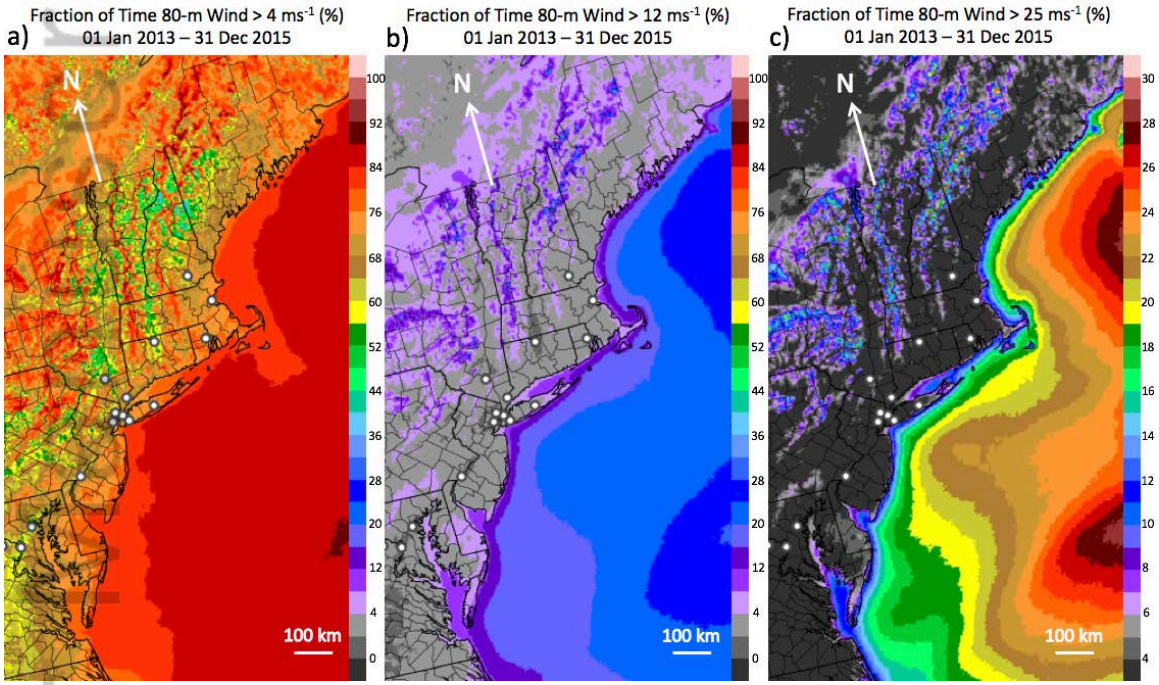

Fig. 7. Frequency of 80-m winds exceeding (a) 4 m s^{-1}, (b) 12 m s^{-1}, and (c) 25 m s^{-1} from 1-h HRRR forecasts over the 2013-15 period, showing the northeastern coast of the United States.

Figure 7b shows the frequency of exceedance of the 12 m s^{-1} threshold over the three years. This threshold shows stronger frequency gradients in the offshore environment, with shoreline values often below 8% but with greater than 16% within 30 km of the coast for much of the extent from New Jersey to Maine. Once again, nearshore gradients are weakest south of New Jersey (about 5% per 100 km), and increase northward to the entrance to the Bay of Fundy (near 15% per 100 km). The area of open water 100-200 km offshore to the south of Martha's Vineyard exhibits a weak far-offshore wind frequency gradient.

The exceedance frequency of the 25 m s^{-1} threshold is shown in Fig. 7c, using a different color scale. This wind speed value is near the point on the power curve where turbines typically need to shut down in order to prevent structural damage. The probability of winds of this magnitude is an additional consideration in wind resource prospecting. The frequency of 25 m s^{-1} winds is much smaller than the frequency of the lower thresholds; much less than 1% of the time in most areas. Values approach 0.5% in the center of the Gulf of Maine. The east coast of Cape Cod, and the western tip and eastern coast of Nantucket Island, have winds of this speed around 0.1-0.15% of the time (winds exceeding 25 m s^{-1} on an average of 8-14 h out of each year).

Examining these maps in concert, we can get a sense of the probability density function of wind speeds in the nearshore environment. The region to the south of Long Island, along the coast of New Jersey, is characterized by moderately strong average wind speeds (in the vicinity of 7.5 m s^{-1}); this appears to be due to the encroachment of winds greater than 12 m s^{-1} closer to the coastline here, especially near the inflection point between Long Beach and Island Beach (east of Philadelphia). Farther south, along the Delmarva Peninsula, the offshore wind gradient is weaker; 12 m s^{-1} winds occur less than 20% of the time even 200 km east of the southern tip of the Delmarva Peninsula.

The south shore of Long Island appears similar to the New Jersey coast in terms of the wind distribution, although in our dataset there is some indication of less frequent extreme wind speeds (winds stronger than 25 m s^{-1}). Long Island Sound, on the other hand, appears much less windy by all measures. There is a significant eastward gradient in windiness along the coasts of Connecticut and Rhode Island, with the south shore of Rhode Island appearing very similar in its wind distribution to the south shore of Long Island.

Montauk Point, at the eastern tip of Long Island, as well as Block Island farther to the east, appear to have a wind distribution shifted towards higher wind speeds.

Winds greater than 4 m s^{-1} appear about the same amount of time as other coastal areas, but 12 m s^{-1} winds are more common (up to 17% occurrence frequency). The western tip of Martha's Vineyard experiences similar conditions. Nantucket Island, Monomoy Island, and the eastern shore of Cape Cod have even higher average wind speeds (as high as 8 m s^{-1}); this comes from increased frequencies of 12 m s^{-1} winds, as well as significant probabilities of 25 m s^{-1} winds. It is likely that the frequent occurrence of winds between 12 and 25 m s^{-1} is responsible for the high mean wind speeds in this region.

Relatively low average coastal wind speeds are seen in the region between Boston and Casco Bay in southern Maine, with the exception of Cape Ann. It appears that the concavity of the coast in this area with land friction effects from Cape Cod and eastern MA on predominantly south-southwesterly winds reduces the likelihood of high winds. Farther northeast, along the coast of Maine, average winds are higher. The complex coastline in this region seems to provide both sheltered bays where wind speeds are quite low, as well as exposed islands and tips that are among the windiest spots along the northeastern coast of the US. The outlying islands to the southeast of Penobscot Bay (Isle au Haut and Swan Island) have average wind speeds over 8 m s^{-1}, and their southeast coasts experience winds greater than 12 m

s^{-1} about 18% of the time. Grand Manan Island (in the Bay of Fundy) appears to have similar conditions.

b. Seasonal and diurnal wind variability for northeastern US Atlantic coast area

Turning our attention now to seasonal wind speed changes (Fig. 8; note that December 2012 is included in order to perform the calculation for three consistent winter [DDJ] seasons), we see that the frequency of high winds in the offshore region exhibits a large seasonal cycle. It is apparent that the gradient of offshore wind speeds reaches a maximum during the winter months (Dec – Feb), and a

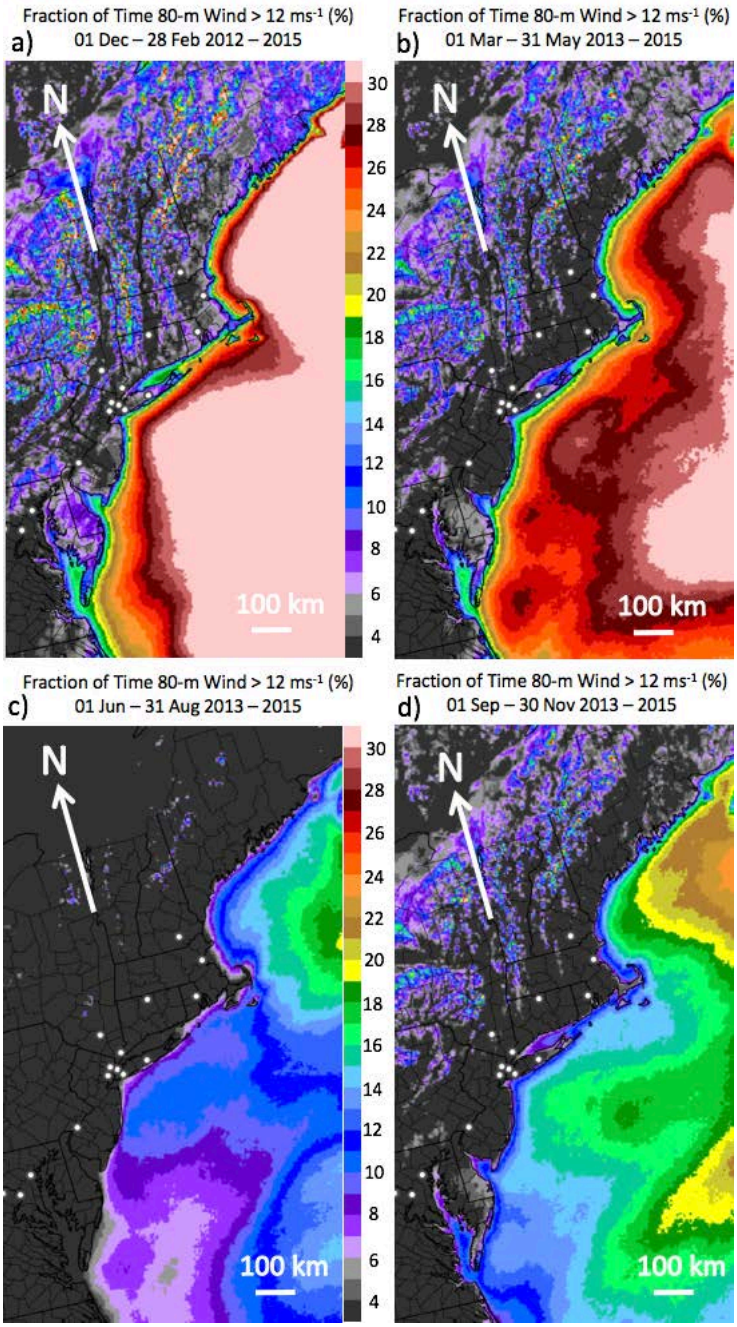

Fig. 8. Frequency of 80-m winds exceeding 12 m s^{-1} during (a) 1 Dec – 28 Feb 2012-13, 2013-14, and 2014-15; (b) 1 Mar – 31 May 2013 – 2015; (c) 1 Jun – 31 Aug 2013

– 2015; and (d) 1 Sep – 30 Nov 2013 – 2015 from 1-h HRRR forecasts, showing the northeastern coast of the United States.

minimum in the summer (Jun – Aug). The stronger wintertime gradient is manifested in the closer proximity of more frequent high winds offshore, but only a modest increase in coastal wind speeds (Fig. 8a). Frequency of 80-m winds exceeding 12 m s^{-1} more than 9% of the time during the high-energy load in summer (Fig. 8c) skirts Montauk Point, Block Island, and Cape Cod.

For offshore wind energy development near the highly populated east coast of the CONUS, there is also great interest in the diurnal variability of the resource as compared with the diurnal variability of the power load during the high-demand summertime period. To examine this, we break down the results by time of day (Figs. 9), with 15-00 UTC valid times representing daytime (from HRRR runs initialized between 14 and 23 UTC), and 03-12 UTC valid times representing nighttime (from HRRR runs initialized between 02 and 11 UTC). These times represent 10-19 Eastern Standard Time (EST) for the daytime hours, and 22-07 EST for the nighttime hours over the eastern CONUS.

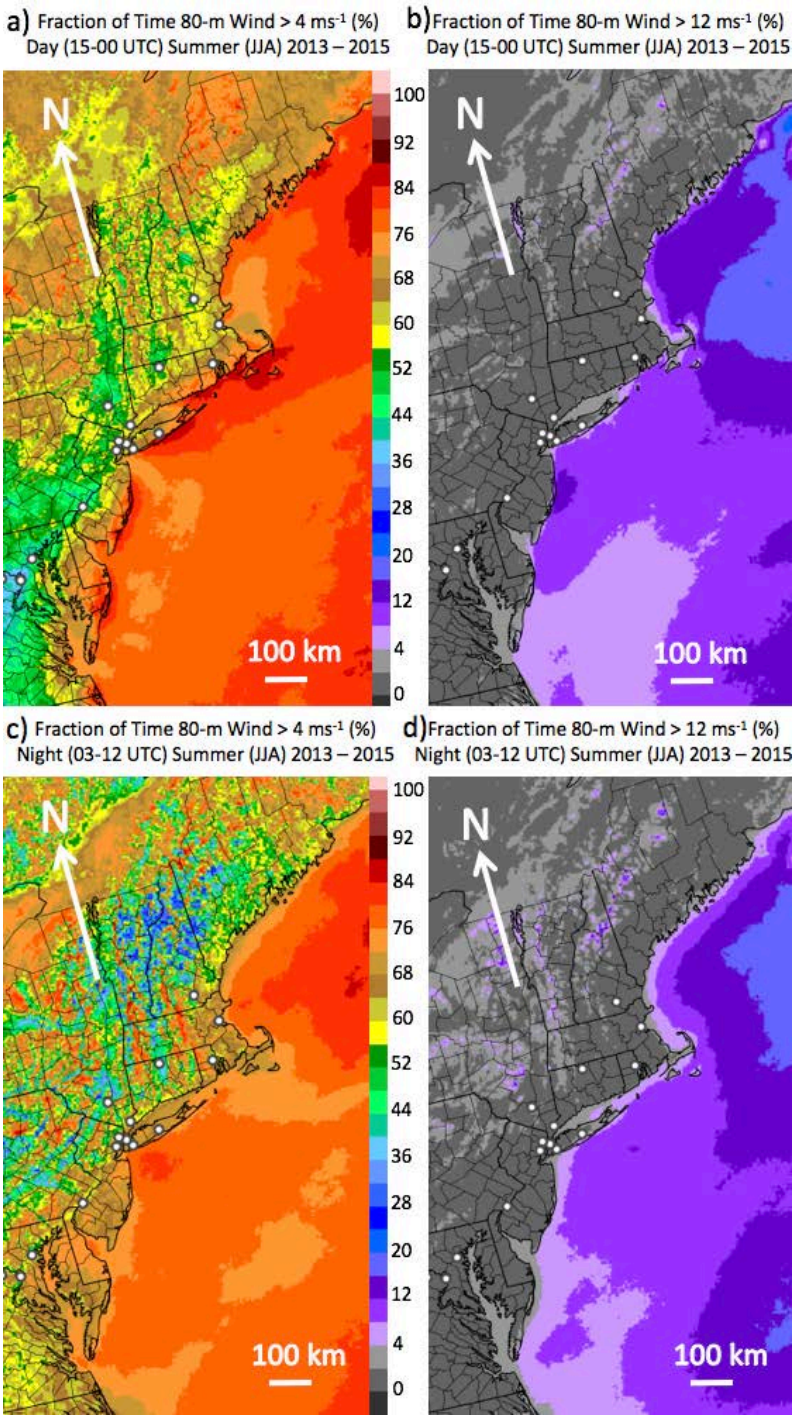

Fig. 9. Frequency of 80-m winds exceeding (a,c) 4 m s^{-1} and (b,d) 12 m s^{-1} during (a,b) the daytime hours (valid during 15-00 UTC) and (c,d) the nighttime hours (valid during 03-12 UTC) in the summer (1 Jun – 31 Aug 2013 – 2015) from HRRR 1-h forecasts, showing the northeastern coast of the United States.

Figure 9a shows the daytime frequency of wind speeds greater than 4 m s^{-1} during the summers (June-August) of 2013-15. Figure 9b shows the corresponding frequencies of 12 m s^{-1} wind speeds. Nighttime frequencies are shown in Figs. 9c,d. Many interesting features emerge when the averages are computed separately for daytime and nighttime. One of the primary features is the presence of sea breezes during the daytime over the topographically simple coasts of the Delmarva Peninsula, southern New Jersey, Long Island, and eastern Connecticut, Rhode Island, and Massachusetts. The sea breeze signature (i.e., the presence of strongest winds along the coastline) is particularly prominent in the 4 m s^{-1} frequencies (Fig. 9a), although the New Jersey and Delmarva sea breezes apparently sometimes exceed 12 m s^{-1} in speed (up to about 15% of the time during the day; Fig. 9b). As we would physically expect, the 4 m s^{-1} sea breeze signature is centered at the coast, but extends several tens of kilometers inland and offshore. Evaluation of buoy observations at Ocean City Inlet (location shown in Fig. 2, purple star) reveals that, for each summer of 2013-15, wind speeds reach their diurnal maximum at 21 UTC

(which corresponds to 17 EST), with average winds from a southerly or southeasterly direction during the afternoon, which is consistent with sea breeze behavior. Sea breeze signatures also appear along the coast of Maine. Less frequent 4 m s^{-1} winds are seen near major bays and indentations in the coast, particularly around New York Harbor and just off the tip of Cape Cod.

The presence of the highly predictable and well-understood sea breezes along the New Jersey and Delmarva coasts could play an important role in offshore wind energy development. The strongest sea breeze winds are seen very close to the coast, which limits the challenges related to construction and electricity transport. Another important point is that sea breezes are strongest during periods of quiescent synoptic weather, which also tend to be the hottest periods (i.e., periods of highest electricity demand) during the summertime.

Winds are only slightly weaker during the nighttime over most of the coastal region, with the frequency of exceedance of the 4 m s^{-1} threshold decreasing from >84% to >72% (Fig. 9c,d), although winds are slightly stronger in the bays and coastal indentations.

b. Wind regimes of the nearshore environment

Another way to visualize the spatial and time variability of the 80-m wind field in the HRRR is to average over interesting regions and then look at time series. The five sites picked for this study are shown in the map in Fig. 5; two sites are DOE offshore wind energy project locations [49], and the other three are in different parts of the nearshore environment. Figure 5 shows two offshore bathymetry contours at 30 m depth and 80 m depth. The value of 30 m is considered an important threshold; anchoring wind turbines in water deeper than this is significantly more costly. The 80-m depth threshold outlines the limits of current economically viable anchoring technology, although interest is growing in floating platforms [49].

We can use our dataset to plot time series of the fraction of time above the 4, 12, and 25 m s^{-1} thresholds at these five offshore locations during 2013, 2014, and 2015 (Fig. 10). It is seen from these plots that there is a significant annual cycle in the

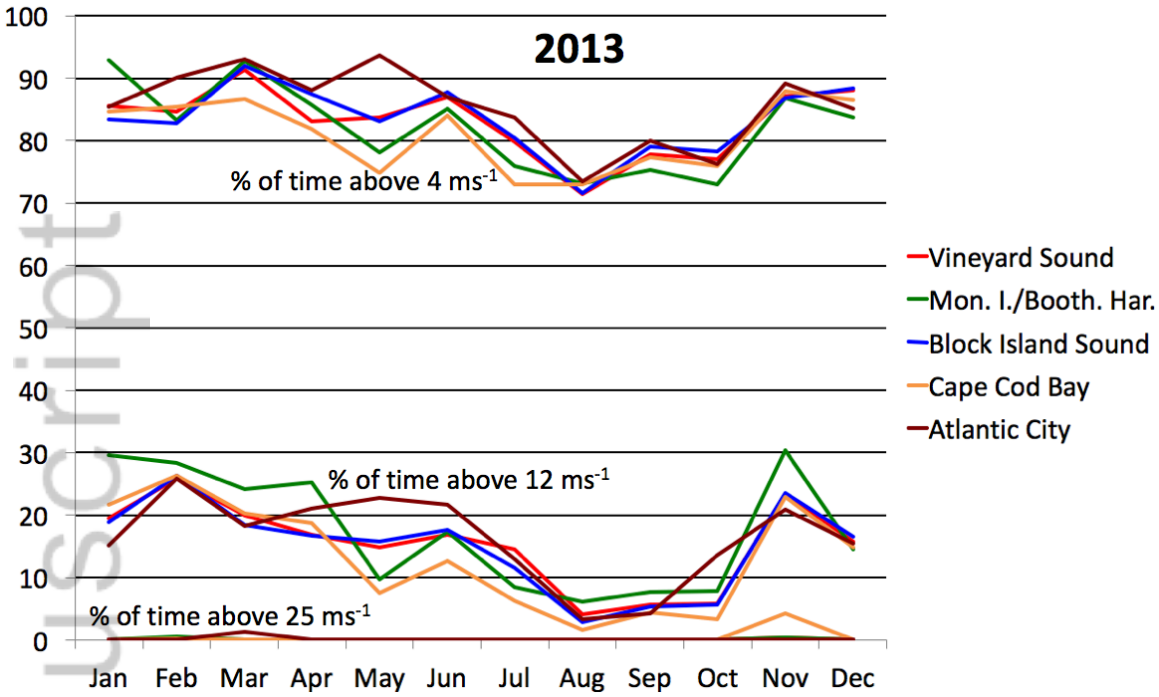

Fig. 10. Frequency of 80-m winds exceeding 4 m s^{-1}, 12 m s^{-1}, and 25 m s^{-1} at the five offshore wind regions shown in Fig. 5 during (top) 2013, (bottom) 2014, and (next page) 2015, from HRRR 1-h forecasts.

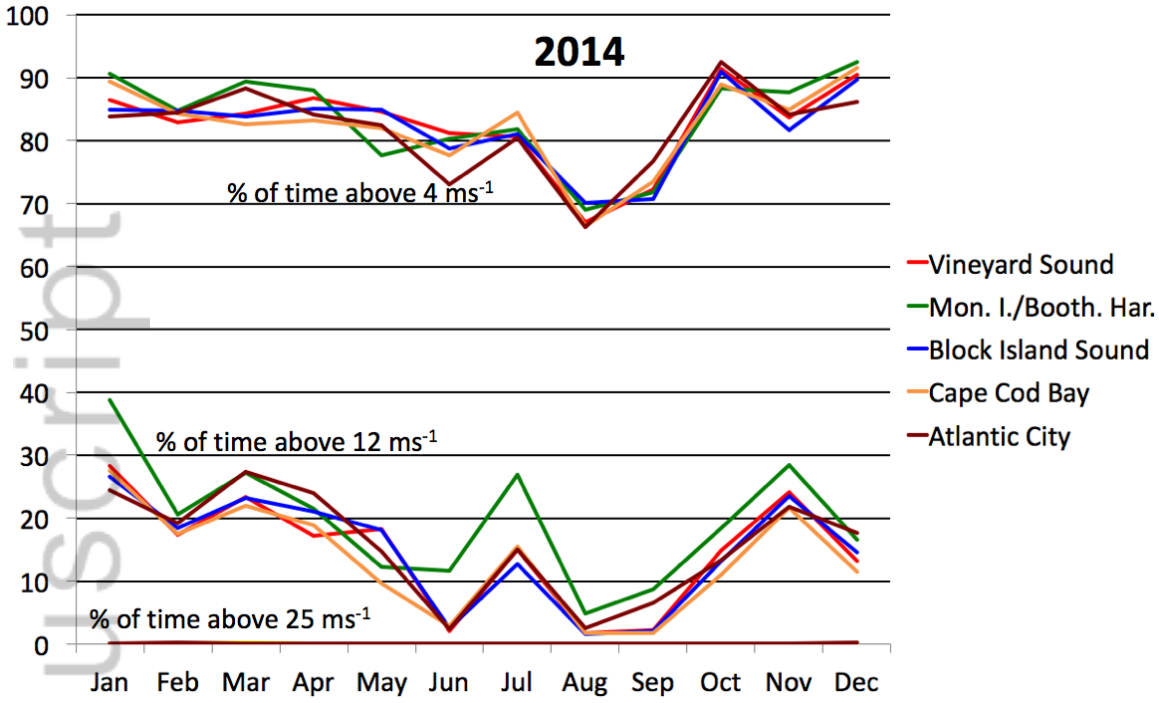

Fig. 10. (continued)

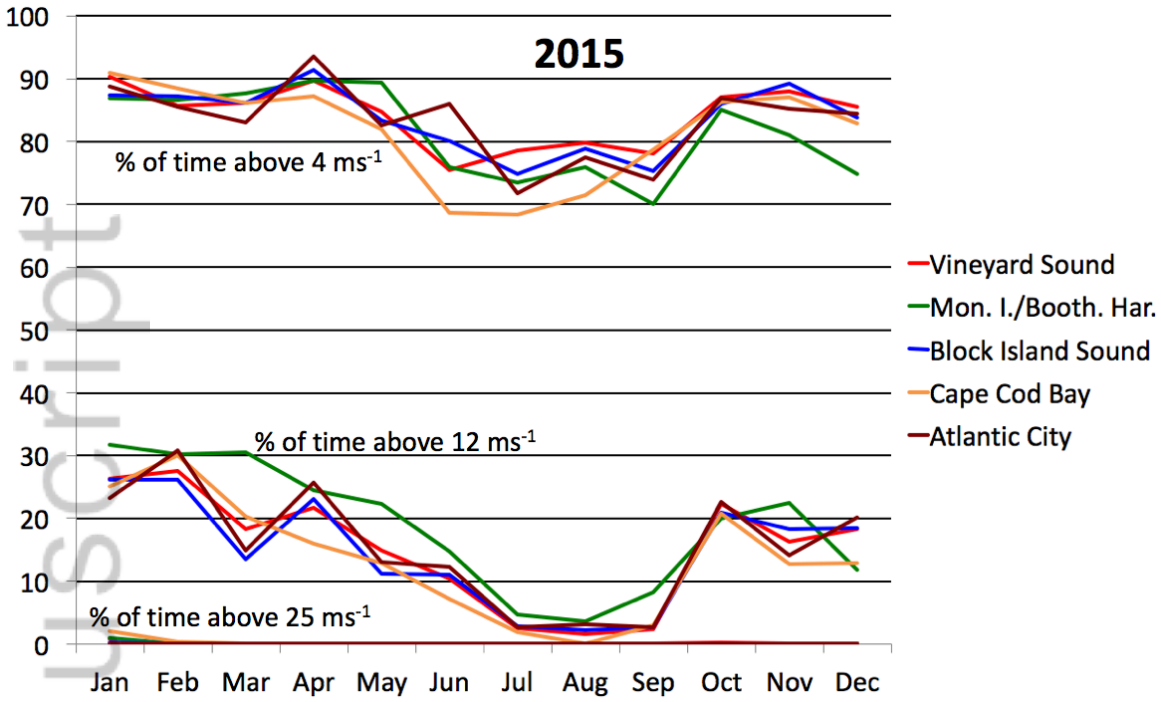

Fig. 10. (continued)

fractions of time above the 4 and 12 m s^{-1} thresholds. Exceedance of the higher wind threshold of 25 m s^{-1} is a very infrequent event in the estimate of truth from the 3-km HRRR model, occurring only several hours per year. 80-m winds are most frequently high in the winter and spring at all sites, and lowest in the summer (with a minimum generally in August). The summer of 2015, especially the month of July, featured particularly light winds at all sites. Some of the regions display similar behavior due to geographical proximity, particularly Vineyard Sound (MA) and Block Island Sound, and also Monhegan Island / Boothbay Harbor (ME) and Cape

Cod Bay. For example, the late spring and early summer of 2013 was quite windy at both Vineyard Sound and Block Island Sound.

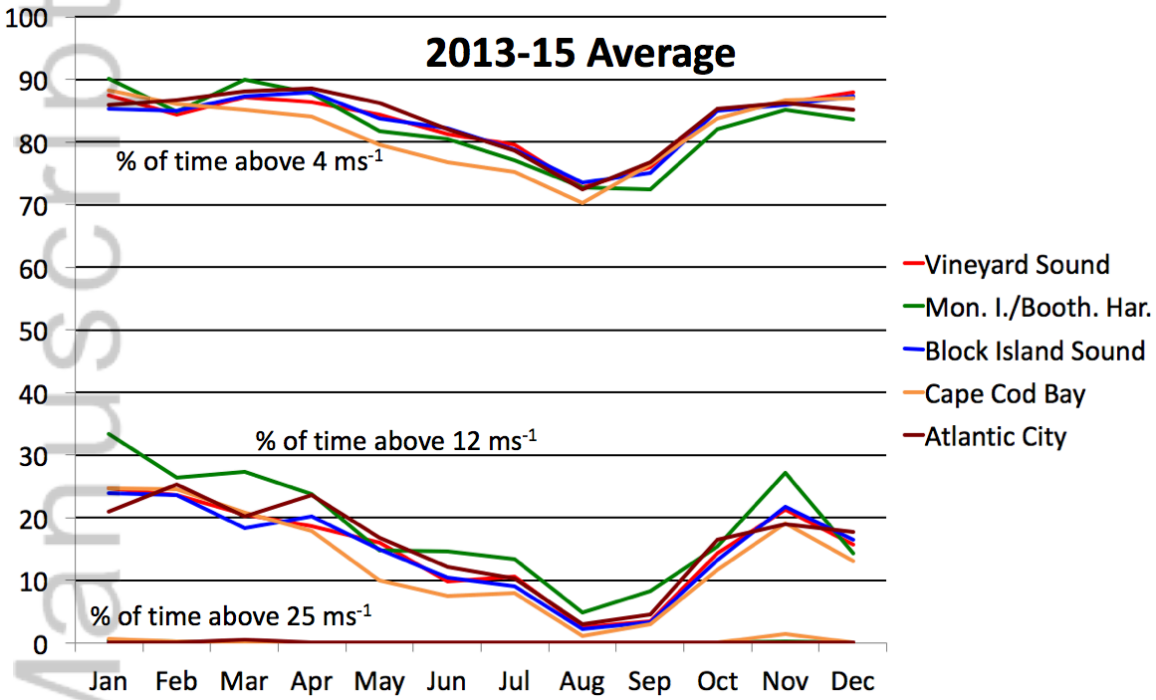

Fig. 11. As in Fig. 10, but for the three-year average from 2013 – 2015.

Averaging the three years together allows us to generalize the seasonal cycle at these five sites (Fig. 11). Monhegan Island/Boothbay Harbor (ME), the northernmost of these five sites, has the most frequent 12 m s^{-1} winds during nearly every month, while the frequency of 4 m s^{-1} winds here is not much different from that seen in the other regions. Cape Cod Bay appears to have the least frequent high

winds during the spring and autumn months, while in the wintertime it is comparably windy to many of the other sites. The Atlantic City region seems to be the windiest region during the late spring months of April and May. As can be seen in Fig. 10, there is a considerable amount of interannual variability in the month-to-month winds. This makes it challenging to draw conclusions about the long-term climatology of the region (i.e., an "average" year) and the relative windiness of each of the sites. In the future, this 3-year study could be extended to include additional years, which would produce more robust results.

4. Results for other contiguous US offshore regions

Several other regions within the nearshore waters of the continental United States have been considered for offshore wind development over the last few years. A useful reference here is an overview of 80-m wind average over the entire HRRR domain covering the contiguous US for this same 2013-2015 period, as shown by James et al. [27; see their Fig 7a]. In this section, we focus on local maps of some average wind metrics over these additional regions with local maxima for potential offshore wind energy.

a. Great Lakes

While not an oceanic offshore wind region, the Great Lakes comprise a large enough area of open water that they experience significantly stronger winds than the surrounding land areas. Figure 12 shows the three-year average 80-m wind speed over the Great Lakes from our dataset. We see that the maximum average 80-m wind speed varies among the Great Lakes, with Lake Superior being the windiest (maximum average 80-m wind speed over 8.5 m s^{-1}), followed by Michigan and Huron (8.25 m s^{-1}), then Erie and Ontario (8 m s^{-1}). Generally, the northern and western shores of the lakes are less windy, while the southern and eastern shores are windier.

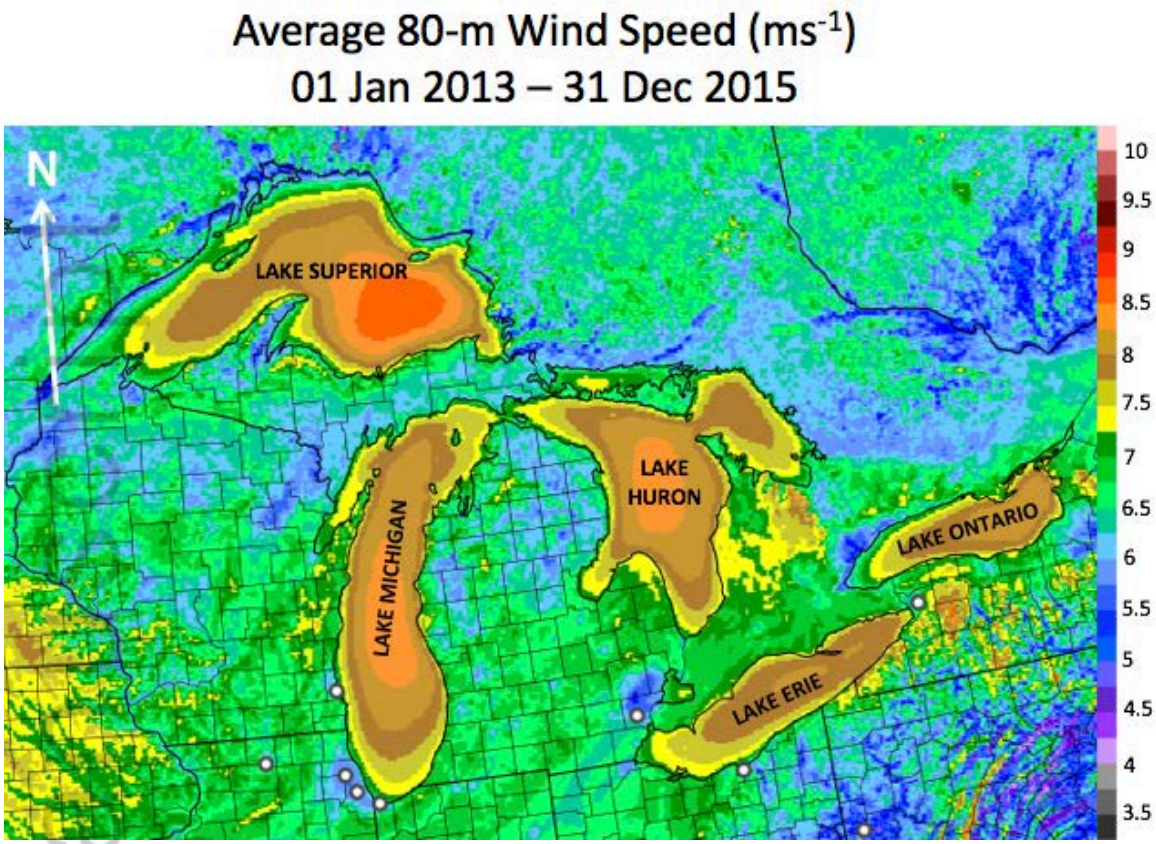

Fig. 12. As in Fig. 6, but for the Great Lakes.

We can also plot, as before, the exceedance frequencies of the wind speed thresholds of 4 and 12 m s^{-1} (Fig. 13). Once again, we see slightly higher exceedance frequencies for the upper (western) Great Lakes. Areas with at least 16% frequency of 80-m winds greater than 12 m s^{-1} (Fig. 13b) approach lakeshores most closely on the eastern sides of Lake Michigan (near western MI) and Lake Huron (in ON), offshore from the thumb of lower Michigan, and the southeastern shores of Lake

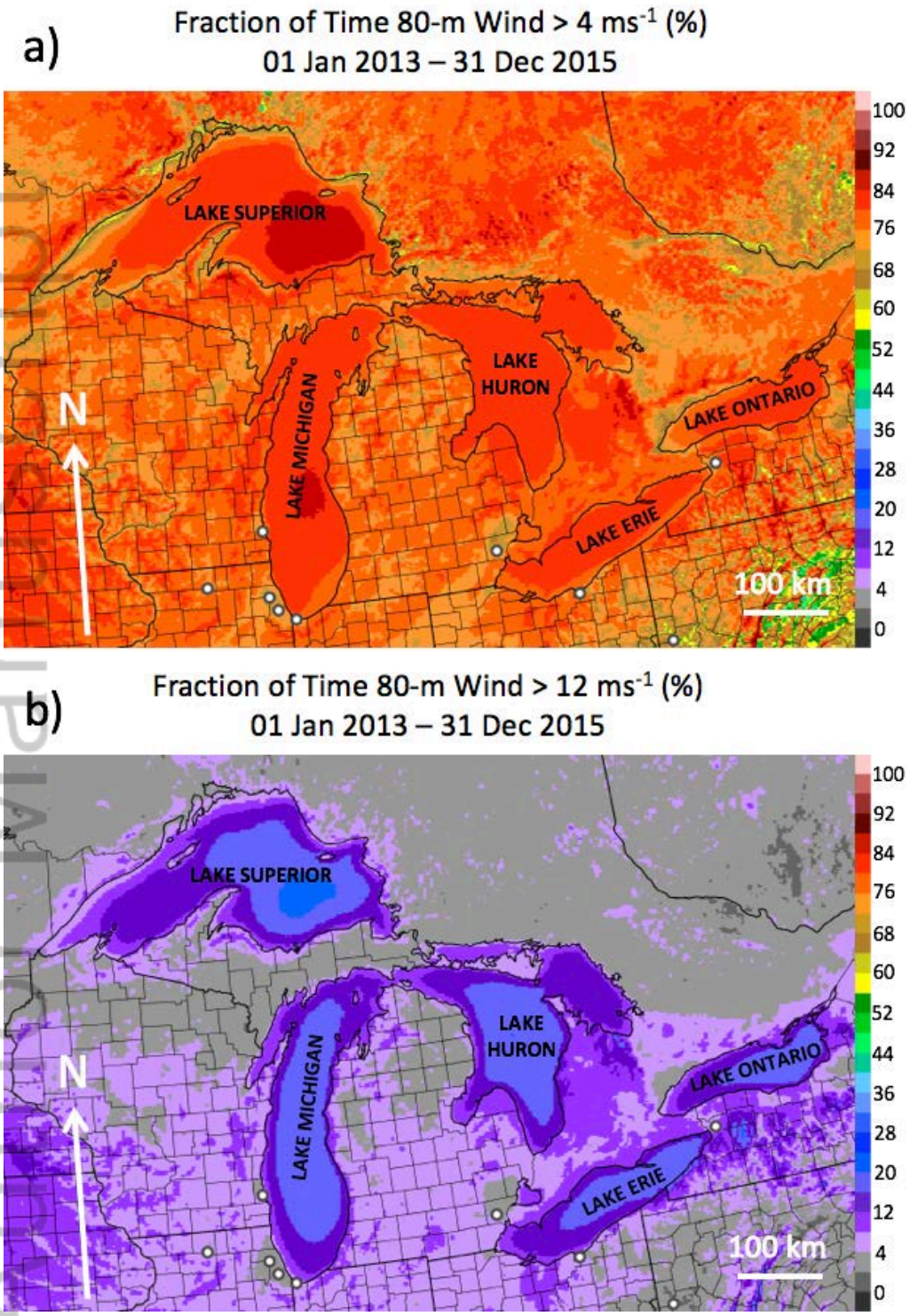

Fig. 13. Frequency of 80-m winds exceeding (a) 4 m s^{-1}, and (b) 12 m s^{-1} from 1-h HRRR forecasts over the 2013-15 period, showing the Great Lakes.

Erie (near its PA and NY lakeshores) and Lake Ontario (near its NY lakeshore). These nearshore frequencies are comparable to those at similar distances from the Atlantic coast of the northeastern US (Fig. 7).

b. Atlantic Coast of the Carolinas

While the southeastern United States are generally thought to have only minimal wind resources, the region offshore of the Carolinas experiences winds only slightly less than those farther north along the New England coast. Figure 14 shows the average 80-m wind speed for this region from our dataset. Average winds greater than 8 m s^{-1} exist within about 100 km of the coast of North Carolina.

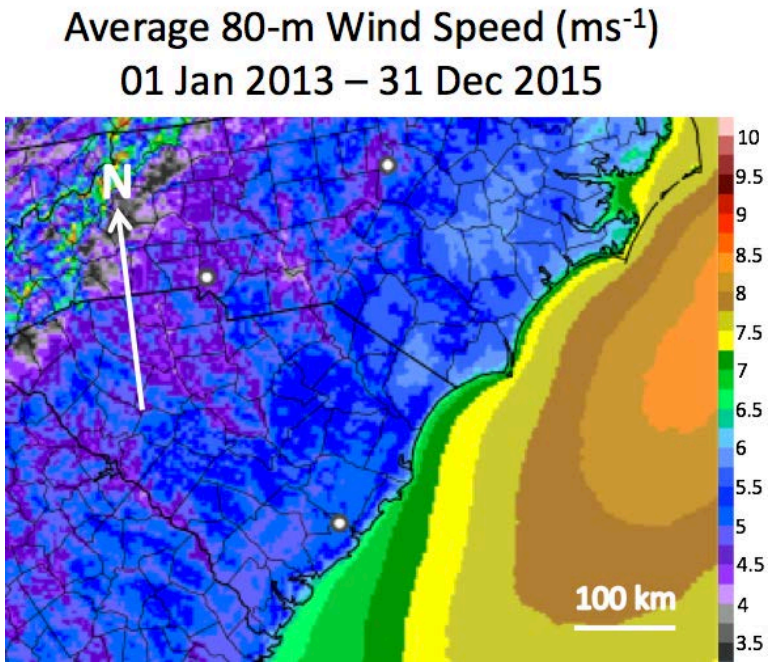

Fig. 14. As in Fig. 6, but for the Atlantic coast of the Carolinas.

The outer banks of North Carolina extend a considerable distance out into the offshore wind speed gradient, with average wind speeds reaching close to 8 m s^{-1}. Farther south along the coast of South Carolina, average wind speeds are lower, but 7 m s^{-1} winds remain within about 20 km of the coast in the eastern part of the state.

Figure 15 shows the frequency of 4 and 12 m s^{-1} winds in the Carolinas offshore region. The southeastern coast of North Carolina experiences 4 m s^{-1} winds about 80% of the time, while frequencies are slightly lower in South Carolina. The frequency of 12 m s^{-1} winds varies from about 14% on the Outer Banks (NC) down to about 4% along the far southern coast of South Carolina.

c. Gulf Coast of southern Texas

Another region that stands out on national maps of long-term average wind speed [25] is the Gulf Coast of southern Texas. As can be seen in Fig. 16, average wind speeds reach up to nearly 8 m s^{-1} off the coast between Brownsville and Corpus Christi. According to the HRRR forecast dataset, these winds occur on the immediate coast of Padre Island, and extend out several tens of km offshore. Winds of 7 m s^{-1} average wind speed extend north along the coast towards Matagorda Bay, and southward along the coast of Tamaulipas in northern Mexico.

Looking at the exceedance frequencies of the 4 m s^{-1} and 12 m s^{-1} thresholds (Fig. 17), we see that the highest 4 m s^{-1} frequencies occur in regions with the highest

a) Fraction of Time 80-m Wind > 4 ms^{-1} (%)
01 Jan 2013 – 31 Dec 2015

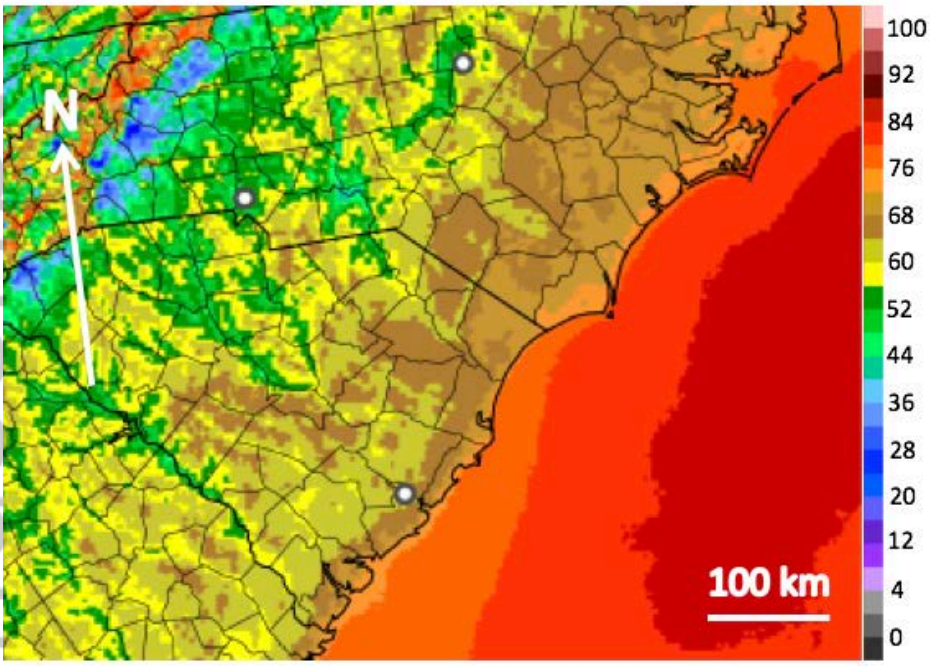

b) Fraction of Time 80-m Wind > 12 ms^{-1} (%)
01 Jan 2013 – 31 Dec 2015

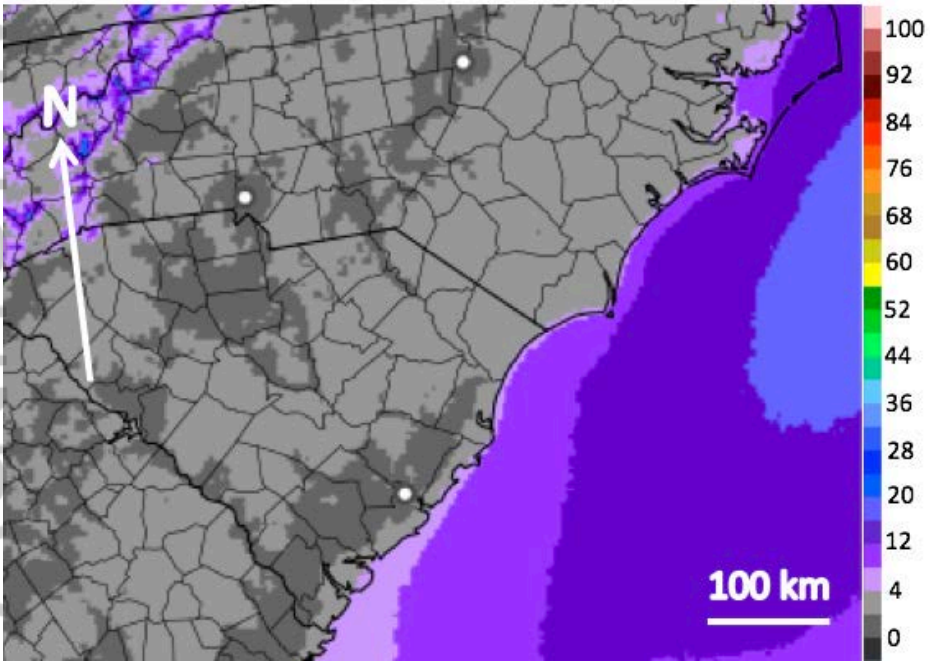

Fig. 15. As in Fig. 13, but for the Atlantic coast of the Carolinas.

average wind speed (84-88% of the time in areas where the average wind speed is greater than 7.25 m s^{-1}). In our three-year dataset, the frequency of 12 m s^{-1} winds show an interesting pattern, with a region of higher frequencies (although still fairly low; 8-12%) extending northeastward into the Gulf away from southern Texas roughly parallel to the Texas coast. This may be a signature of frontogenesis in this region, since cold fronts are the main mechanism for high winds here; Gulf of Mexico extratropical cyclones are relatively common during the cool season, particularly during El Nino years.

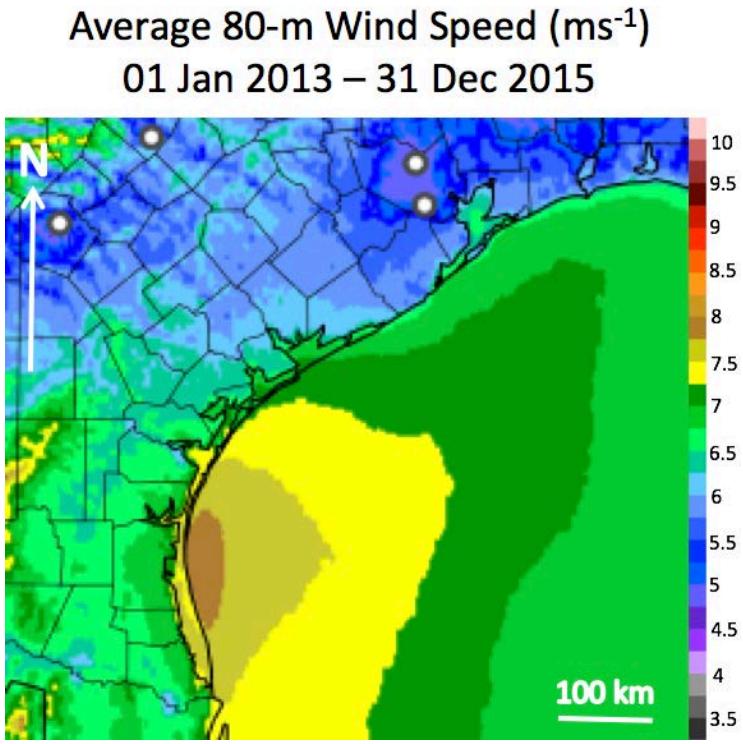

Fig. 16. As in Fig. 6, but for the Gulf Coast of southern Texas.

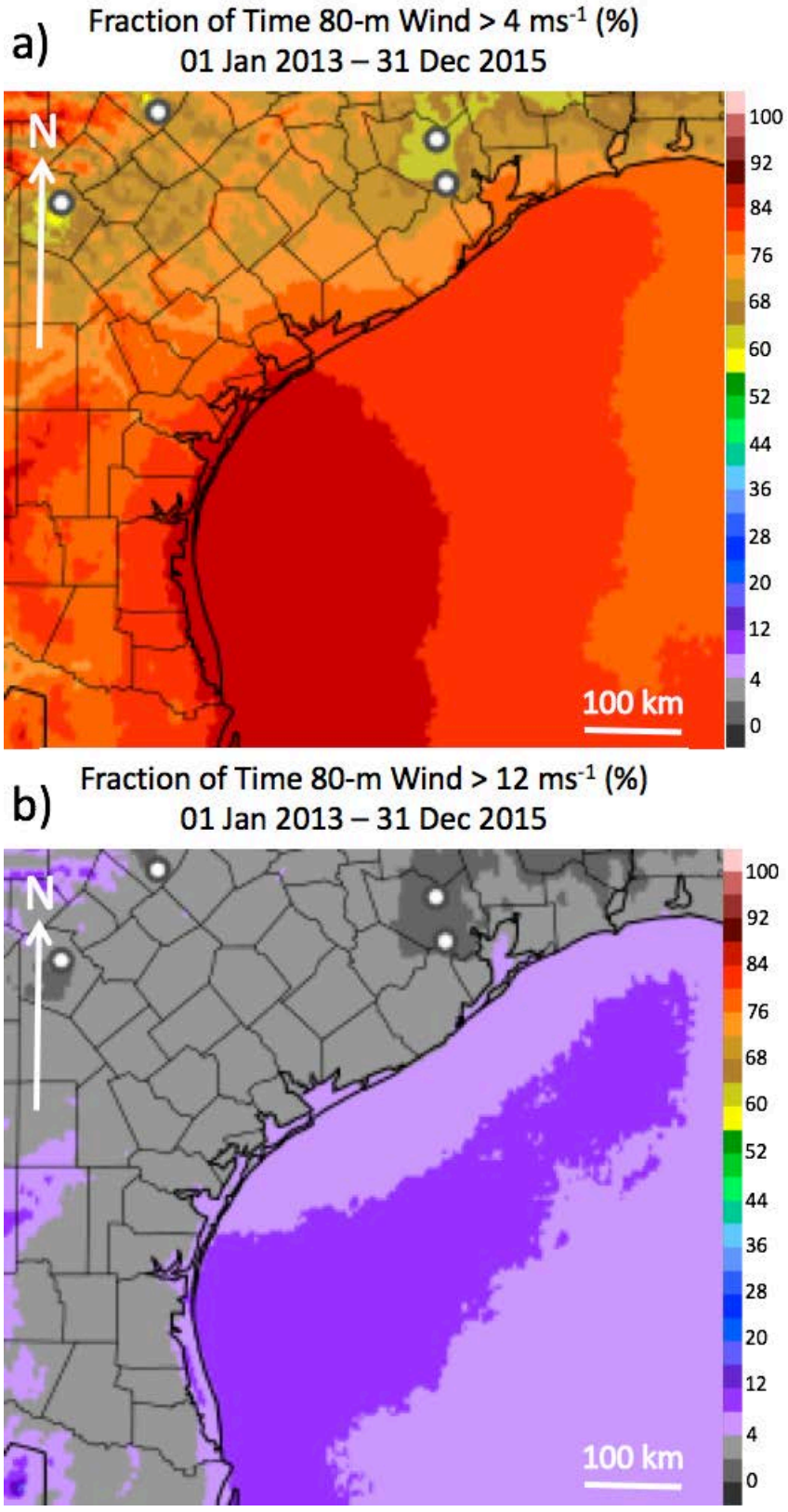

Fig. 17. As in Fig. 13, but for the Gulf Coast of southern Texas.

d. Pacific Coast of Oregon and northern California

There has, as yet, been little investigation of wind resources on the west coast of the CONUS due to the close proximity of deep water to the coastline. However, this region is home to the strongest 80-m winds in the entire HRRR domain. Figure 18 shows the average 80-m wind speed along the US West Coast over the three-year period of record. There is much fine-scale structure even in the mean 80-m wind field in this region, due to the complex topography of the coast and the semi-permanent northerly jet that exists off the coast, parallel to the coast ranges. Pronounced wind speed acceleration occurs immediately downwind of major tips and capes along the coast ("expansion fans"; [50]), particularly Cape Blanco in southwestern Oregon, and Cape Mendocino in northwestern California. Average coastal wind speeds vary from less than 7 m s^{-1} away from these capes, to 8-9 m s^{-1} in the maximum of the tip jets. The maximum average wind speeds in the tip jets exist approximately 10-20 km offshore, with enhanced wind speed zones surrounding these jets by ~50 km or so. The maximum average wind speed in the Cape Mendocino tip jet is nearly 10 m s^{-1} according to our three-year dataset.

Now looking at the exceedance frequency maps for this region (Fig. 19), we see that the tip jets have very little signature in the 4 m s^{-1} frequency maps, indicating that winds exceeding this strength frequently occur outside of the tip jet phenomenon

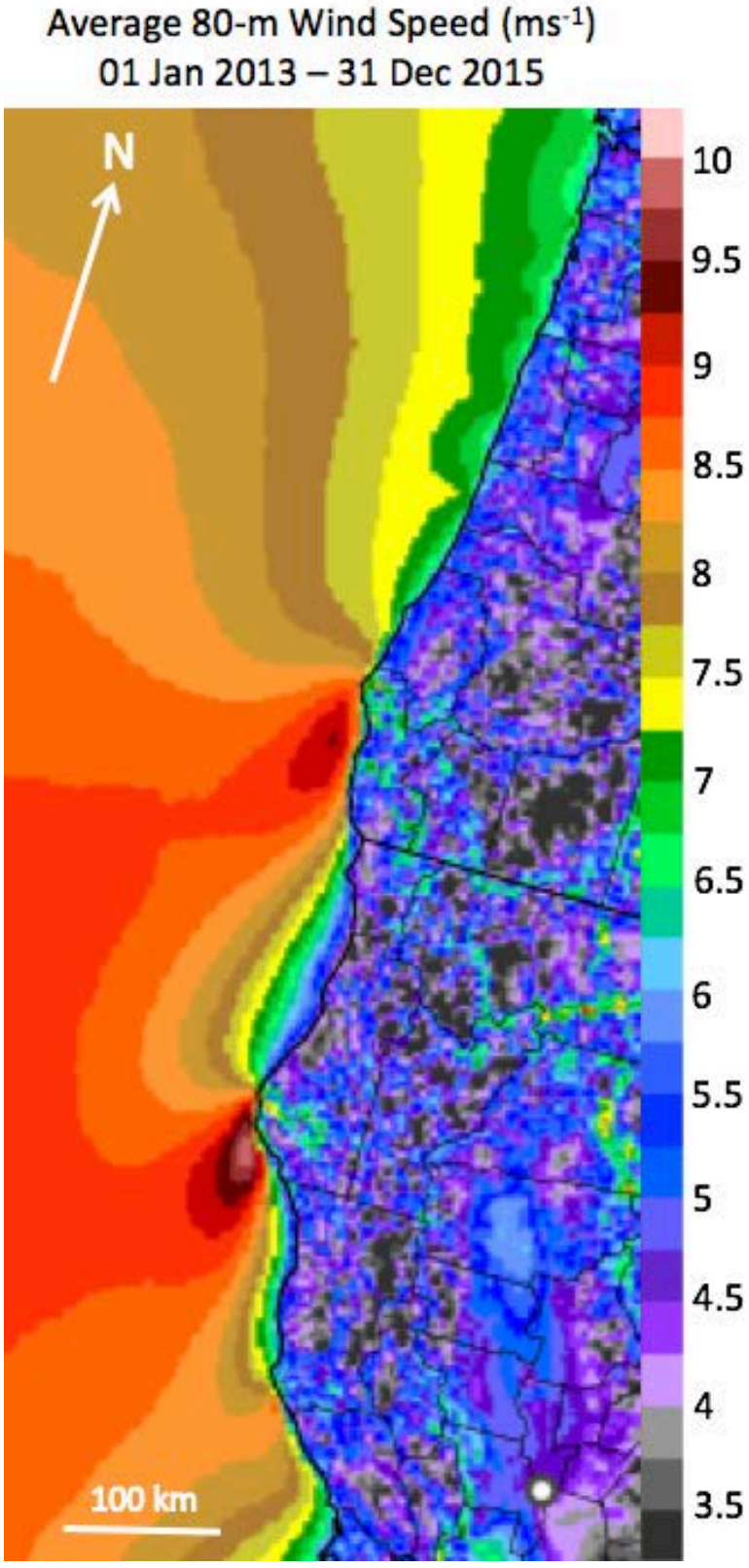

Fig. 18. As in Fig. 6, but for the Pacific coast of Oregon and northern California.

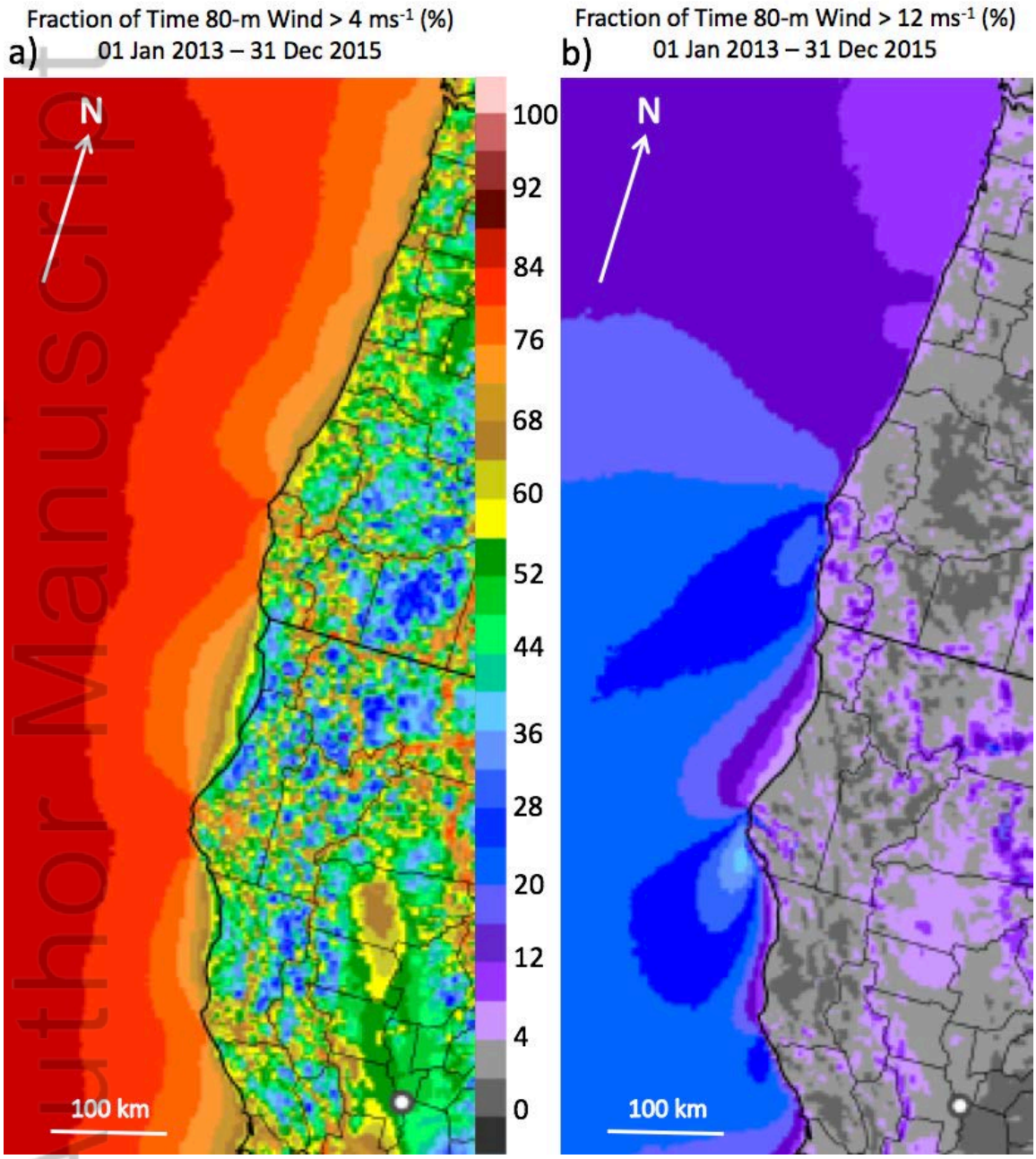

Fig. 19. As in Fig. 13, but for the Pacific coast of Oregon and northern California.

with larger-scale forcing. Still, Cape Mendocino itself has winds greater than 4 m s^{-1} about 80% of the time. The tip jets show up strongly in the frequency of 12 m s^{-1} winds, with cores exceeding this frequency about 30-40% of the time. A lesser tip jet off Point Arena farther south in California also shows up in the 12 m s^{-1} frequencies, having frequencies greater than 24% (corresponding to average wind speeds of about 8.5 m s^{-1}).

6. Discussion and conclusions

The dataset presented in this paper represents an initial step towards using NWP model output, which features hourly data assimilation and advanced model physics, to estimate offshore long-term average wind speeds for renewable energy purposes for the contiguous United States. Since observational datasets in the offshore region are so sparse in their spatial and temporal coverage, such NWP-based data has an important role to play in the process of assessing offshore wind resources. The advent of the convection-allowing 3-km HRRR model into NOAA operational modeling [18], along with its hourly refresh rate, permits the resolution of mesoscale features related both to meteorology and to the coastal geography, which

allows for improved analyses and forecasts. This paper complements the land-centered 80-m wind study by James et al. 2017 [27].

Five distinct offshore regions for wind energy potential were examined in this study, representing areas with large existing wind resource near US land areas: the northeast US Atlantic coast, the Great Lakes, the Carolinas coast, the south Texas Gulf coast, and the Pacific coast. To provide a more useful dataset, frequency maps for 80-m winds exceeding thresholds of 4 m s^{-1} (typical cut-in speed for turbines), 12 m s^{-1} (near the top of a typical turbine power curve), and 25 m s^{-1} (typical cut-out speed) were added to the overall mean 80-m wind speed determination for each of these areas. More detailed attention is given to the northeastern US coastal area because of recent developments including the opening of the first offshore wind farm near Block Island, including providing monthly time series for exceeding key thresholds at five specific nearshore areas.

In this study, we have shown that the HRRR is at least capable of producing physically reasonable estimates of 80-m winds over the US offshore regions. With the continuing expansion of the dataset during subsequent years, and particularly with improving model physics and data assimilation techniques, we expect that the accuracy and statistical significance of our results will continue to increase.

The HRRR 80-m wind dataset is publically available. Additional information on the file formatting, as well as descriptions of the underlying NWP model configuration, is available at the website (http://rapidrefresh.noaa.gov/). The data itself, in GRIB2 format, is available via the Unidata THREDDs Data Server (TDS) interface (http://www.unidata.ucar.edu/software/thredds/current/tds/) at the following URL: (http://esrl.noaa.gov/gsd/thredds/catalog/data/retro/catalog.html).

Acknowledgments

Funding for this study was provided by the U.S. Department of Energy, Wind and Water Program, Award No. DE-EE0003080 and the NOAA Atmospheric Science for Renewable Energy Program. Observations within the POWER project were supported through the NEAQS-04 campaign and the NEHRTP. Comments from two anonymous reviewers greatly improved an earlier version of the manuscript.

References

[1] European Wind Energy Association. The European Offshore Wind Industry: Key trends and statistics 1st half of 2015. European Wind Energy Report (accessed online 25 Mar 2016) http://www.ewea.org/fileadmin/files/library/publications/statistics/EWEA-European-Offshore-Statistics-H1-2015.pdf

[2] Musial W, Ram B. Large-scale offshore wind power in the United States: Assessment of opportunities and barriers. NREL Report TP-500-40745 2010; National Renewable Energy Laboratory, Golden, CO.

[3] Schwartz M, Heimiller D, Haymes S, Musial W. Assessment of offshore wind energy resources for the United States. NREL Report TP-500-45889 2010; National Renewable Energy Laboratory, Golden, CO.

[4] Musial W, Heimiller D, Beiter P, Scott G, Draxl C. 2016 Offshore wind energy resource assessment for the United States. NREL Report TP-5000-66599 2016; National Renewable Energy Laboratory, Golden, CO.

[5] U. S. Department of Energy. A national offshore wind strategy: Creating an offshore wind energy industry in the United States. DOE Report EE-0798 2011.

[6] U. S. Department of Energy. Wind vision: A new era for wind power in the United States. DOE Report GO-102015-4557 2015.

[7] Archer CL, Colle BA, Delle Monache L, Dvorak MJ, Lundquist J, Bailey BH, Beaucage P, Churchfield MJ, Fitch AC, Kosovic B, Lee S, Moriarty SJ, Simao H, Stevens RJAM, Veron D, Zack J. Meteorology for coastal/offshore wind energy in the United States: Recommendations and research needs for the next 10 years. *Bulletin of the American Meteorological Society* 2014; **94:** 515-519. DOI:10.1175/BAMS-D-13-00108.1

[8] Colle BA, Sienkiewicz MJ, Archer C, Veron D, Veron F, Kempton W, Max JE. Improving the mapping and prediction of offshore wind resources (IMPOWR): Experimental overview and first results. *Bulletin of the American Meteorological Society* 2016; **97:** 1377-1390. DOI:10.1175/BAMS-D-14-00253.1

[9] Banta RM, Pichugina YL, Brewer WA, James EP, Olson JB, Benjamin SG, Carley J, Bianco L, Djalalova I, Wilczak JM, Marquis M, Cline J. Evaluating and improving NWP forecast models: How the needs of offshore wind energy can point the way. Manuscript to be submitted to *Bulletin of the American Meteorological Society.*

[10] Pichugina YL, Banta RM, Brewer WA, Sandberg SP, Hardesty RM. Doppler-lidar-based wind-profile measurement system for offshore wind-energy and other marine-boundary-layer applications. *Journal of Applied Meteorology and Climatology* 2012; **51:** 327-349. DOI:10.1175/JAMC-D-11-040.1

[11] Banta RM, Pichugina YL, Kelley ND, Hardesty RM, Brewer WA. Wind energy meteorology: Insight into wind properties in the turbine-rotor layer of the atmosphere from high-resolution Doppler lidar. *Bulletin of the American Meteorological Society* 2013; **94:** 883-902. DOI:10.1175/BAMS-D-11-00057.1

[12] Pichugina YL, Banta RM, Olson JB, Carley JR, Marquis M, Brewer WA, Wilczak JM, Djalalova IV, Bianco L, James EP, Benjamin SG, Cline J. Assessment of NWP

forecast models in simulating offshore winds through the lower boundary layer by measurements from a ship-based scanning Doppler lidar. *Wind Energy* 2016; **19:** in press.

[13] Manwell JF, Rogers AL, McGowan JB, Bailey BH. An offshore wind resource assessment study for New England. *Renewable Energy* 2002; **27:** 175-187. DOI:10.1016/S0960-1481(01)00183-5.

[14] Carta JA, Velazquez S, Cabrera P. A review of measure-correlate-predict (MCP) methods used to estimate long-term wind characteristics at a target site. *Renewable and Sustainable Energy Reviews* 2013; **27:** 362-400. DOI:10.1016/j.rser.2013.07.004.

[15] Woods BK, Nehrkorn T, Henderson JM. A downscaled wind climatology on the outer continental shelf. *Journal of Applied Meteorology and Climatology* 2013; **52:** 1878-1890. DOI:10.1175/JAMC-D-12-0216.1.

[16] Monaldo FM, Li X, Pichel WG, Jackson CR. Ocean wind speed climatology from spaceborne SAR imagery. *Bulletin of the American Meteorological Society* 2014; **95:** 565-569.

[17] Draxl C, Clifton A, Hodge B, McCaa J. The Wind Integration National Dataset (WIND) Toolkit. *Applied Energy* 2015; **151:** 355-366.

[18] Alexander CR, Manikin G, Benjamin S, Weygandt SS, DiMego G, Hu M, Smirnova TG. The High-Resolution Rapid Refresh (HRRR): The operational

implementation, in 95th Annual Meeting of the American Meteorological Society, 2015.

[19] James EP, Benjamin SG. Observation system experiments with the hourly-updating Rapid Refresh model using GSI hybrid ensemble/variational data assimilation. *Monthly Weather Review* 2017; **145:** 2897-2918.

[20] Benjamin SG, Weygandt SS, Brown JM, Hu M, Alexander CR, Smirnova TG, Olson JB, James EP, Dowell DC, Grell GA, Lin H, Peckham SE, Smith TL, Moninger WR, Kenyon JS, Manikin GS. A North American hourly assimilation and model forecast cycle: The Rapid Refresh. *Monthly Weather Review* 2016; **144:** 1669-1694. DOI:10.1175/MWR-D-15-0242.1

[21] Benjamin SG, Devenyi DD, Weygandt SS, Brundage KJ, Brown JM, Grell GA, Kim D, Schwartz BE, Smirnova TB, Smith TL, Manikin GS. An hourly assimilation-forecast cycle: The RUC. *Monthly Weather Review* 2004; **132:** 495-518. DOI:10.1175/1520-0493(2004)132<0495:AHACTR>2.0.CO;2

[22] Skamarock WC, Klemp JB, Dudhia J, Gill DO, Barker DM, Duda MG, Huang XY, Wang W, Powers JG. A description of the Advanced Research WRF version 3. NCAR Report TN-475+STR 2008; Boulder, CO.

[23] Kleist DT, Parrish DF, Derber JC, Treadon R, Wu WS, Lord S. Introduction of the GSI into the NCEP global data assimilation system. *Weather and Forecasting* 2009; **24:** 1691-1705. DOI:10.1175/2009WAF22222201.1

[24] Shao H, Derber J, Huang X-Y, Hu M, Newman K, Stark D, Lueken M, Zhou C, Nance L, Kuo Y-H, Brown B. Bridging research to operations transitions: Status and plans of community GSI. *Bulletin of the American Meteorological Society* 2016; **97:** 1427-1440. DOI:10.1175/BAMS-D-13-00245.1

[25] Hu M, Benjamin SG, Ladwig T, Dowell DC, Weygandt SS, Alexander CR, Whitaker JS. GSI 3-dimensional ensemble-variational hybrid data assimilation using a global ensemble for the regional Rapid Refresh model. *Monthly Weather Review* 2017; **145:** accepted.

[26] Peckham SE, Smirnova TG, Benjamin SG, Brown JM, Kenyon JS. Implementation of a digital filter initialization in the WRF model and its application in the Rapid Refresh. *Monthly Weather Review* 2016; **144:** 99-106. DOI:10.1175/MWRF -D-15-0219.1

[27] James EP, Benjamin SG, Marquis M. A unified high-resolution wind and solar dataset from a rapidly updating numerical weather prediction model. *Renewable Energy* 2017; **102;** 390-405.

[28] Nakanishi M. Improvement of the Mellor-Yamada turbulence closure model based on large-eddy simulation data. *Boundary-Layer Meteorology* 2001; **99:** 349-378. DOI:10.1023/A;1018915827400

[29] Nakanishi M, Niino H. An improved Mellor-Yamada level-3 model with condensation physics: Its design and verification. *Boundary-Layer*

Meteorology 2004; **112:** 1-31. DOI:10.1023/B:BOUN.0000120164.04146.98

[30] Nakanishi M, Niino H. Development of an improved turbulence closure model for the atmospheric boundary layer. *Journal of the Meteorological Society of Japan* 2009; **87:** 895-912. DOI:10.2151/JMSJ.87.895

[31] Janjic ZI. The step-mountain eta coordinate model: Further developments of the convection, viscous sublayer, and turbulence closure schemes. *Monthly Weather Review* 1994; **122:** 927-945. DOI:10.1175/1520-0493(1993)122<0927:TSMECM>2.0.CO;2

[32] Coniglio MC, Correia J, Jr, Marsh PT, Kong F. Verification of convection-allowing WRF model forecasts of the planetary boundary layer using sounding observations. *Weather and Forecasting* 2013; **28:** 842-862. DOI:10.1175/WAF-D-12-00103.1

[33] Cohen AE, Cavallo SM, Coniglio MC, Brooks HE. A review of planetary boundary layer parameterization schemes and their sensitivity in simulating southeastern U.S. cold season severe weather environments. *Weather and Forecasting* 2015; **30:** 591-612. DOI:10.1175/WAF-D-14-00105.1

[34] Huang H-Y, Hall A, Teixeira J. Evaluation of the WRF PBL parameterizations for marine boundary layer clouds: Cumulus and stratocumulus. *Monthly Weather Review* 2013; **141:** 2265-2271. DOI:10.1175/MWR-D-12-00292.1

[35] Siuta D, West G, Stull R. WRF hub-height wind forecast sensitivity to PBL

scheme, grid length, and initial condition choice in complex terrain. *Weather and Forecasting* 2017; **32:** 493-509. DOI:10.1175/WAF-D-16-0120.1

[36] Edson JB, Jampana V, Weller RA, Bigorre SP, Plueddemann AJ, Fairall CW, Miller SD, Mahrt L, Vickers D, Hersbach H. On the exchange of momentum over the open ocean. *Journal of Physical Oceanography* 2013; **43:** 1589-1610.

[37] Smirnova TG, Brown JM, Benjamin SG, Kenyon JS. Modifications to the Rapid Update Cycle Land Surface Model (RUC LSM) available in the Weather Research and Forecasting (WRF) model. *Monthly Weather Review* 2016; **144:** 1851-1865. DOI:10.1175/MWR-D-15-0198.1

[38] Thompson G, Rasmussen RM, Manning K. Explicit forecasts of winter precipitation using an improved bulk microphysics scheme. Part I: Description and sensitivity analysis. *Monthly Weather Review* 2004; **132:** 519-542. DOI:10.1175/1520-0493(2004)132<0519:EFOWPU>2.0.CO;2

[39] Thompson G, Field PR, Rasmussen RM, Hall WD. Explicit forecasts of winter precipitation using an improved bulk microphysics scheme. Part II: Implementation of a new snow parameterization. *Monthly Weather Review* 2008; **136:** 5095-5115. DOI:10.1175/2008MWR2387.1

[40] Thompson G, Eidhammer T. A study of aerosol impacts on clouds and precipitation development in a large winter cyclone. *Journal of the Atmospheric Sciences* 2014; **71:** 3636-3658. DOI:10.1175/JAS-D-13-0305.1

[41] Iacono MJ, Delamere JS, Mlawer EJ, Shephard MW, Clough SA, Clough WD. Radiative forcing by long-lived greenhouse gases: Calculations with the AER radiative transfer models. *Journal of Geophysical Research* 2009; **113:** D13103. DOI:10.1029/2008JD009944

[42] Dudhia J. Numerical study of convection observed during the Winter Monsoon Experiment using a mesoscale two-dimensional model. *Journal of the Atmospheric Sciences* 1989; **46:** 3077-3107. DOI:10.1176/1520-0469(1989)046<3077NSOCOD>2.0.CO;2

[43] Mlawer EJ, Taubman SJ, Brown PD, Iacono MJ, Clough SA. Radiative transfer for inhomogeneous atmospheres: RRTM, a validated correlated-k model for the longwave. *Journal of Geophysical Research* 1997; **102:** 16663-16682. DOI:10.1029/97JD00237

[44] Chou MD, Suarez MJ. An efficient thermal infrared radiation parameterization for use in general circulation models. NASA Report TM-1999-104606 1994; Goddard Space Flight Center, Greenbelt, MD.

[45] Tennekes H. The logarithmic wind profile. *Journal of the Atmospheric Sciences* 1973; **30:** 234-238.

[46] World Meteorological Organization. Guide to Meteorological Instruments and Methods of Observation. WMO-No. 8 p. I.5-12.

[47] Fairall CW, Bradley EF, Hare JE, Grachev AA, Edson EE. Bulk parameterization

of air-sea fluxes: Updates and verification for the COARE algorithm. *Journal of Climate* 2003; **16:** 571-591.

[48] Clack CTM, Alexander A, Choukulkar A, MacDonald AE. Demonstrating the effect of vertical and directional shear for resource mapping of wind power. *Wind Energy* 2016; **19:** 1687-1697. DOI:10.1002/we.1944

[49] U. S. Department of Energy. Offshore wind market and economic analysis. DOE Report DE-EE0005360 2013.

[50] Parish TR, Rahn DA, Leon DC. Aircraft measurements and numerical simulations of an expansion fan off the California coast. *Journal of Applied Meteorology and Climatology* 2016; **55:** 2053-2062.

[51] Djalalova IV, Olson J, Carley JR, Bianco L, Wilczak JM, Pichugina Y, Banta R, Marquis M, and Cline C. The POWER Experiment: Impact of assimilation of a network of coastal wind profiling radars on simulating offshore winds in and above the wind turbine layer. *Weather and Forecasting* 2016; **31:** 1071-1091. DOI:10.1175/WAF-D-15-0104.1.

Table 1. Important configuration changes within the 3-km HRRR during the 2013-15 period of study, compared to the configuration of the 2-km WIND Toolkit WRF model [17]. PBL: planetary boundary layer. MYNN: Mellor-Yamada-Nakanishi-

Niino. LSM: land surface model. RRTM: Rapid Radiative Transfer Model. RRTMG: Rapid Radiative Transfer Model – Global.

Component	**3-km High-Resolution Rapid Refresh**	**2-km WIND Toolkit**
WRF-ARW version	1 Jan – 30 Mar 2013: WRFv3.3.1 30 Mar 2013 – 10 Apr 2014: WRFv3.4.1 10 Apr 2014 – 10 Apr 2015: WRFv3.5.1 10 Apr – 31 Dec 2015: WRFv3.6	WRFv3.4.1
Convective scheme/clouds	1 Jan 2013 – 10 Apr 2015: None 10 Apr – 31 Dec 2015: MYNN boundary layer clouds	None
PBL scheme	1 Jan – 4 Apr 2013: Mellor-Yamada-Janjic 4 Apr 2013 – 10 Apr 2014: modified MYNN 10 Apr 2014 – 10 Apr 2015: MYNN with reduced thermal roughness over snow 10 Apr – 31 Dec 2015: further enhanced MYNN	Yonsei Univ. scheme
Wind-wave drag coefficient	1 Jan 2013 – 10 Apr 2015: constant drag with wind speed 10 Apr – 31 Dec 2015: COARE algorithm v3.0	Yonsei Univ. scheme

LSM	1 Jan – 13 Mar 2013: 6-level RUC LSM 13 Mar 2013 – 10 Apr 2014: 9-level RUC LSM 10 Apr 2014 – 10 Apr 2015: RUC LSM with increased resolution of top snow layer 10 Apr – 31 Dec 2015: further enhanced RUC LSM	Noah LSM
Radiation scheme (shortwave)	1 Jan – 30 Mar 2013: Dudhia 30 Mar 2013 – 10 Apr 2014: Goddard (5 min calls) 10 Apr 2014 – 31 Dec 2015: RRTMG (15 min calls but with solar zenith angle interpolation)	Dudhia
Radiation scheme (longwave)	1 Jan 2013 – 10 Apr 2014: RRTM 10 Apr 2014 – 31 Dec 2015: RRTMG	RRTM
Microphysics scheme	1 Jan – 30 Mar 2013: Thompson v3.3.1 30 Mar 2013 – 10 Apr 2014: Thompson v3.4.1 10 Apr 2014 – 4 May 2015: Thompson v3.5.1 4 May – 31 Dec 2015: aerosol-aware Thompson v3.6.1	Eta
Data assimilation	1 Jan – 6 Apr 2013: radar downscaled from RAP	None

(DA) configuration	6 Apr 2013 – 8 Apr 2014: 15-min radar DA + 3DVar with static model background error covariance 8 Apr 2014 – 31 Dec 2015: 15-min radar DA + hybrid ensemble/variational DA with 75% flow-dependent covariance from 80-mem GFS ensemble / 25% static covariance	
Cycling	1 Jan 2013 – 10 Apr 2015: None 10 Apr – 31 Dec 2015: land surface only	None

Table 2. Verification of 1-h HRRR wind speed forecasts for 2013-2015 against buoy observations. A simple log wind speed profile correction was employed to interpolate from 10-m HRRR winds to the anemometer heights (see text). Note that the Great Lake buoys (marked with *) do not report winds when lake ice is present (generally a 4-5 month period each winter/spring).

Buoy	**Lat. (deg. north)**	**Lon. (deg. west)**	**Elev. (m)**	**Anem. Hgt (m)**	**Start (Y/M/D)**	**End (Y/M/D)**	**RMSE (m s^{-1})**	**Bias (m s^{-1})**
41004	32.501	79.099	0	4	14/1/1	15/12/31	1.84	-0.61
41025	35.006	75.402	0	5	13/10/1	15/12/31	2.12	-0.70
42019	27.907	95.352	0	5	13/6/16	15/12/31	1.61	-0.33
42020	26.968	96.694	0	5	13/6/16	15/12/31	1.70	-0.37
44007	43.525	70.141	0	5	13/6/16	15/12/31	1.97	-0.02
44065	40.369	73.703	0	5	13/6/16	15/12/31	1.78	-0.14

45004*	47.585	86.585	183	5	14/5/18	15/12/05	2.94	1.27
45005*	41.677	83.398	174	4	13/6/16	15/12/02	1.85	-0.08
45007*	42.674	87.026	183	5	13/6/16	15/12/05	2.03	0.07
45008*	44.283	82.416	177	5	13/6/16	15/11/16	2.06	0.26
45012*	43.621	77.406	75	5	13/6/16	15/12/23	1.89	0.27
46014	39.235	123.974	0	4	13/6/16	15/7/31	2.01	0.16
46015	42.758	124.850	0	4	13/6/16	15/12/31	1.90	-0.04
BUZM3	41.397	71.033	0	24.8	13/6/16	15/12/31	2.04	-0.43

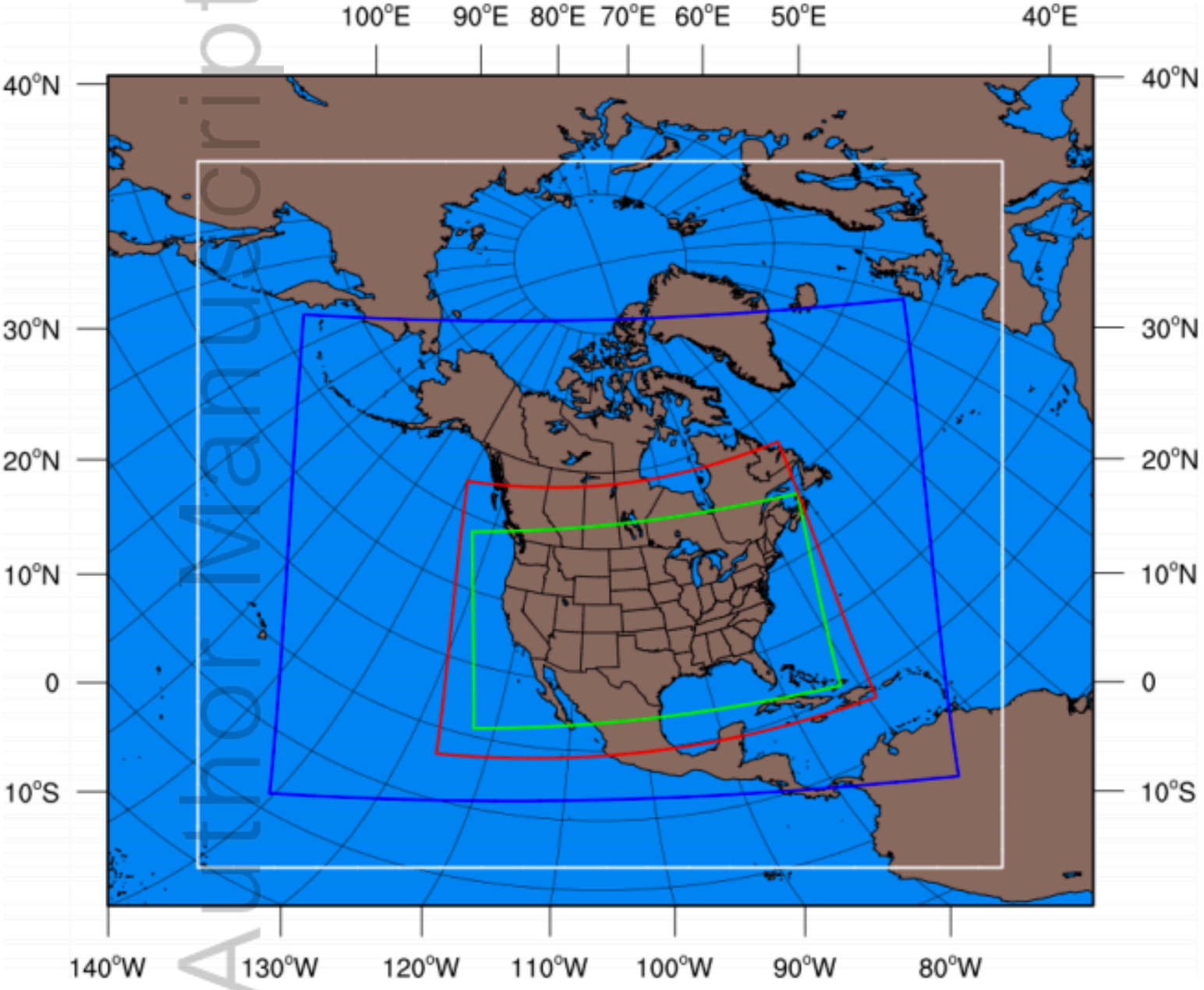

WE_2161_F1.png

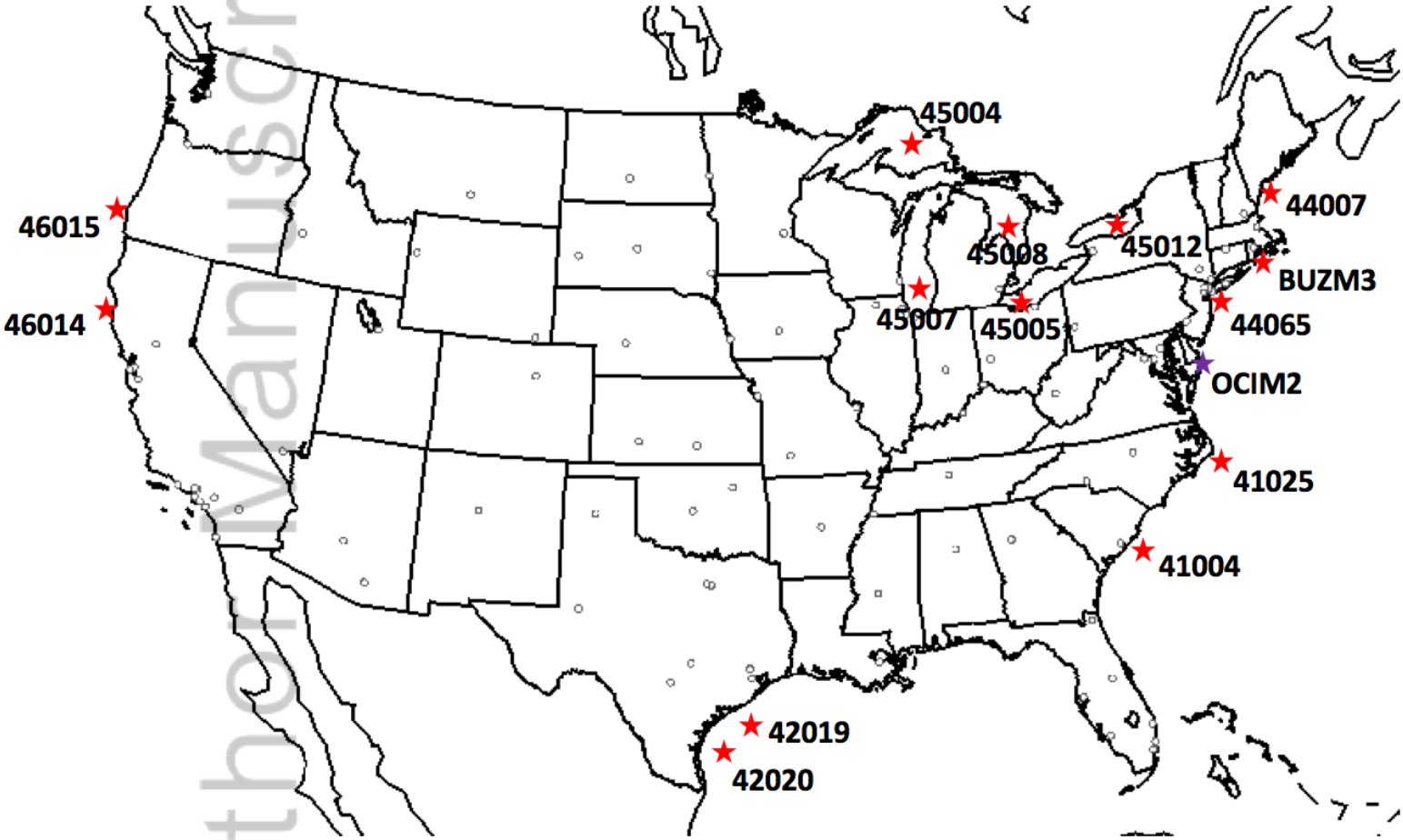

WE_2161_F2.png

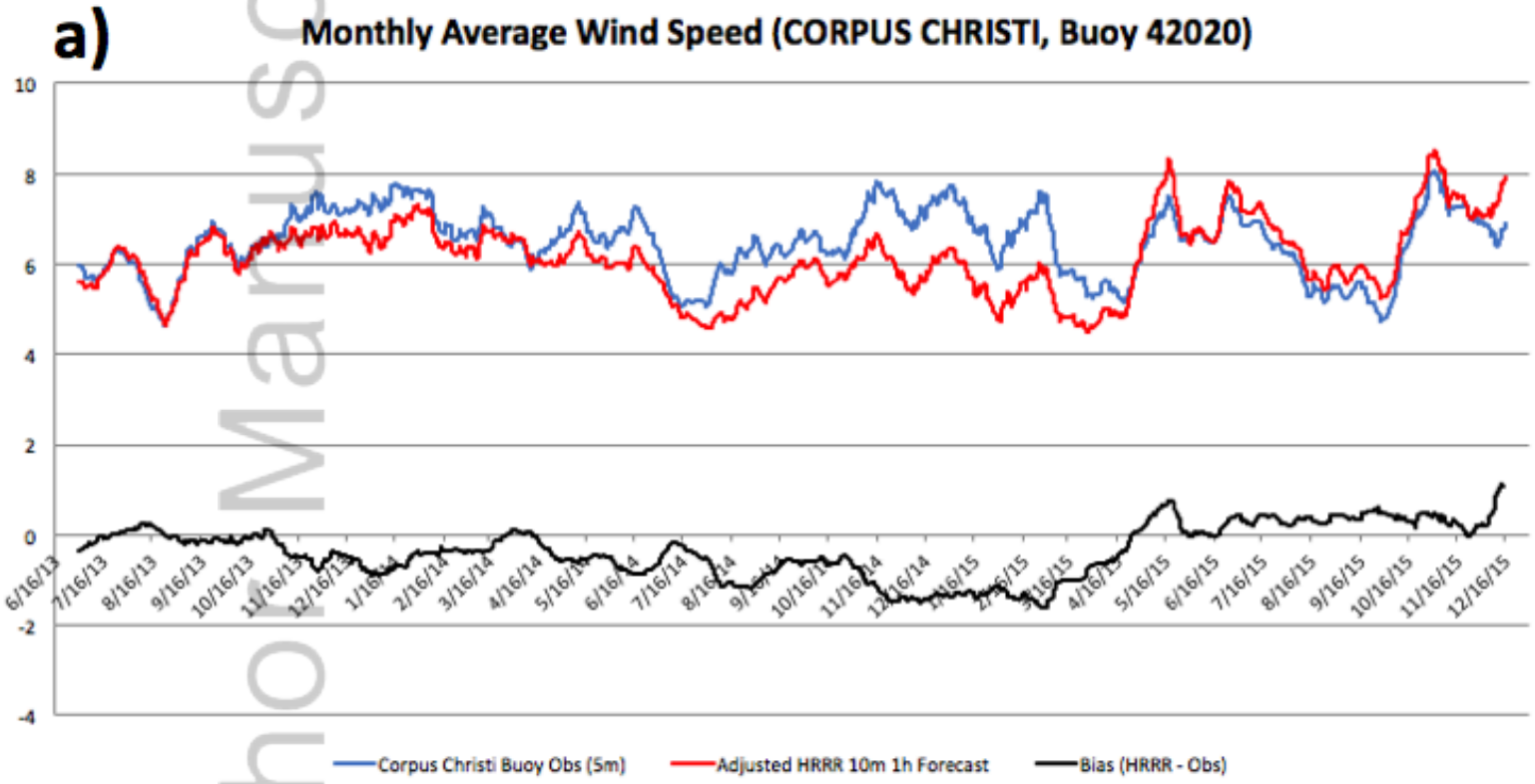

WE_2161_F3a.png

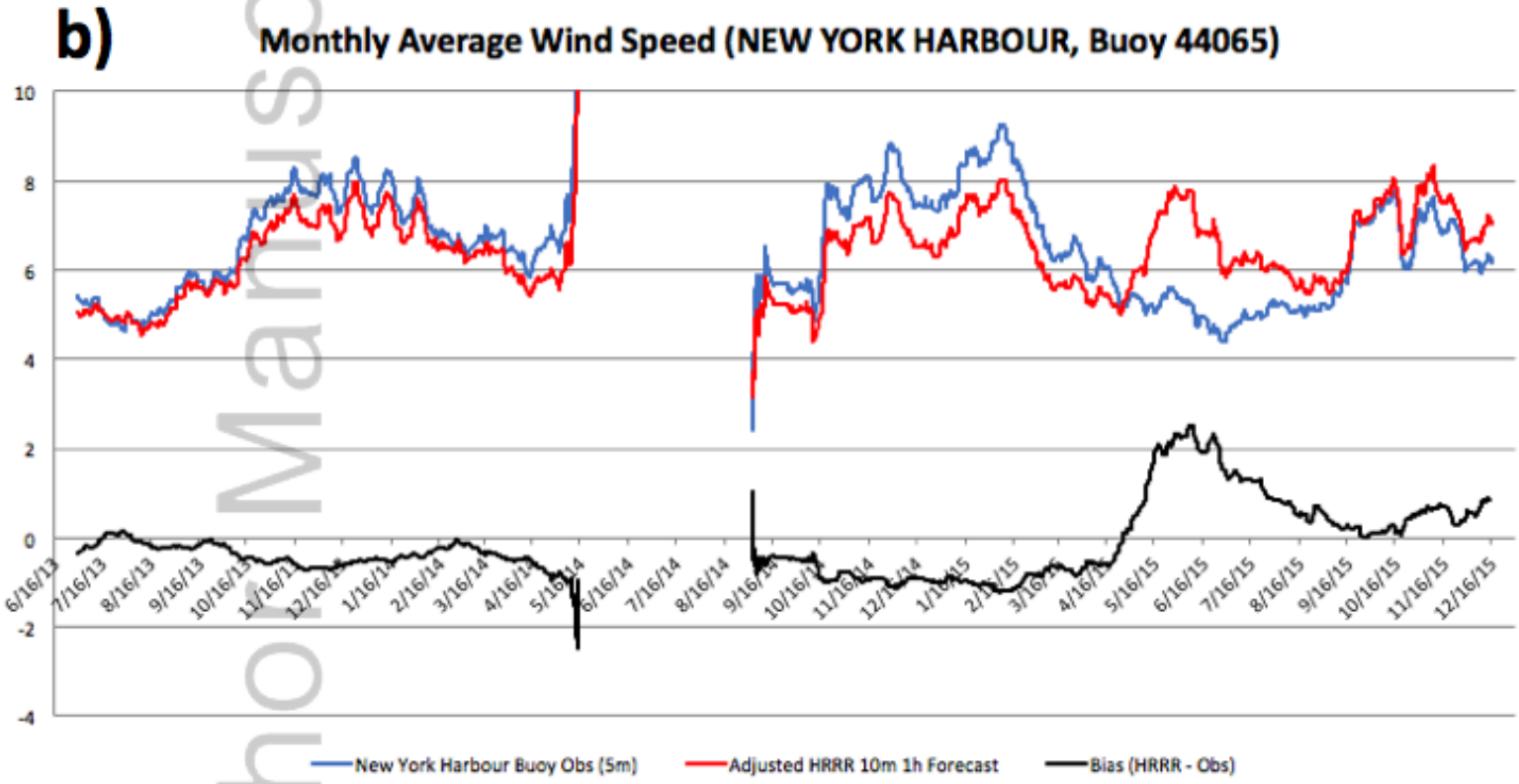

WE_2161_F3b.png

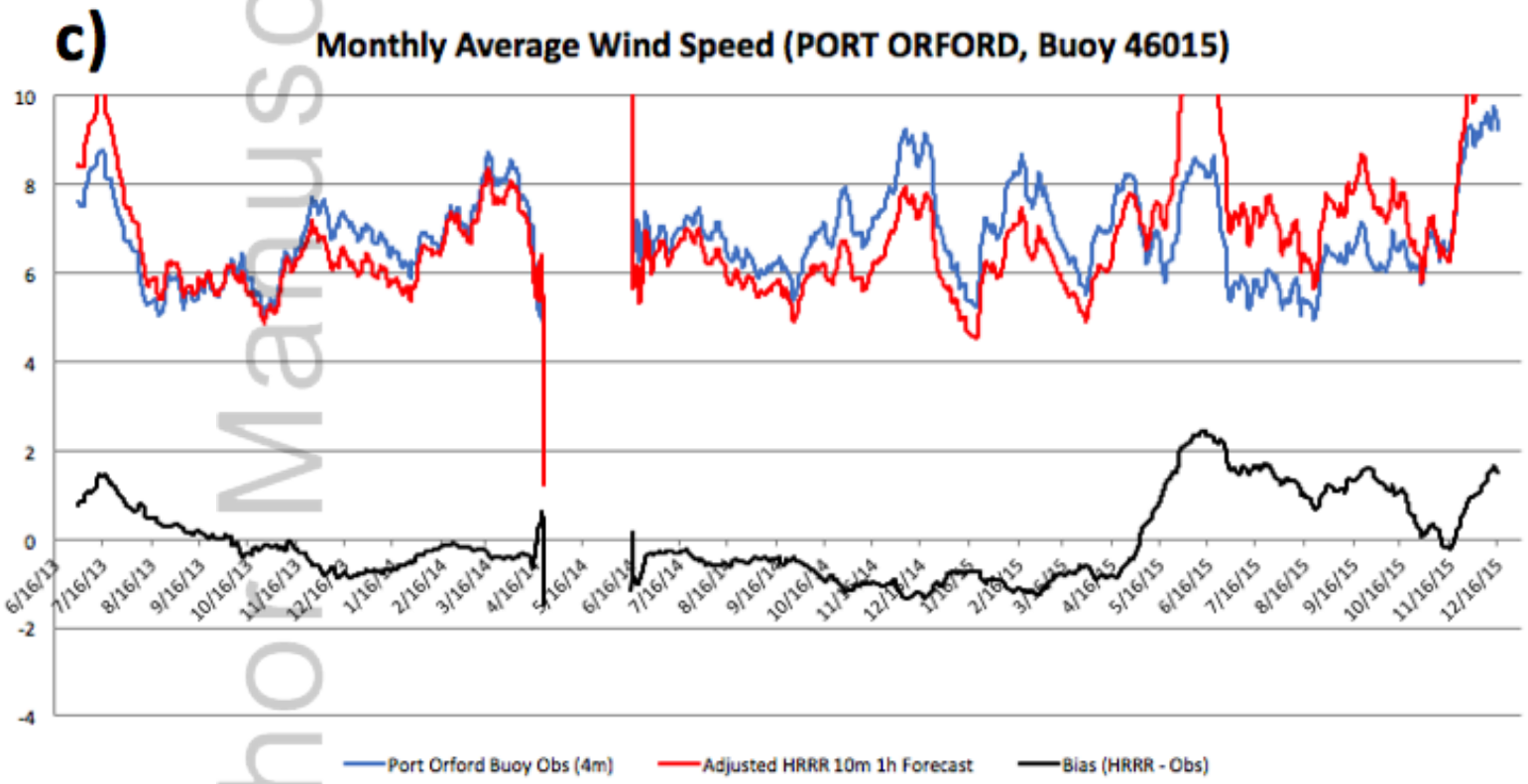

WE_2161_F3c.png

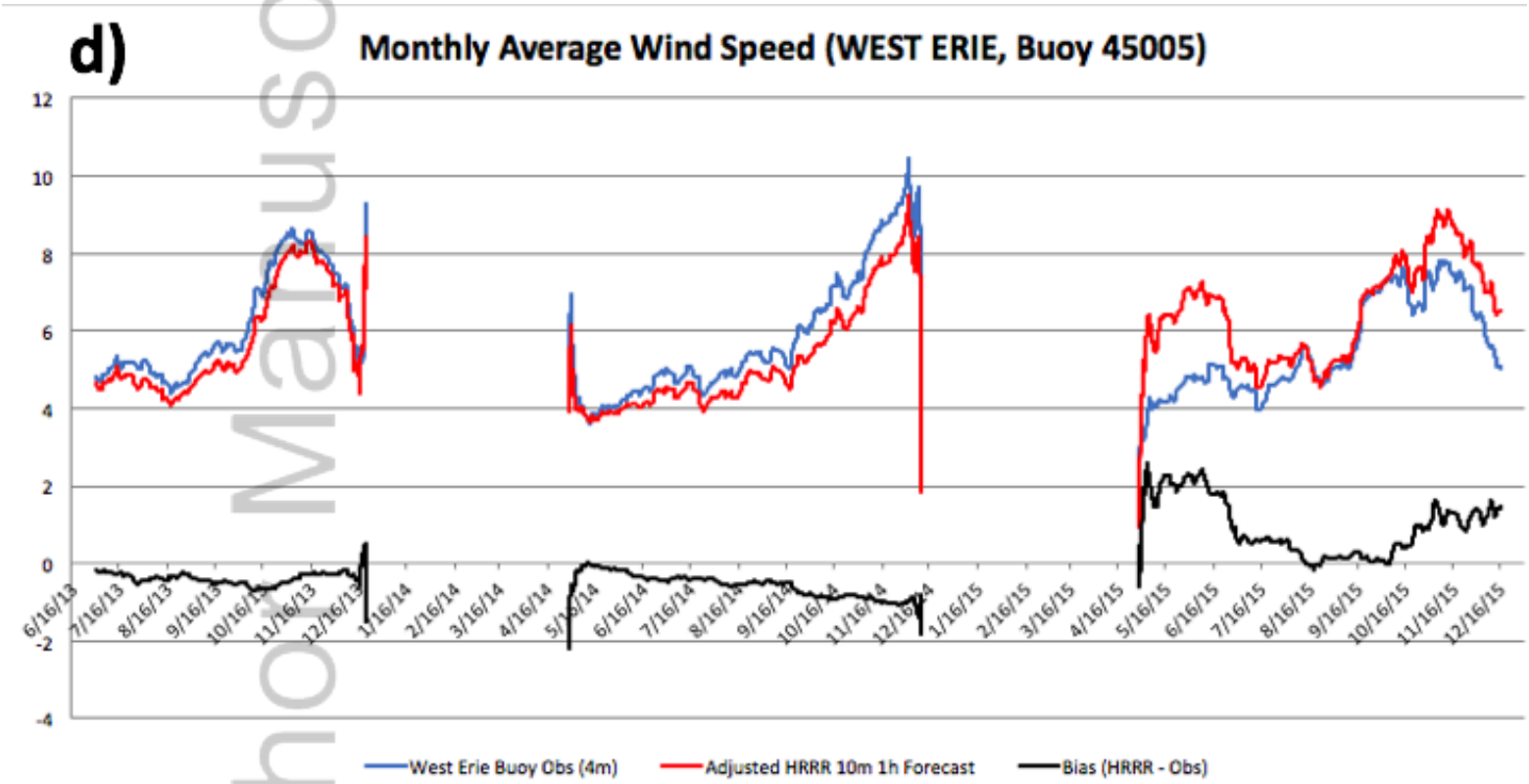

WE_2161_F3d.png

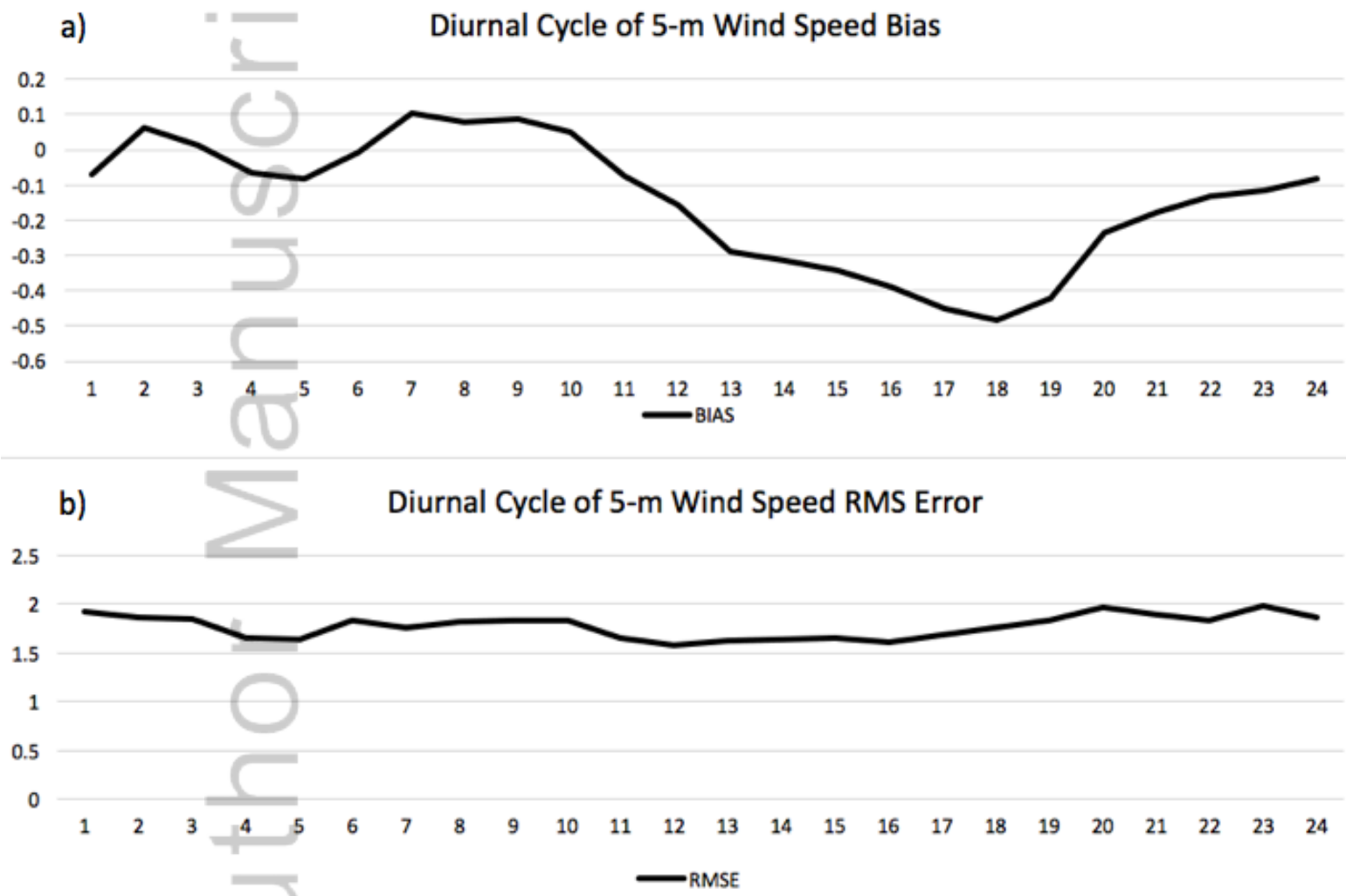

WE_2161_F4.png

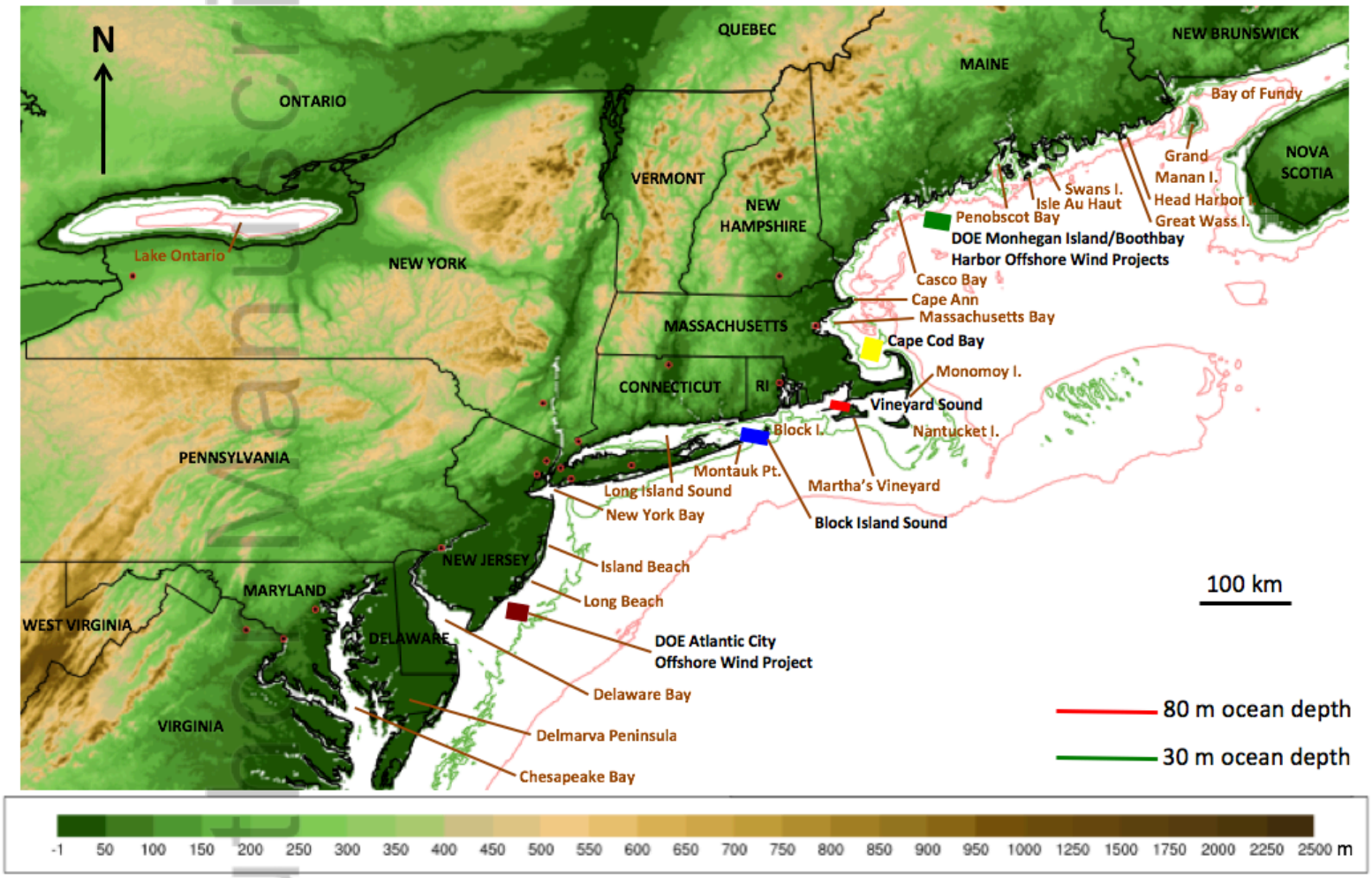

WE_2161_F5.png

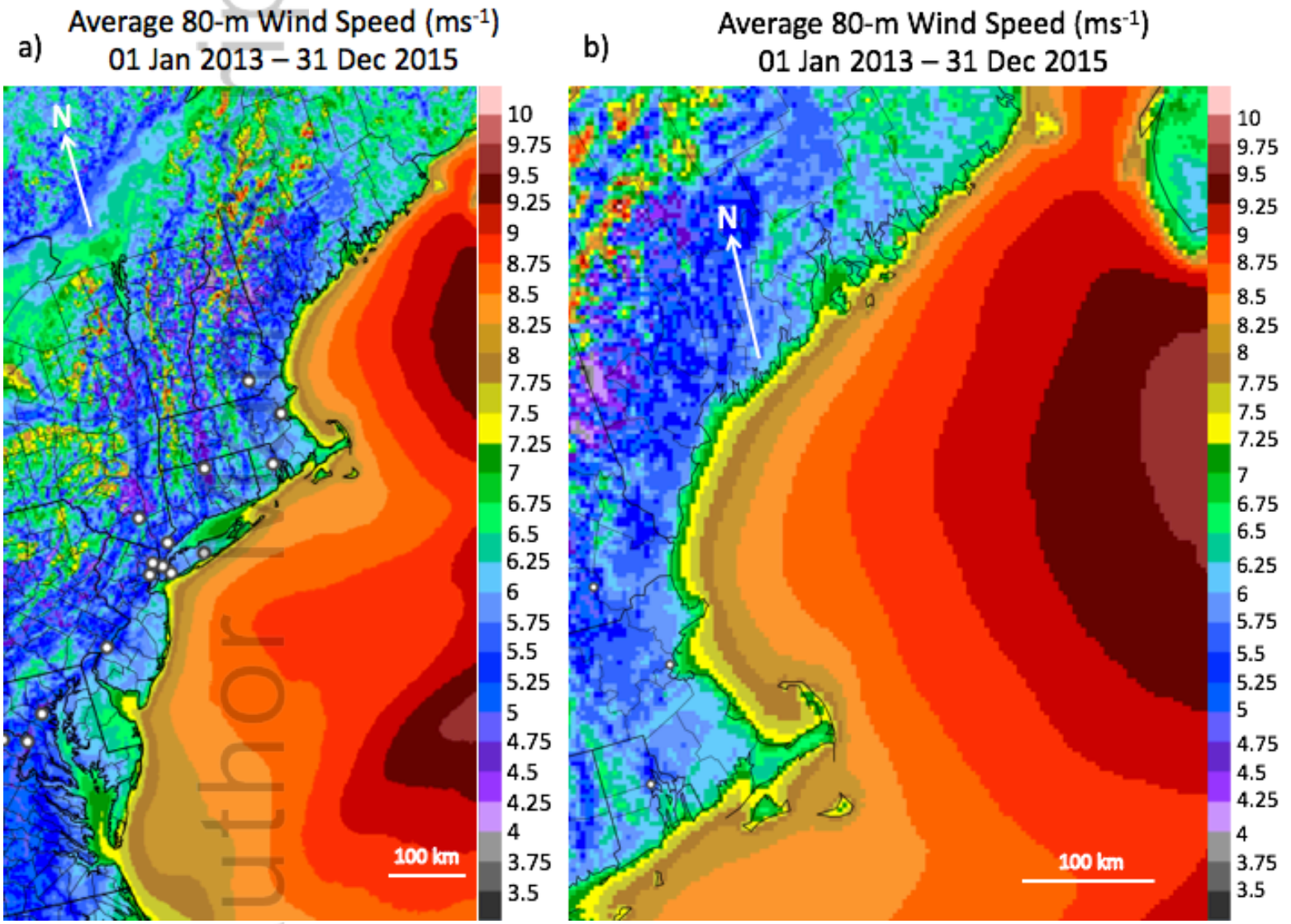

WE_2161_F6.png

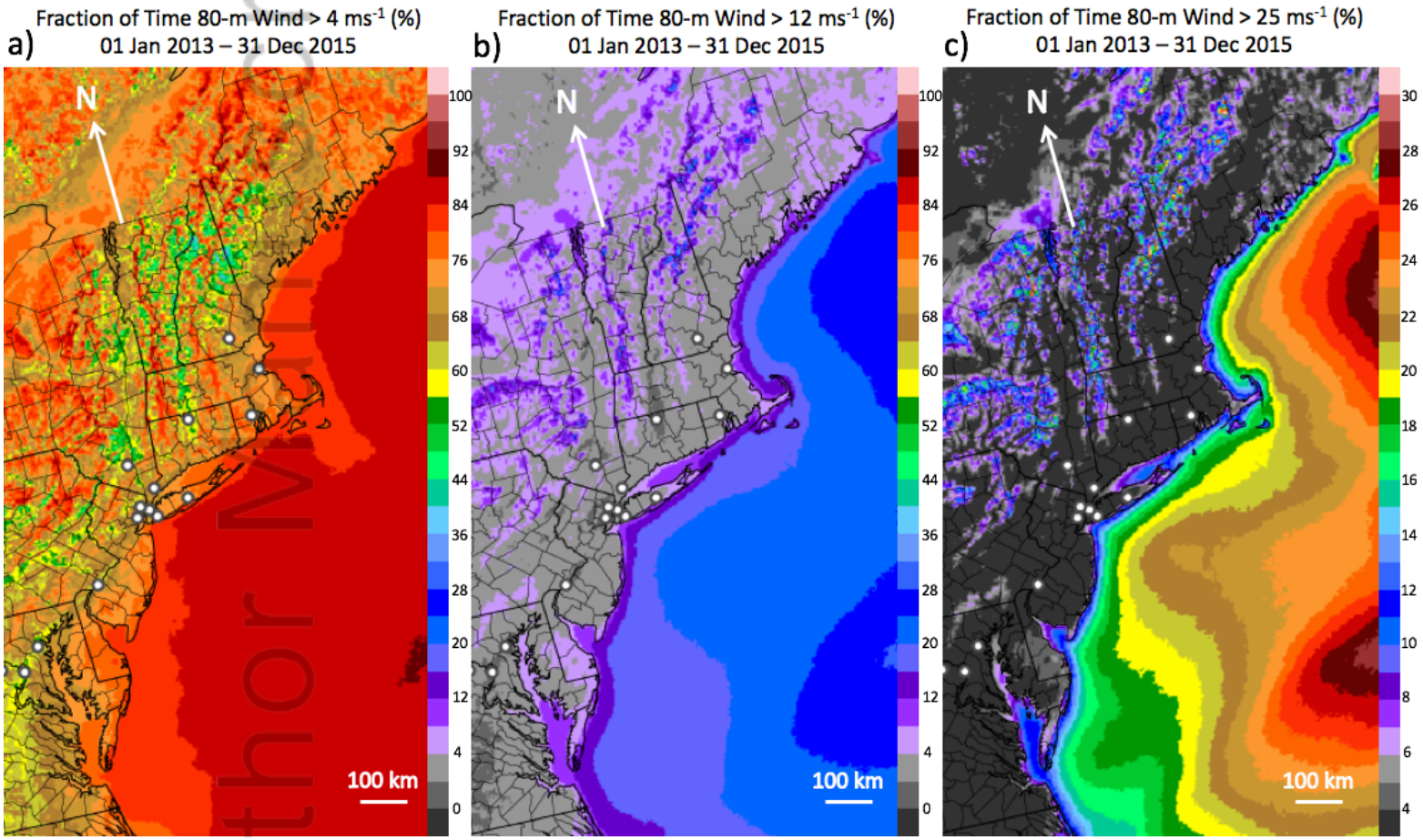

WE_2161_F7.png

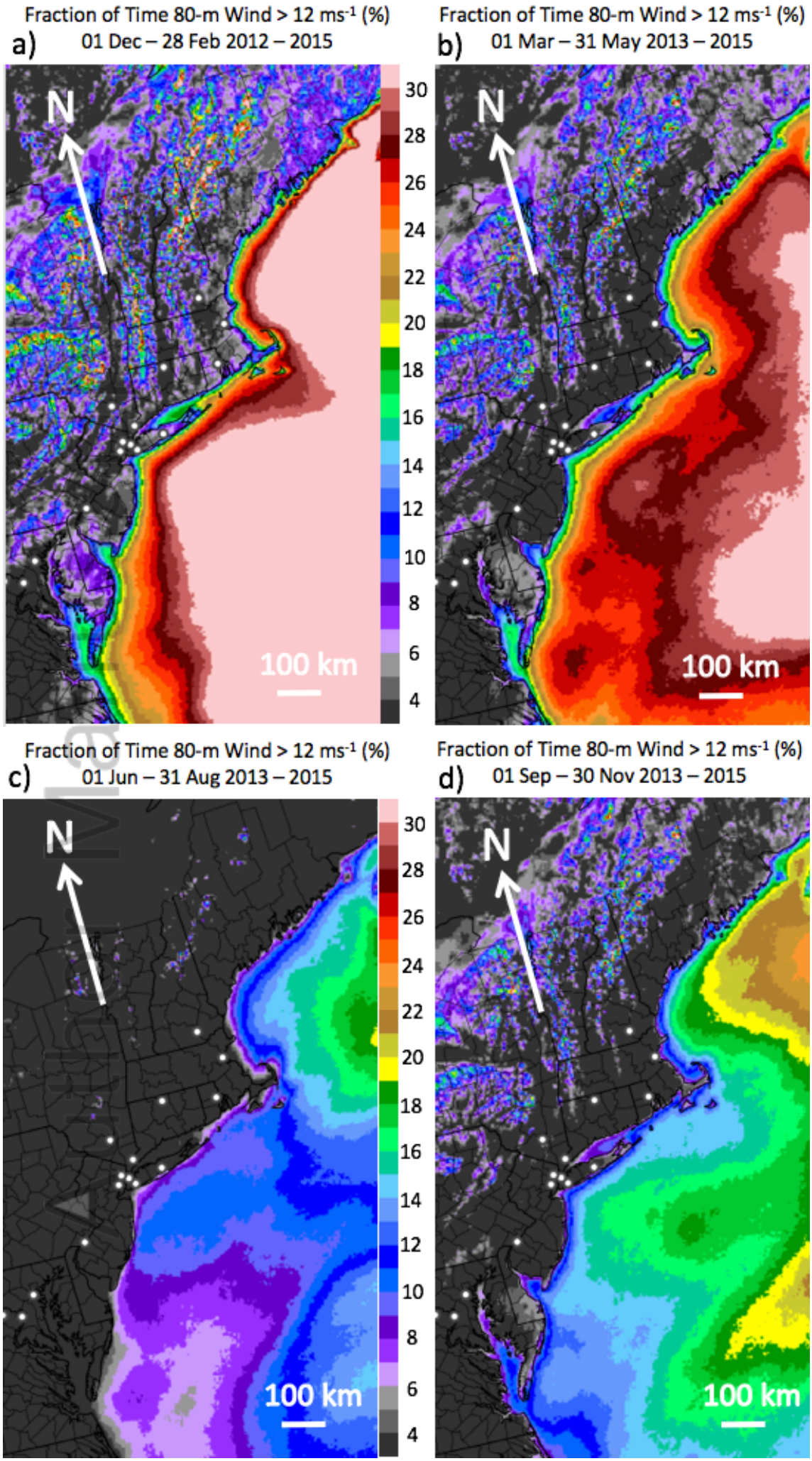

WE_2161_F8.png

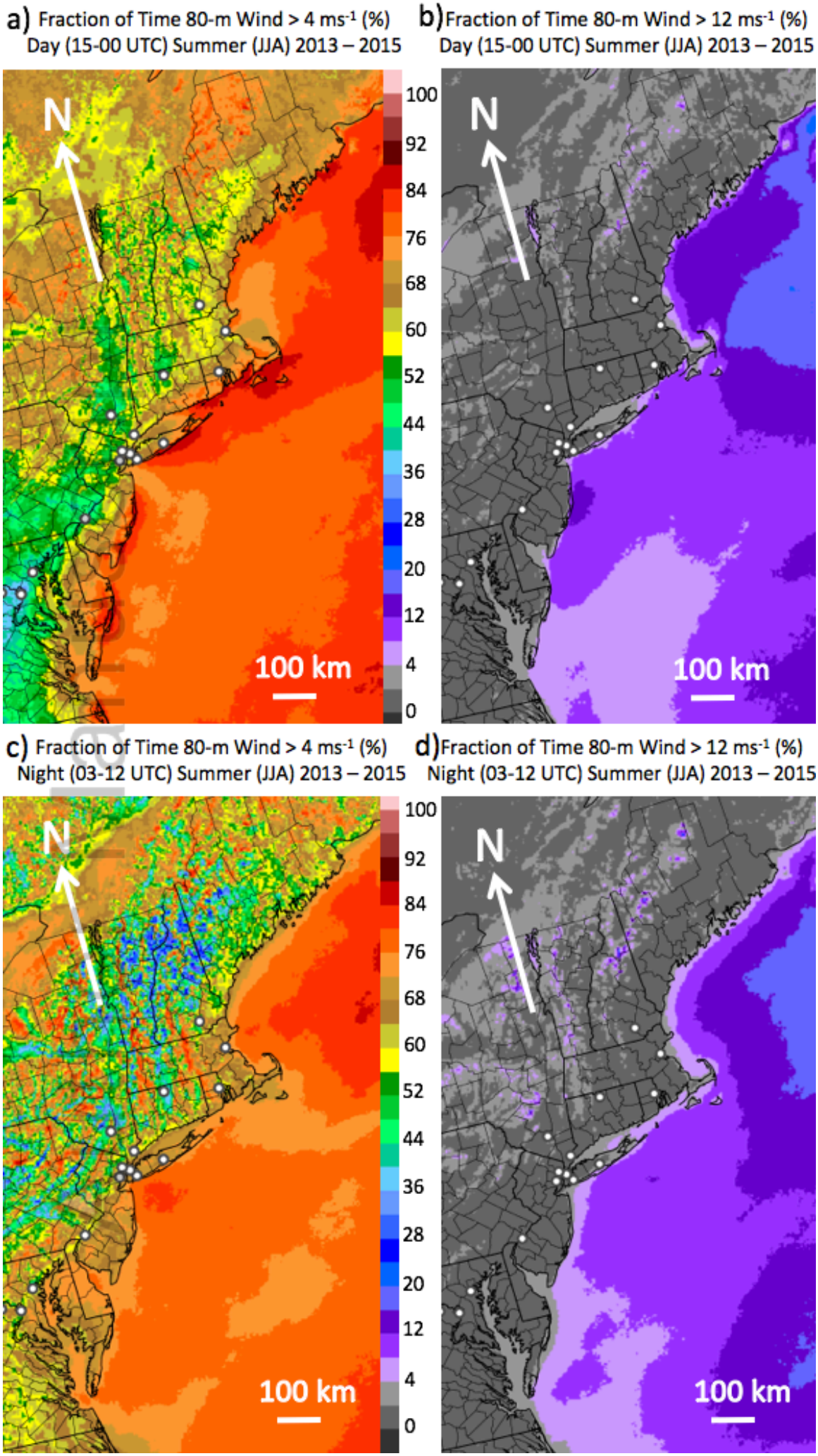

WE_2161_F9.png

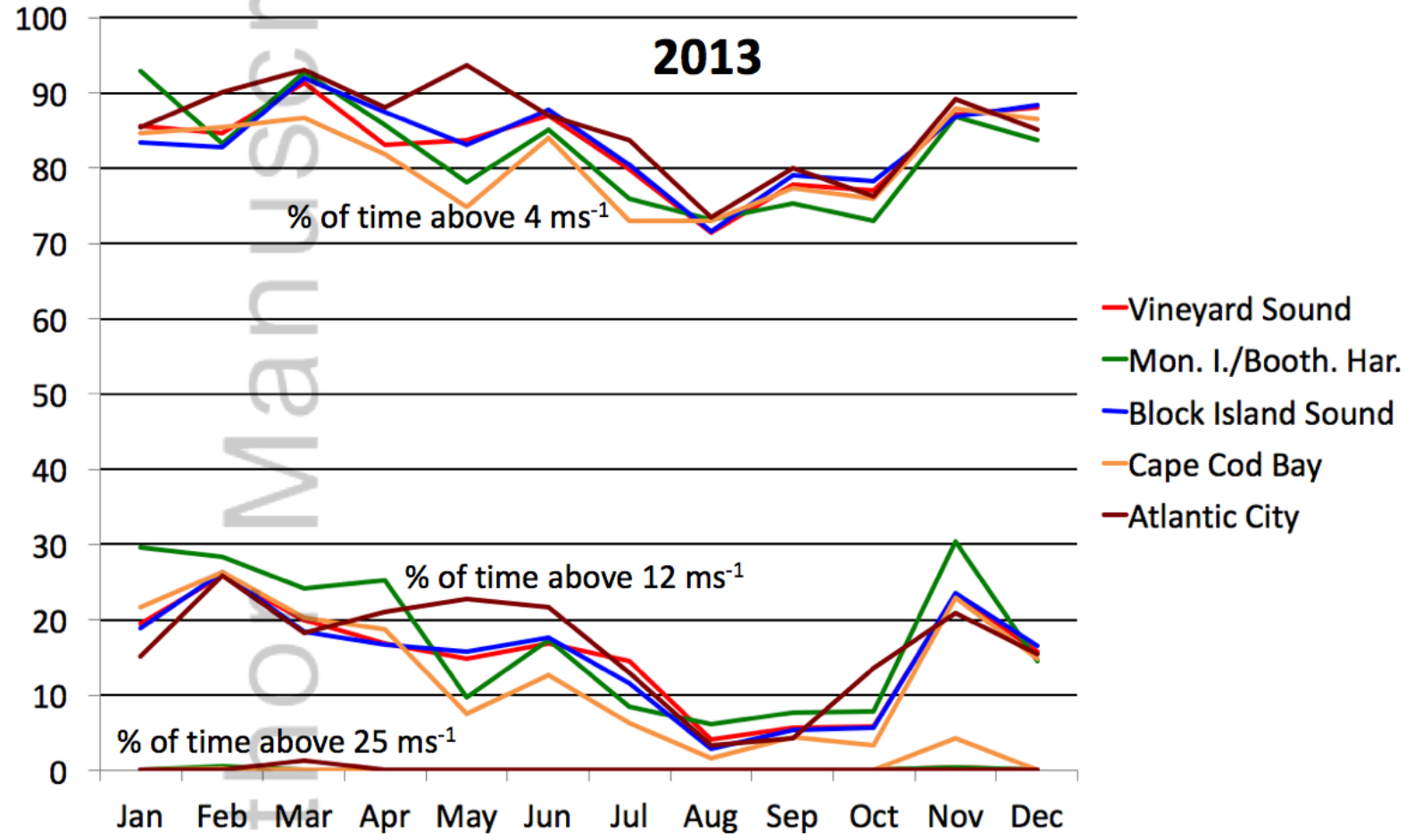

WE_2161_F10a.png

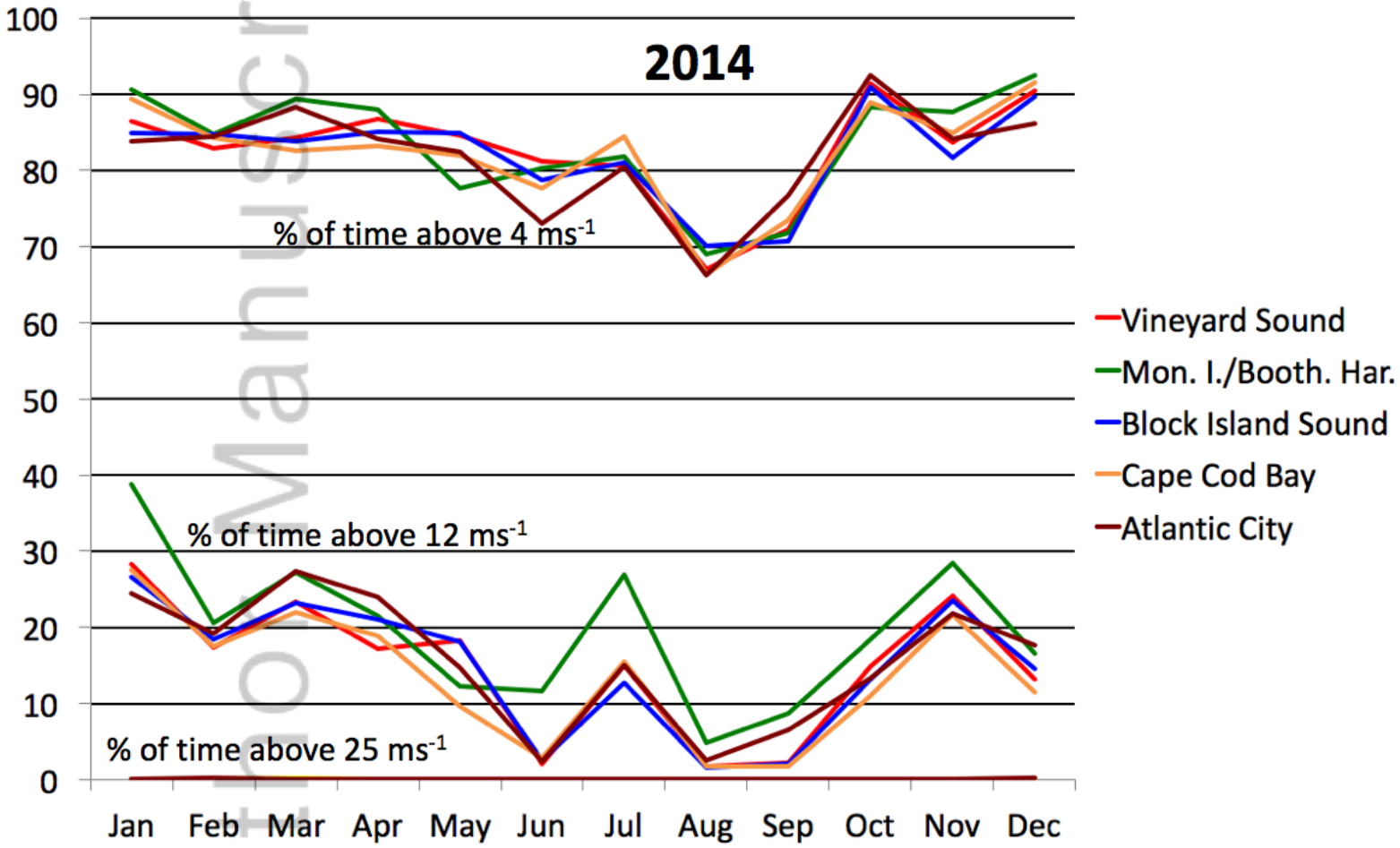

WE_2161_F10b.png

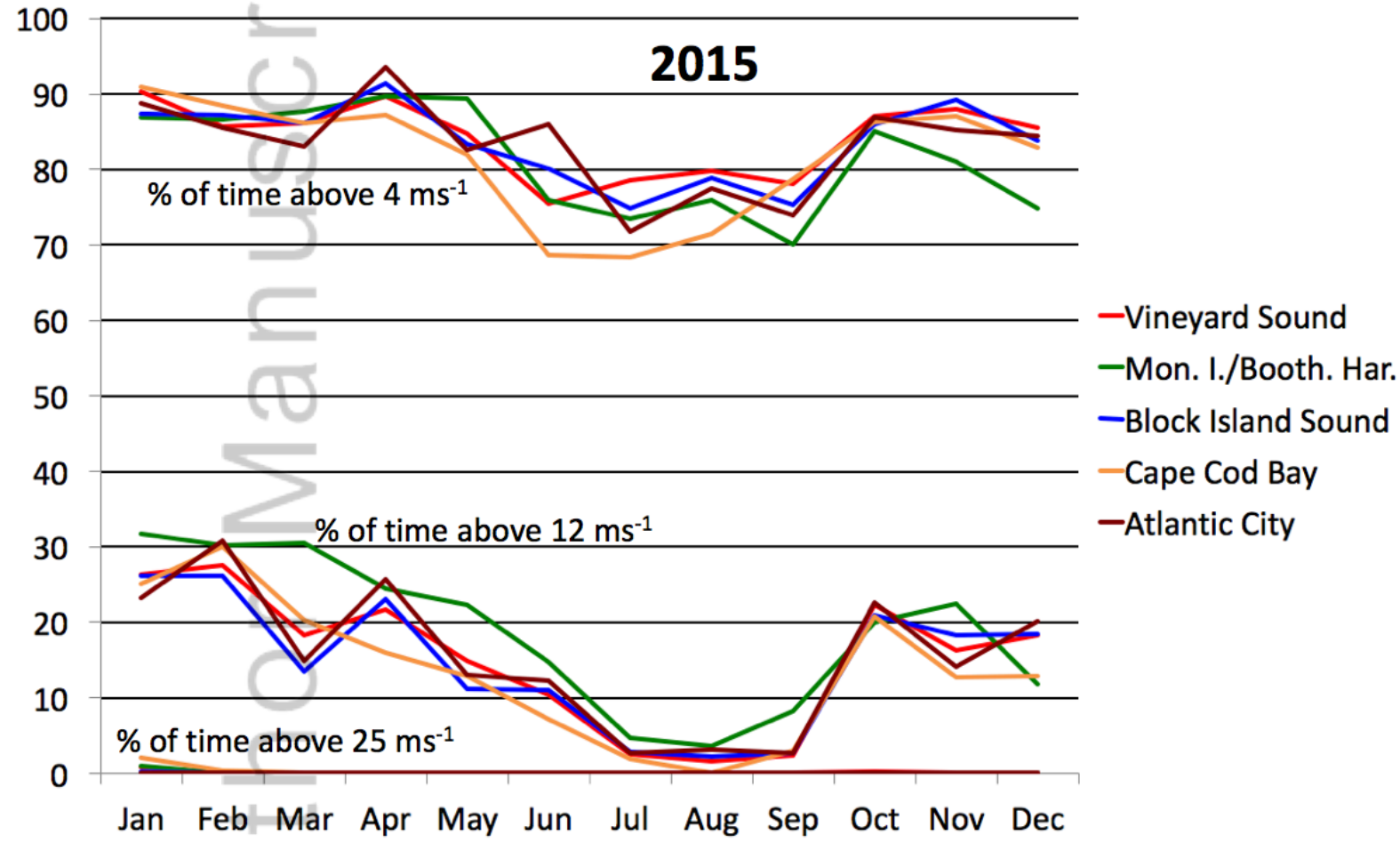

WE_2161_F10c.png

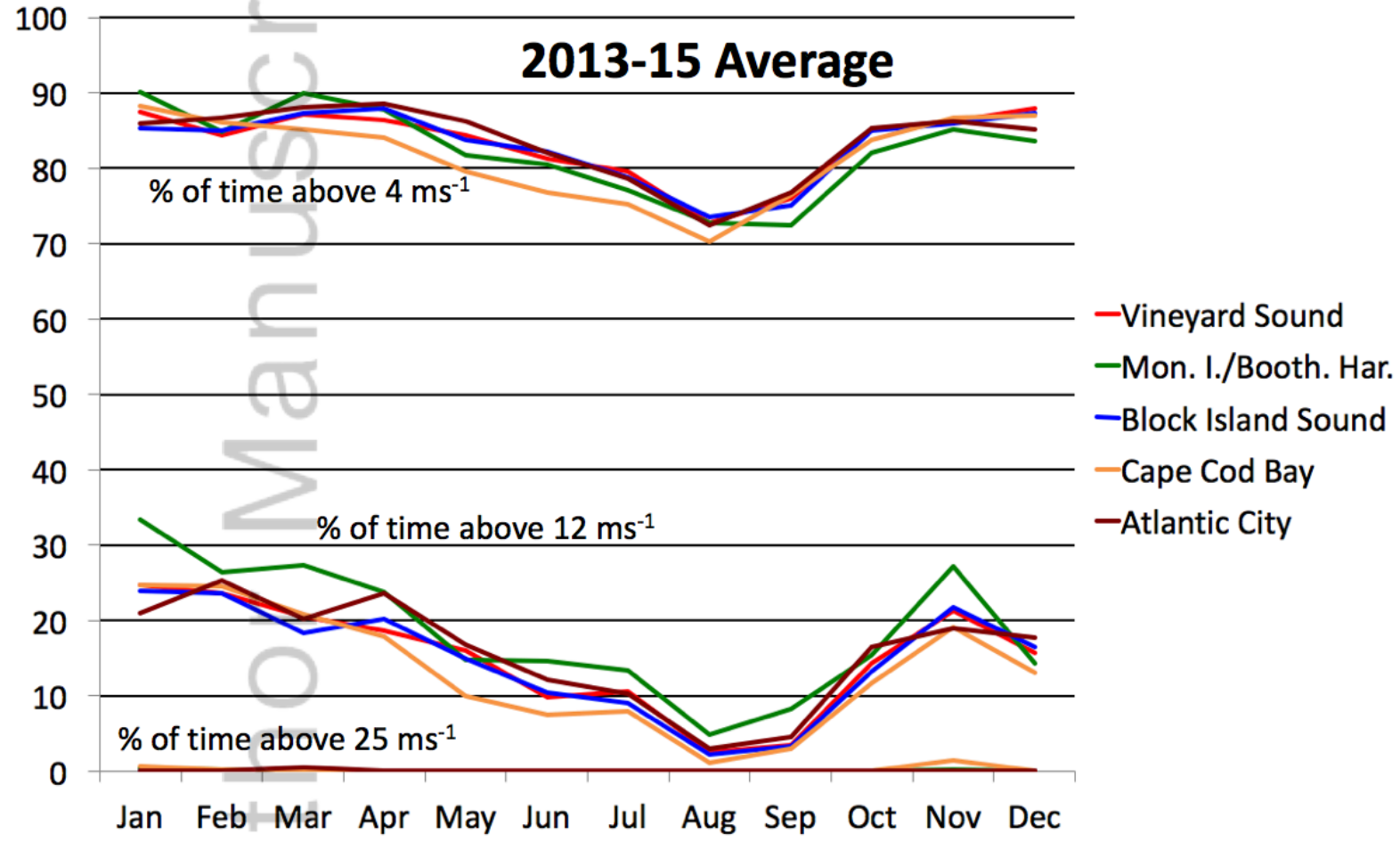

WE_2161_F11.png

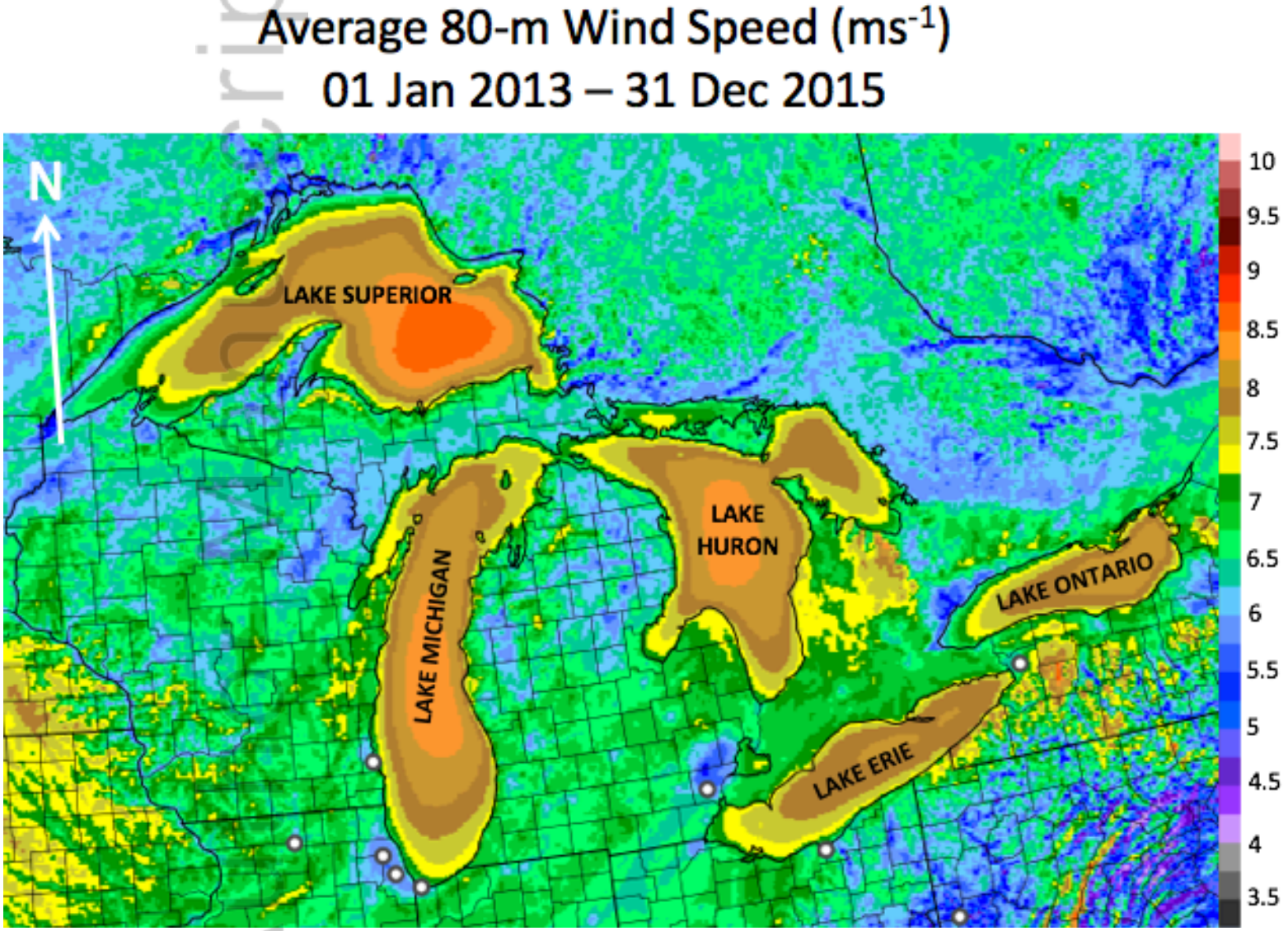

WE_2161_F12.png

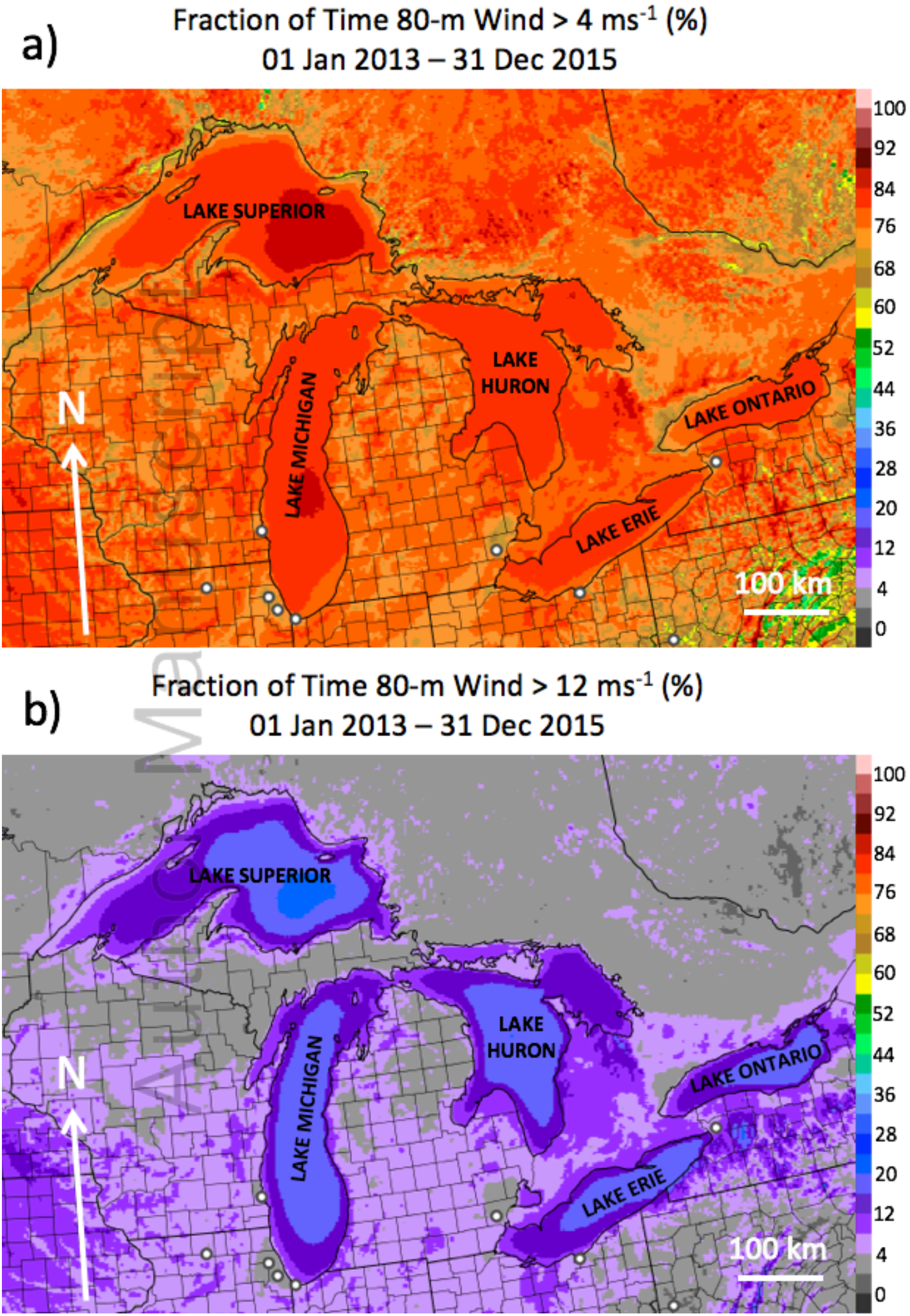

WE_2161_F13.png

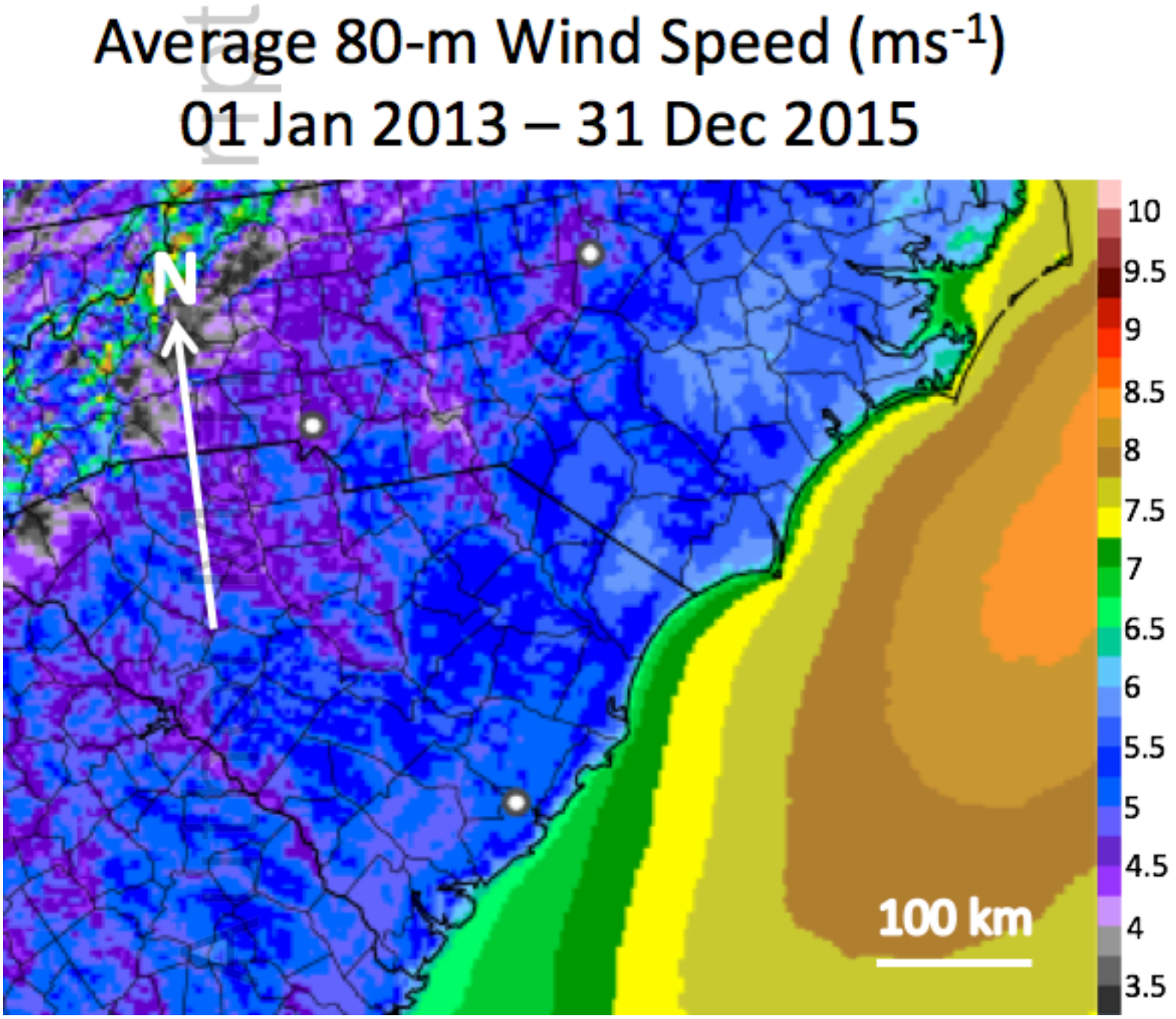

WE_2161_F14.png

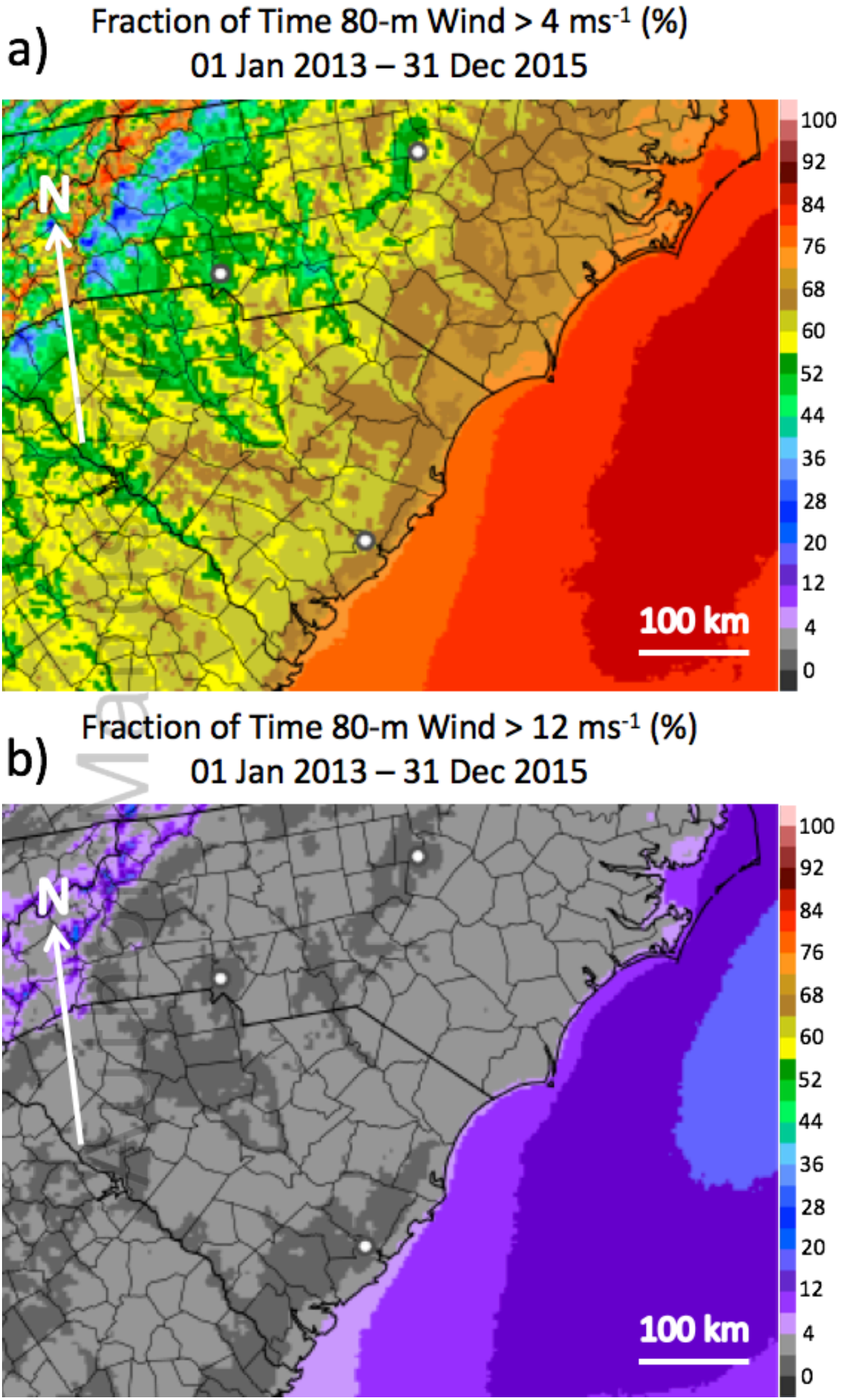

WE_2161_F15.png

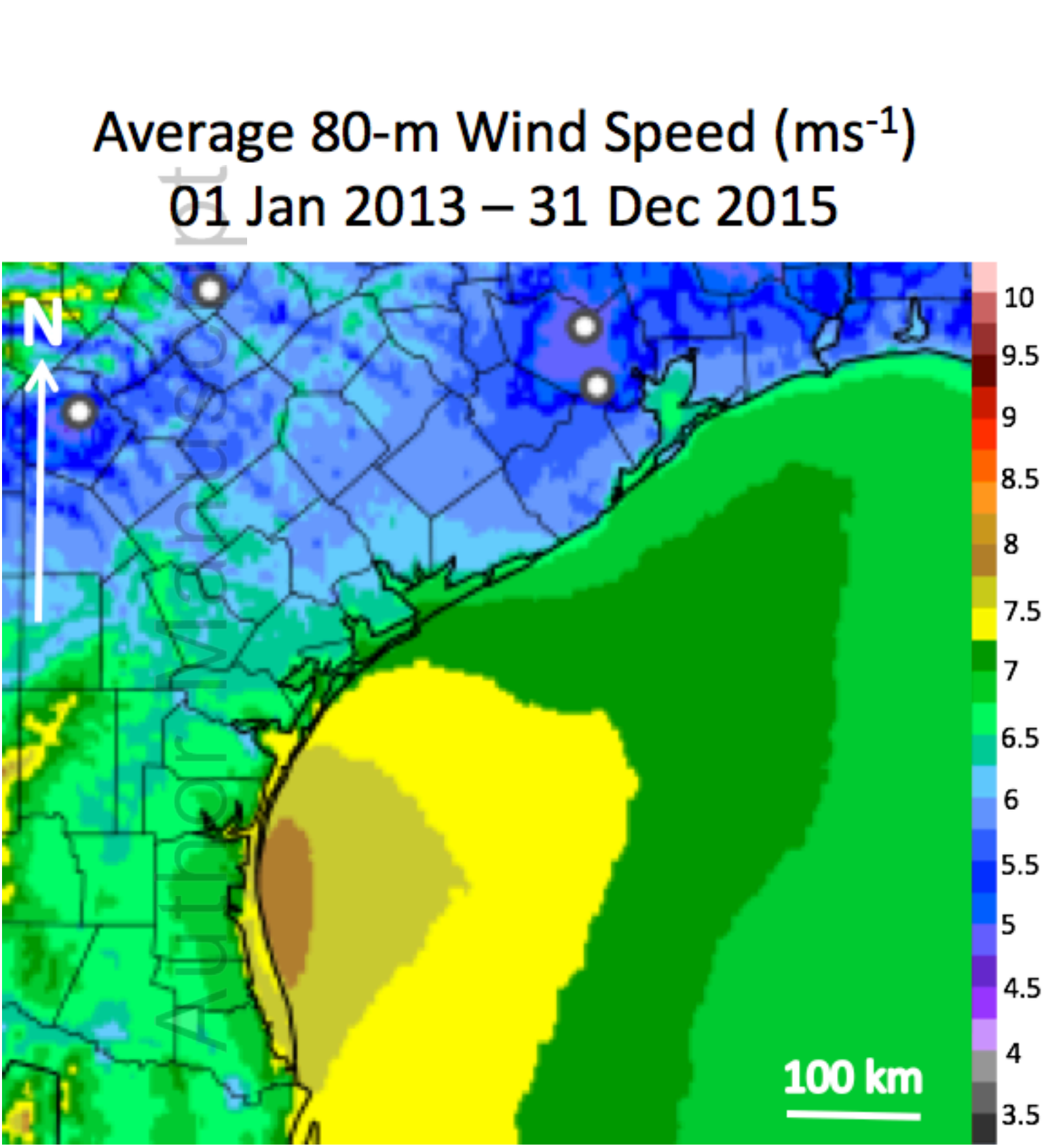

WE_2161_F16.png

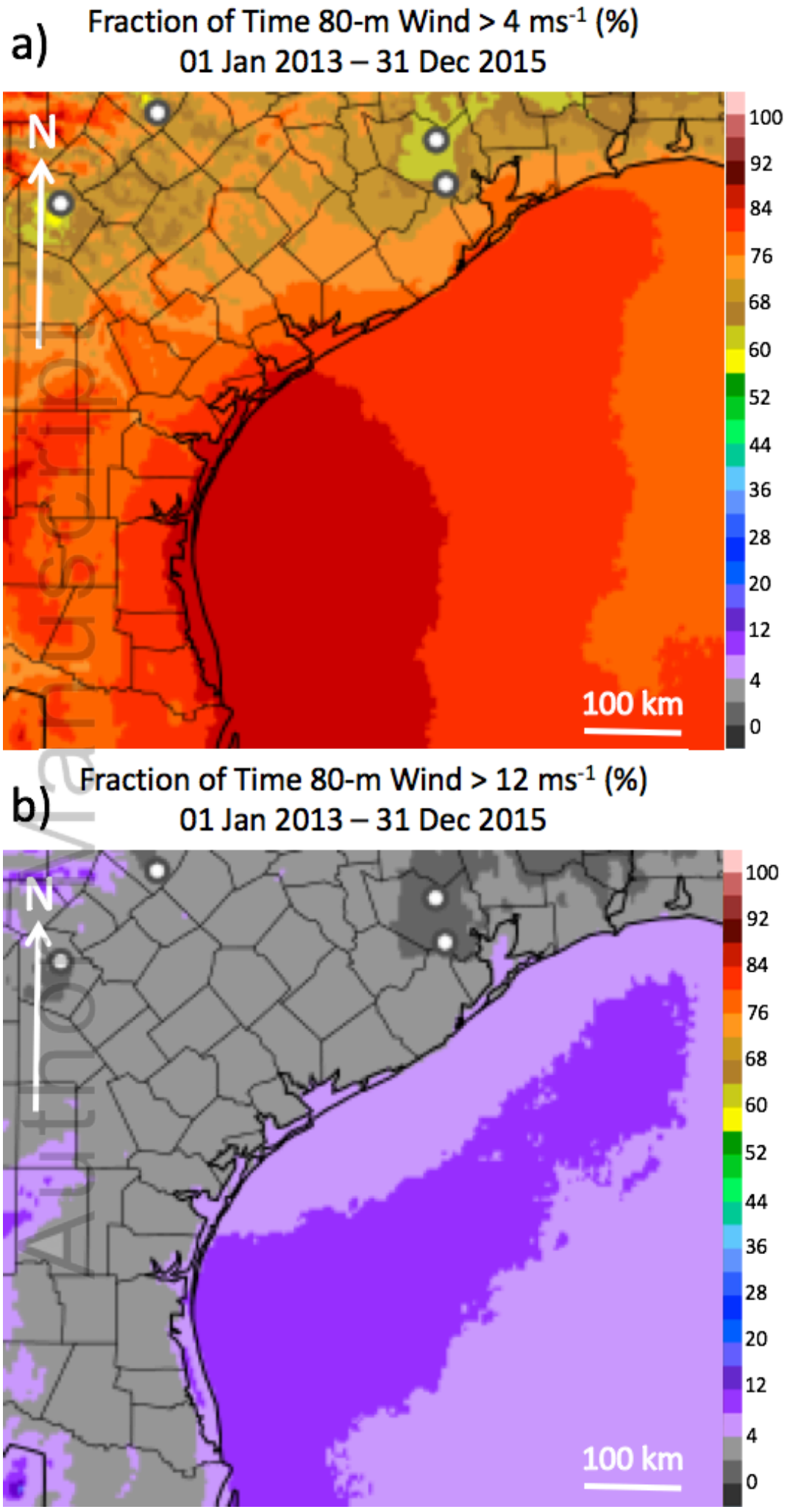

WE_2161_F17.png

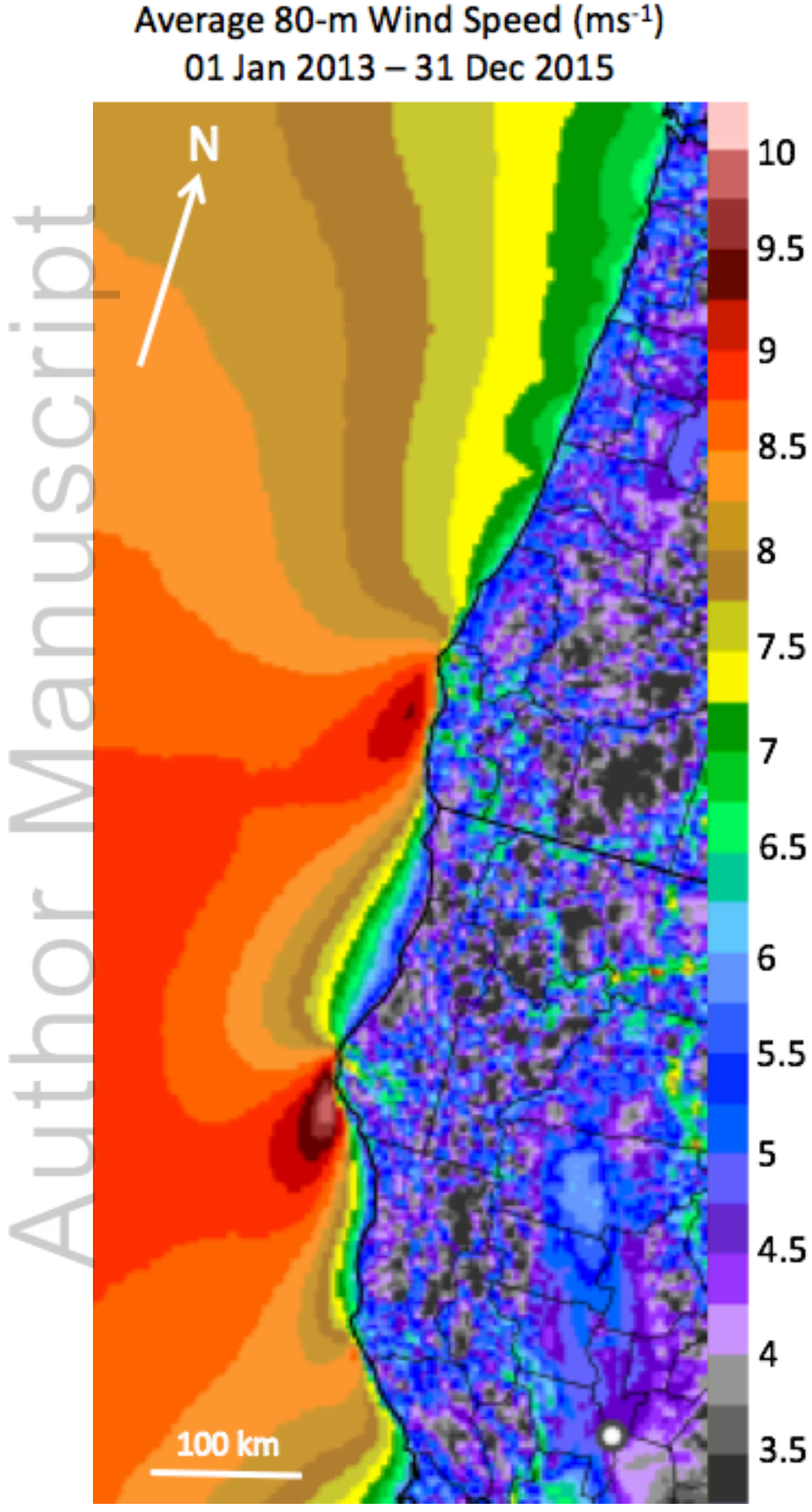

WE_2161_F18.png

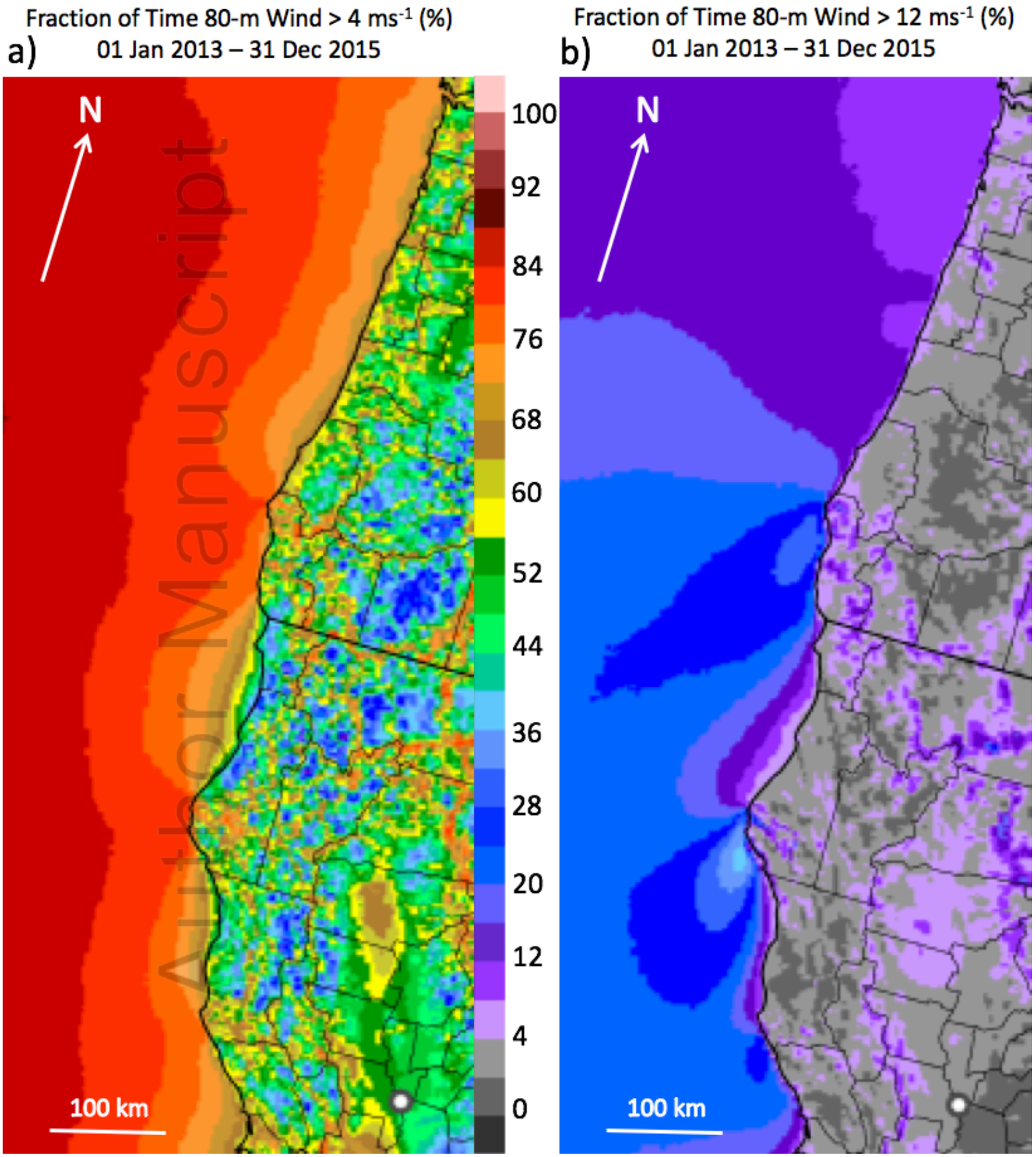

WE_2161_F19.png